To the Graduate Council:

I am submitting herewith a dissertation written by Milan Buncick entitled "Optical Absorbance of Silver Ellipsoidal Particles." I have examined the final copy of this dissertation for form and content and recommend that it be accepted in partial fulfillment of the requirements for the degree of Doctor of Philosophy, with a major in Physics.

Thomas L. Ferrell, Major Professor

We have read this dissertation and recommend its acceptance:

H. R. Daemach

K. H. Ritchie

T. A. Callcott

Donald W. Boulden

Accepted for the Council:

Vice Provost
and Dean of the Graduate School

# OPTICAL ABSORBANCE OF SILVER ELLIPSOIDAL PARTICLES

A Dissertation

Presented for the

Doctor of Philosophy

Degree

The University of Tennessee, Knoxville

Milan Buncick

June 1987

## ACKNOWLEDGEMENTS

I wish to express my gratitude to Dr. T. L. Ferrell who provided guidance throughout this work, set aside his own work to help with problems whenever necessary, and provided financial support. I would also like to thank Dr. R. J. Warmack for the benefit of his expertise and patience, and for his ability to approach a problem in a straightforward manner. Thanks to Dr. R. H. Ritchie for helpful discussions and to Maxine Martin for her help in the preparation of this document for the graduate school. A special thanks goes to Susan Roakes for her help and moral support during the final phase of this effort.

Finally, I would like to thank friends and colleagues for advice and support making this a more pleasant and productive endeavor.

# ABSTRACT

We have studied the optical absorbance of silver ellipsoidal particles with parallel principal axes. A simple technique for producing arrays of silver particles in this configuration is described. The particles were characterized by scanning electron microscopy. The optical absorbance of the silver ellipsoids produced by this technique was measured as a function of wavelength, polarization, and incident angle of the incident light. Theoretical analysis of the response of these objects was made using nonretarded electrodynamics and the bulk optical constants for silver. The dipole approximation was assumed. The results indicate that resonant surface-plasmon modes are stimulated along the principal axes of the ellipsoids and contribute to the absorbance. The calculations are shown to compare favorably with the measurements.

TABLE OF CONTENTS


| CHAPTER | | PAGE |
|---|---|---|
| I. | INTRODUCTION | 1 |
| | Submicron Physics | 1 |
| | Basic Principles | 3 |
| | Microlithography | 5 |
| | Sample Choice | 8 |
| | Organization of the Present Work | 9 |
| II. | OPTICAL PROPERTIES OF SPHEROIDS AND ELLIPSOIDS | 11 |
| | Introduction | 11 |
| | The Non-retarded Limit and the Dipole Approximation | 11 |
| | General Approach | 18 |
| | Coordinate Systems | 23 |
| | The Dielectric Response | 34 |
| | The Spheroidal and Spherical Limits | 49 |
| | Dipole Moments and the Polarizability | 54 |
| | Cross Sections | 56 |
| | The Optical Absorbance | 71 |
| III. | EXPERIMENT | 73 |
| | Introduction | 73 |
| | Sample Preparation | 73 |
| | Apparatus | 84 |
| | Data-Taking Procedure | 87 |
| IV. | EXPERIMENTAL RESULTS AND COMPARISON WITH THEORY | 89 |
| | Introduction | 89 |
| | Results and Comparisons | 89 |
| | Substrate Effects | 117 |
| | Conclusions | 120 |
| REFERENCES | | 123 |
| APPENDICES | | 129 |
| A. | OBLATE AND PROLATE SPHEROIDAL COORDINATES | 130 |
| B. | THE TOTAL CROSS SECTION | 140 |
| VITA | | 146 |

# LIST OF FIGURES


| FIGURE | | PAGE |
|---|---|---|
| 2-1. | A Set of Coordinate Surfaces for Oblate Spheroidal Coordinates | 25 |
| 2-2. | A Cross Section of the Oblate Spheroidal Coordinate System | 27 |
| 2-3. | A Set of Coordinate Surfaces for Prolate Spheroidal Coordinates | 30 |
| 2-4. | A Cross Section of the Prolate Spheroidal Coordinate System | 31 |
| 2-5. | A Set of Coordinate Surfaces for Ellipsoidal Coordinates | 35 |
| 2-6. | The Dielectric Function for the Two Dipole Modes of Surface Plasmon Oscillations on Oblate Spheroids as a Function of Shape Parameter | 39 |
| 2-7. | The Dielectric Function for the Two Dipole Modes of Surface Plasmon Oscillations on Prolate Spheroids as a Function of Shape Parameter | 41 |
| 2-8. | Dielectric Response as a Function of Axis Ratio c/a for Values of Ratio b/a for Resonant Charge-density -oscillation Modes in Silver Ellipsoids | 50 |
| 2-9. | The Angles $\Theta$ and $\Phi$ that the Incident Propagation Vector $\hat{n}_i$ Makes with Respect to the z- and x-axes | 60 |
| 2-10. | The Relationship Between the Incident Electric Vector and the Coordinate Axes for s-polarization | 62 |
| 2-11. | The Relationship Between the Incident Electric Vector and the Coordinate Axes for p-polarization | 64 |
| 2-12. | The Calculated Mode Energies for the Two Dipole Modes for Oblate Silver Spheroids as a Function of Shape Parameter | 67 |
| 2-13. | The Calculated Mode Energies for the Two Dipole Modes for Prolate Silver Spheroids as a Function of Shape Parameter | 68 |

FIGURE PAGE

2-14. Dielectric Response as a Function of Axis Ratio c/a for Values of Ratio b/a for Resonant Charge-density -oscillation Modes in Silver Ellipsoids . . . . . 69

2-15. The Ratio of Scattering Cross Section to Total Cross Section as a Function of the Wavelength for Different Shapes of Ellipsoids . . . . . 70

3-1. A General Schematic for the Production of Silver Ellipsoids . . . . . 74

3-2. A Monolayer of 272-nm-diameter Polystyrene Spheres on a Substrate. The Substrate Was Flooded With a 3.3% Solids Mixture of Spheres and Water and Spun at 1000 rpm Until Dry. A Grain Boundary and Dislocations Are Visible. The Bar Indicates a Length Of 5.18$\mu$m. . . . . 77

3-3. A Monolayer of 272-nm-diameter Polystyrene Spheres on a Substrate. The Substrate Was Flooded With a 3.3% Solids Mixture of Spheres and Water and Spun at 1000 rpm Until Dry. A Grain Boundary and Dislocations Are Visible. The Bar Indicates a Length Of 296nm . . . . . 78

3-4. A Silver-particle Array Fabricated by Depositing Silver Over a close-packed array of 272-nm-diameter spheres . . 79

3-5. $SiO_2$ Posts Fabricated by Reactive-ion Etching in $CHF_3$ . . 81

3-6. Silver Deposited on a Set of Posts at 35° With Respect to the Sample Normal . . . . . 83

3-7. A Schematic of the Components of the Spectrophotometer . . . . . 85

4-1. Experimental parameters . . . . . 90

4-2. Comparison of Experimental and Theoretical Absorbance for p-polarized Light for a Single Ellipsoid . . . . . 92

4-3. Comparison of Experimental and Theoretical Absorbance for s-polarized Light for a Single Ellipsoid . . . . . 93

4-4. Conditions Under Which Silver Bridges Form Across the Small Gap Between Close Lying Posts to Form a Single Ellipsoid . . . . . 95

FIGURE PAGE

4-5. Comparison of Measured and Calculated Absorbance for p-polarized Light for Two Ellipsoids . . . . . 96

4-6. Comparison of Measured and Calculated Absorbance for s-polarized Light for Two Ellipsoids . . . . . 98

4-7. Comparison of Experimental and Theoretical Absorbance for s-polarized Light at $\Phi$=0°,$\theta$=0° . . . . . 99

4-8. Comparison of Experimental and Theoretical Absorbance for s-polarized Light at $\Phi$=0°,$\theta$=45° . . . . . 101

4-9. Comparison of Experimental and Theoretical Absorbance for s-polarized Light at $\Phi$=0°,$\theta$=90° . . . . . 102

4-10. Comparison of Experimental and Theoretical Absorbance for p-polarized Light at $\Phi$=0°,$\theta$=0° . . . . . 103

4-11. Comparison of Experimental and Theoretical Absorbance for p-polarized Light at $\Phi$=0°,$\theta$=45° . . . . . 104

4-12. Comparison of Experimental and Theoretical Absorbance for p-polarized Light at $\Phi$=0°,$\theta$=90° . . . . . 105

4-13. A Comparison of the Measured Resonance Peaks with Those Calculated for Silver From the Allowed Values of the Dielectric Function and the Bulk Silver Optical Data . . 107

4-14. The Absorbance of a Thin Silver Film. For p-polarized Light . . . . . 109

4-15. The Absorbance of a Thin Silver Film. For s-polarized Light . . . . . 110

4-16. Measured and Calculated Absorbance for Silver Posts Produced by a Field-assisted Evaporation Technique. The Incident Light is p-polarized . . . . . 115

4-17. Measured and Calculated Absorbance for Silver Posts Produced by a Field-assisted Evaporation Technique. The Incident Light is p-polarized . . . . . 116

# CHAPTER I

# INTRODUCTION

## A. SUBMICRON PHYSICS

During the past decade a number of new subfields of condensed-matter science have emerged as new experimental techniques have developed. Among the new subfields is the area of submicron physics. This work is concerned with new types of submicron samples that were especially developed for experiments and theoretical analysis in the Liquid and Submicron Physics Group at Oak Ridge National Laboratory in collaboration with the University of Tennessee.

Submicron physics is the study of the physical properties of structures with one or more dimensions smaller than a micrometer (micron or $10^{-6}$ meter). Electromagnetic radiation is an important probe in this rapidly evolving field. The elastic and inelastic scattering of radiation by submicron structures and the interaction of atoms, molecules, and charged particles with submicron structures has received increasing attention due to both technological applications and interest in fundamental physics on the submicron size scale. Although the structures studied have dimensions less than one micrometer they are frequently of sufficient size so that they retain a variety of properties of the bulk material from which they are made. This limit can be as small as a few nanometers. A thorough understanding of the mechanisms of electromagnetic interactions with these surfaces can

contribute to advancements not only in surface physics but in medicine, chemistry, biology, and the electronics industry. Because of the rapidity with which optical measurements can be made, and because of its relative convenience, electromagnetic scattering is a vital field in the area of submicron physics. The present work is concerned with the production of new types of submicron samples that are easily probed with visible light, are highly effective in surface-enhanced Raman scattering experiments, and may be of use in a variety of other experiments.

This work presents a simple technique for producing arrays of submicrometer particles approximately ellipsoidal in shape. These particles of silver were produced in a well-defined orientation so that each sample contained an array of ellipsoids with parallel principal axes. The samples were probed by measuring the optical absorbance of the arrays as a function of the wavelength, polarization, and angle of incidence of the incident light. This work also presents a theory for describing the major features of the absorbance. The shape and size of the ellipsoids has been used as a parameter to compare the theory with the measured absorbance. The absorbance peak positions can be controlled by varying the shape. The heights of the maxima can be controlled by varying the size. Independent measurements were made using scanning electron microscopy to characterize the shape.

One intent of this work is to develop a reliable method of optically determining the shape of particles much smaller than the

wavelength of light. This is impossible using only elastic scattering but is a clear possibility using inelastic scattering data from absorbance measurements. In our samples elastic scattering is only a small part of the total absorbance. Among the factors that complicate the shape determination are the effect of the substrate interactions and the distribution of the shapes of particles for a given sample. Changes in sample preparation technique can help determine the contribution of some of these factors.

A well-known surface plasmon related phenomenon is surface-enhanced Raman scattering (SERS). While some types of structures have shown promise as substrates for SERS [1.1],[1.2], structures similar to the ones presented here are many times more effective in SERS [1.3]. However, the particles formed in reference [1.3] are not as easily characterized as those produced in this work. The optical data and sample characterization presented here may add to the understanding of SERS as well as other surface plasmon related phenomena. The ability to control the absorbance peak position provides a means for understanding the physical mechanisms of SERS, although these mechanisms remain to be unambiguously determined.

## B. BASIC PRINCIPLES

Scattering of electromagnetic waves by any system is related to the heterogeneity of that system [1.4]. This heterogeneity can be on a molecular scale or on a scale of aggregations of molecules. The

underlying physics is the same for all systems regardless of scale. Because matter contains protons and electrons it consists of discrete electronic charges. If an electromagnetic wave is incident on an object electric charges are set into oscillatory motion by the electric field of the wave. The accelerated charges radiate electromagnetic energy in all directions producing scattered radiation. In addition to emitting scattered radiation, the excited charges may convert some of the energy into some other form. This is the process of absorption. Both scattering and absorption can be modeled for samples down to a few nanometers in size using macroscopic electrodynamics.

In a metal the conduction electrons are not bound to individual ion cores and are essentially free, except for damping, to move about under the influence of an external force. They combine with the ion cores to form a condensed matter plasma. If the properties of the metal and the wavelength of the exciting energy are such that the electron interactions are predominantly collective in nature, this system will exhibit a resonance in which longitudinal waves of oscillating charge separation propagate with some damping through the plasma. This was first shown in work by Bohm and Pines in 1951 [1.5]. This longitudinal wave has, for small damping, an associated energy quantum known as the volume plasmon. It has an energy of

$$\hbar\omega_p = \hbar \left( \frac{4\pi n_0 e^2}{m^*} \right)^{\frac{1}{2}} \qquad (1\text{-}1)$$

where $\hbar$ is Planck's constant divided by $2\pi$, e is the electron charge, n is the electron density, and $m^*$ is the effective electron mass. In 1957 Ritchie [1.6] showed that there are also waves with associated quanta at the surface of a metal. For a plane semi-infinite boundary of a free-electron gas, the surface plasmon is the energy quantum and its energy is related to the volume plasmon energy by

$$\hbar\omega_{sp} = \frac{\hbar\omega_p}{\sqrt{2}} . \qquad (1\text{-}2)$$

Review articles by Ritchie [1.7], Steinmann [1.8], Raether [1.9], and Ferrell [1.10] discuss the plasmon properties and the interactions of plasmons with photons and charged particles.

The excitation of surface plasmons enable optical scattering to provide shape data for particles smaller than the wavelength of the probe. In Chapter II we show that the surface plasmon spectrum is sensitive to the particle shape. The surface plasmons appear as resonances in the polarizability of the ellipsoids, and the quantum connection is provided by the proportionality between frequency and energy as discussed above.

## C. MICROLITHOGRAPHY

Production of submicron structures generally involves some microlithographic technique. The structures produced can be a variety of shapes and sizes, can consist of different materials and can be

produced in a variety of ways. In general, microlithography has greatly benefited from such developments as long-chain polymer resists and anisotropic, dry etching. The simple techniques generally produce structures with a distribution of sizes and shapes. Minimizing the width of the distribution usually involves using a more complex fabrication process. However, particles of a single shape (spheres) can be produced by a simple process that permits metal smokes with 4-5 nm radii to be formed by vacuum evaporation in the presence of an inert gas atmosphere [1.11]. This process also gives a narrow size distribution. Larger spheres in ordered arrays can be produced by a lift-off process [1.12] in which the metal structure is deposited directly onto the substrate through a mask produced by electron beam lithography. This process is considerably more complicated.

Heat treating vacuum evaporated thin metal films [1.13]-[1.15] will form spheroids. This process is very simple but does produce a reasonably large size and shape distribution. Spheroids and ellipsoids can be formed indirectly by deposition of metals on a patterned substrate [1.16]-[1.18]. The patterned substrate consists of ordered arrays of submicron posts produced by a crossed-grating lithography technique. Production of these ordered arrays requires a series of somewhat complicated lithographic steps. One type of patterned substrate that can be made in this way [1.19] consists of quartz posts. This allows production of individual submicron particles by subsequent deposition of metal. Random arrays of quartz microneedles can be

produced by using a thin silver island film as an etch mask [1.3]. Metal deposited on these substrates also produces spheroids and ellipsoids, but with a distribution of sizes and shapes. Ordered arrays of high aspect ratio metal posts can be produced using electron beam lithography [1.20], [1.21] and by use of a deposition mask [1.22]. Lithography techniques are highly developed because of extensive use in the electronics industry. In general, the many commercial applications of small structures made by lithography have contributed to the availability of equipment and techniques for basic physical investigations.

Using microlithography techniques it is possible to produce patterned metal structures directly. The main difficulty in using a direct pattern technique is that the metal surface may become contaminated during the lithography process or by subsequent use. By producing a patterned substrate that is reusable, it is possible to deposit fresh metal just prior to making optical measurements. This not only provides uncontaminated metal particles but also does not require the lithography process to be repeated for each new measurement.

The present work offers a different method for producing patterned arrays [1.23], [1.24]. These are formed using a monolayer of polystyrene spheres as a first step in a process that ultimately produces ordered arrays of microneedles that lean with respect to the substrate normal. Silver can be deposited on the sides of the needles

so that particles are formed which are approximately ellipsoidal in shape. Shadowing during the silver deposition helps to determine the shape and size of the ellipsoids. To form ellipsoids of different shapes it is only necessary to change the angle of deposition.

This fabrication technique has several advantages over other patterned substrate methods. The random arrays of needles are easy to produce yet the stochastic arrangements and the size variation of the needles form ellipsoids with a large size and shape distribution. The sphere monolayer production process yields a final particle size and shape distribution that is considerably smaller than those produced by the island-film technique. Liao [1.19] constructed arrays of larger posts by using a more complicated, and more costly technique. His arrays had long and short range order, but his posts were oriented parallel to the substrate normal. He also deposited silver on the sides of posts to form particles in an effort to produce new SERS substrates. The technique presented here is a relatively straightforward and inexpensive technique for producing small, uniform ellipsoidal particles and provides the most highly effective SERS substrates known [1.3].

## D. SAMPLE CHOICE

We have chosen silver for study because it is easy to use experimentally and because it has a relatively sharp surface plasmon spectrum in the visible spectrum. Optical absorbance can be measured

on other materials using different wavelength ranges as necessary. With silver surface plasmon oscillations may be observed along each principal axis of the ellipsoids in the 300-800 nm wavelength range. For changes in shape the resonance peak position shifts. The peak position is determined primarily by the real part of the dielectric function of the material. Because the slope of the real part of the dielectric function for silver is rather steep in the higher-energy part of this spectral region we expect relatively small shifts in the absorbance peak position for changes in shape. At longer wavelengths the real part of the dielectric function varies more slowly with energy and much larger shifts of peak positions are observed as the particle shapes are changed. The imaginary part of the dielectric function for silver grows with increasing wavelength so the longer wavelength peaks are broadened.

## E. ORGANIZATION OF THE PRESENT WORK

In the succeeding chapters we describe an investigation of the optical absorbance of ellipsoidal particles. The general procedure of Ritchie et. al. [1.25] is used to establish a theoretical model applicable to spheroids and ellipsoids. We model our particles as ellipsoids. The calculations for ellipsoids require the numerical evaluation of several integrals. Since spheroids are a special case of ellipsoids and the calculations for spheroids can be evaluated exactly, we include analytical calculations for spheroids to allow comparison

with those for ellipsoids. Measurements of the absorbance of our samples as a function of the incident wavelength, angle, and polarization are compared with calculations to determine the validity of the model.

# CHAPTER II

# OPTICAL PROPERTIES OF SPHEROIDS AND ELLIPSOIDS

## A. INTRODUCTION

This chapter presents an analysis of light scattering and absorption by metal spheroids and ellipsoids. We assume that they are much smaller than the wavelength of the incident light and are placed in a uniform time-varying electric field. Therefore we use non-retarded electrodynamics and assume the dipole approximation. The field of the light gives rise to time-varying potentials and charge densities that are relatively straightforward to calculate. We assume that the dielectric function characterizing the metal is frequency dependent and complex, and that the bulk optical properties of the metal apply to our samples. We use the induced charge densities to calculate the dipole moments along the principal axes. The optical absorbance is determined for two polarizations using these dipole moments and the total cross section.

## B. THE NON-RETARDED LIMIT AND THE DIPOLE APPROXIMATION

Maxwell's equations consist of a set of coupled first-order differential equations which describe the behavior of electromagnetic fields. They are written in Gaussian units as [2.1]

$$\left.\begin{aligned} \nabla \cdot \vec{D} = 4\pi\rho \quad , \quad \nabla \times \vec{H} = \frac{4\pi}{c}\vec{J} + \frac{1}{c}\frac{\partial \vec{D}}{\partial t} \ , \\ \nabla \cdot \vec{B} = 0 \quad , \quad \nabla \times \vec{E} - \frac{1}{c}\frac{\partial \vec{B}}{\partial t} = 0 \ , \end{aligned}\right\} \tag{2-1}$$

where $\vec{D}$ is the electric displacement vector, $\vec{H}$ is the magnetic field, $\vec{B}$ is the magnetic flux density, $\vec{E}$ is the electric field, $\vec{J}$ is the current density, $\rho$ is the electric charge density, t is the time, and $\nabla$ is the del operator. If we use vector and scalar potentials, the Maxwell equations can be reduced to two second-order equations. Writing the magnetic field in terms of the vector potential, $\vec{A}$,

$$\vec{B} = \nabla \times \vec{A} \ . \tag{2-2}$$

From Faraday's law and the fact that the curl of the divergence of any scalar is zero

$$\vec{E} + \frac{1}{c}\frac{\partial \vec{A}}{\partial t} = - \nabla\Phi \ , \tag{2-3}$$

where $\Phi$ is the scalar electric potential. In a homogeneous, isotropic medium where the magnetic permeability is equal to unity, B=H, and $D=\epsilon E$, the Maxwell equations yield

$$\nabla^2\Phi + \frac{1}{c}\frac{\partial}{\partial t}(\nabla \cdot \vec{A}) = - \frac{4\pi\rho}{\epsilon} \tag{2-4}$$

and

$$\nabla^2\vec{A} - \frac{\epsilon}{c^2}\frac{\partial^2 \vec{A}}{\partial t^2} - \nabla(\nabla \cdot \vec{A} + \frac{\epsilon}{c}\frac{\partial \Phi}{\partial t}) = - \frac{4\pi}{c}\vec{J} \ . \tag{2-5}$$

To uncouple the equations and treat $\Phi$ and $\vec{A}$ separately we assume the Lorentz gauge [2.2] and the associated Lorentz condition for the medium

$$\nabla \cdot A + \frac{\varepsilon}{c} \frac{\partial \Phi}{\partial t} = 0 \ . \tag{2-6}$$

Thus we have the wave equations for the scalar and vector potentials

$$\nabla^2 \Phi - \frac{\varepsilon}{c^2} \frac{\partial^2 \Phi}{\partial t^2} = - \frac{4\pi\rho}{\varepsilon} \tag{2-7}$$

$$\nabla^2 \vec{A} - \frac{\varepsilon}{c^2} \frac{\partial^2 \vec{A}}{\partial t^2} = - \frac{4\pi \vec{J}}{c} \tag{2-8}$$

respectively, with $\rho$ the volume charge density and $\vec{J}$ the current density.

If we assume a localized source of charges and currents oscillating with a harmonic time dependence at angular frequency $\omega$ then we may write

$$\rho(\vec{r},t) = \rho(\vec{r}) e^{-i\omega t} \tag{2-9}$$

$$\vec{J}(\vec{r},t) = \vec{J}(\vec{r}) e^{-i\omega t} \ . \tag{2-10}$$

The two wave equations reduce to the inhomogeneous Helmholtz equations

$$\nabla^2 \Phi + \varepsilon k^2 \Phi = - \frac{4\pi\rho}{\varepsilon} \tag{2-11}$$

and

$$\nabla^2 \vec{A} + \varepsilon k^2 \vec{A} = - \frac{4\pi \vec{J}}{c} \ , \tag{2-12}$$

where $k=\omega/c$ is the magnitude of the wave vector. The general solution to the wave equations above are, [2.3]

$$\Phi(\vec{r}) = \int \rho(\vec{r}') \frac{e^{ik\sqrt{\varepsilon}\,|\vec{r}-\vec{r}'|}}{|\vec{r}-\vec{r}'|} d^3r' \tag{2-13}$$

and

$$\vec{A}(\vec{r}) = \int \vec{J}(\vec{r}') \frac{e^{ik\sqrt{\varepsilon}\,|\vec{r}-\vec{r}'|}}{|\vec{r}-\vec{r}'|} d^3r' \ , \tag{2-14}$$

where as usual $\vec{r}'$ locates a source point and $\vec{r}$ locates a field point. The harmonic time dependence is understood. If we assume an idealized charge density so that the charge density and current density are restricted to a vacuum boundary of the medium then the dielectric function is unity. In general we shall write any field variable $f(\vec{r},t)$ as

$$f(\vec{r},t) = f(\vec{r})e^{-i\omega t} \ . \tag{2-15}$$

If the argument is left understood the function is assumed to be a function of $\vec{r}$ only.

The electric field now becomes

$$\vec{E} = -\nabla\Phi + \frac{i\omega}{c}\vec{A} \tag{2-16}$$

and the magnetic field remains as given by Eq. (2-2). The continuity equation

$$\nabla \cdot \vec{J}(\vec{r},t) + \frac{\partial\rho(\vec{r},t)}{\partial t} = 0 \tag{2-17}$$

is

$$\nabla \cdot \vec{J} - i\omega\rho = 0 \ . \qquad (2\text{-}18)$$

If the source dimensions are of order d, then $r' < d$ and if $d\omega/c$ is small, then near the boundary $k|\vec{r}-\vec{r}'|$ is small. In this case we may set the exponential terms in the vector and scalar potential expressions equal to unity. Then each Fourier frequency component of the potentials satisfies the same equations as in electrostatics. The magnetic effects are then negligible and the electrodynamics may be treated with equations that, except for having harmonic amplitudes, have solutions that are the same as those found in electrostatics. The limit under which these conditions apply is known as the "non-retarded" limit.

For optical experiments, if the particulate dimensions are small compared to the wavelength of the incident light the spatial variation of the electromagnetic wave can be neglected over the dimensions of the particle. For incident plane waves, the general expression, $\vec{E}=\vec{E}_o e^{i\vec{k}\cdot\vec{r}-i\omega t}$ , can be approximated by $\vec{E}=\vec{E}_o e^{-i\omega t}$. This is the dipole approximation [2.4]. Thus, for example, the field inside the particle is uniform, while outside the field is the superposition of a dipole field and the applied uniform field. So in a multipole expansion with multipole summation index $\ell$, the only contribution comes from the $\ell=1$ term.

Retardation Correction Terms

In general Maxwell's equations involve $\epsilon(k,\omega)$, a wave-vector and frequency dependent dielectric function. For optical applications to metals, and as long as the source is large enough so that bulk optical properties are valid, spatial dispersion has little importance, and only the frequency dependence need be considered. Typically bulk properties apply for sources with dimensions of the order of or greater than one nanometer.

The importance of retardation for a given material increases with size. For silver the effect of retardation is small until the source dimensions exceed 55nm [2.5]. These effects are well quantified for spheres by the Mie theory [2.6]. For the dipole mode of a sphere the boundary conditions give $\epsilon(\omega)=-2$ in the nonretarded case, while for low-order retardation effects

$$\epsilon(\omega) = -2 - \frac{12}{5}\frac{\omega^2 a^2}{c^2} \qquad (2\text{-}19)$$

where a is the radius of the sphere. The Mie theory gives a transcendental eigenvalue equation for which Eq.(2-19) is obtained as an approximation. The retardation correction neglecting terms of order higher than $(a\omega/c^2)$ may be obtained by using Eq.'s (2-13) and (2-14) for $\Phi$ and $\vec{A}$ and using the binomial expansion of the exponential term for small arguments. Thus, for zero net charge, we have the following form with the lowest order correction included;

$$\Phi = \int \frac{\rho(\vec{r}')}{|\vec{r} - \vec{r}'|} - \frac{k^2}{2} \int \rho(\vec{r}') |\vec{r} - \vec{r}'| d^3r' \tag{2-20}$$

or

$$\Phi = \Phi^0 - \frac{k^2}{2} \int \rho(\vec{r}') |\vec{r} - \vec{r}'| d^3r' \ . \tag{2-21}$$

The potential $\Phi^o$ satisfies Laplace's equation inside and outside the source. The idealized charge density is zero everywhere except at the boundary and is obtained from Poisson's equation for $\Phi^o$.

The electric field is obtained from (2-21) and (2-16)

$$\vec{E} = \vec{E}^0 + \frac{k^2}{2} \int \frac{\rho(\vec{r}')(\vec{r} - \vec{r}')}{|\vec{r} - \vec{r}'|} d^3\vec{r}' + \frac{i\omega}{c} \vec{A} \ , \tag{2-22}$$

where $\vec{E}^o$ is $-\nabla\Phi^o$. We then write

$$\vec{E} = \vec{E}^0 + \frac{k^2}{2} \vec{r}\Phi^0 - \frac{k^2}{2} \int \rho(\vec{r}')\vec{r}' d^3r' + \frac{i\omega}{c} \vec{A} \ . \tag{2-23}$$

The boundary conditions are

$$\Phi_{in}\Big|_s = \Phi_{out}\Big|_s \ , \tag{2-24}$$

where S is the surface of the metal and

$$\epsilon(\omega)\vec{E}_{in} \cdot \hat{e}_n\Big|_s = \vec{E}_{out} \cdot \hat{e}_n\Big|_s \ , \tag{2-25}$$

where $\epsilon(\omega)$ is the dielectric function of the medium bounded by the surface S at angular frequency $\omega$ and $\hat{e}_n$ is the unit vector normal to the surface. Eq .(2-24) is equivalent to the continuity of the tangential component of the electric field while (2-25) is equivalent

to the continuity of the normal component of the electric displacement vector. All field quantities are assumed to be Fourier frequency components in general, although we have simply used a harmonic time dependence. Application of the boundary conditions produces an eigenequation for $\epsilon(\omega)$ that specifies the surface resonance conditions.

This procedure works well for a sphere, but not for spheroids. For a spheroid the retardation correction gives an eigenequation for $\epsilon(\omega)$ that requires diagonalizing a complicated matrix. Nevertheless, the above treatment illustrates the idea of retardation corrections in a simple way.

## C. GENERAL APPROACH

For the calculations applied to spheroids or ellipsoids we choose a coordinate system in which a constant value of one coordinate represents the surface of the particulate. We assume the source is bounded and has no net charge. The charge and current densities arise from charge displacements from equilibrium. We assume an idealized surface charge density at the particulate boundary and a spatially local, frequency dependent dielectric function $\epsilon(\omega)$, for the source. For the non-retarded limit the potentials due to the surface charge density oscillations inside and outside the particulate satisfy Laplace's equation,

$$\nabla^2 \Phi_{in} = 0 \qquad (2\text{-}26)$$

$$\nabla^2 \Phi_{out} = 0 \ . \tag{2-27}$$

Free oscillations ensue and the characteristic frequency is obtained from the electromagnetic boundary conditions

$$\Phi_{in}\Big|_{surface} = \Phi_{out}\Big|_{surface} \tag{2-28}$$

$$\epsilon(\omega)\hat{e}_n \cdot \nabla\Phi_{in}\Big|_{surface} = \hat{e}_n \cdot \nabla\Phi_{out}\Big|_{surface} \tag{2-29}$$

at the surface of the particulate where $\hat{e}_n$ is the unit vector normal to the surface. The boundary conditions yield an eigenequation and a value of $\epsilon$ that is purely dependent on geometry. To obtain the corresponding eigenfrequency we match $\epsilon$ and the real part of the complex dielectric function $\epsilon(\omega)$, for the metal from which the particulate is made. For metals, the real part of the dielectric function varies from negative infinity at zero frequency up to zero at some frequency, usually in the ultraviolet. The dielectric function thereafter becomes positive, but may pass through zero several times as frequency increases. The dielectric function eventually remains positive at sufficiently high frequencies. The total cross section is a maximum at the resonant frequency. This is true for both the retarded and the nonretarded calculations.

In elementary electrostatics the expression for the dipole moment in a dielectric sphere of radius a in a uniform electric field is equal to the electric field multiplied by the polarizability

$$\alpha = a^3\left(\frac{\varepsilon - 1}{\varepsilon + 2}\right) . \tag{2-30}$$

This expression is obtained from the usual boundary conditions neglecting retardation. For a harmonic field the dielectric function depends on the angular frequency and we write

$$\varepsilon(\omega) = \varepsilon_1(\omega) + i\varepsilon_2(\omega) , \tag{2-31}$$

where $\epsilon_1(\omega)$ is the real part and $\epsilon_2(\omega)$ is the imaginary part of the dielectric function. As will be shown later in this chapter, the cross section for scattering and absorption of light is a function of the imaginary part of the polarizability. Thus we encounter the form

$$\text{Im } \alpha = \frac{3a^3\varepsilon_2}{(\varepsilon_1 + 2)^2 + \varepsilon_2{}^2} \tag{2-32}$$

that has a resonance at $\epsilon_1$=-2, and the imaginary part of the polarizability is $3a^3/\epsilon_2$ at the frequency where $\epsilon_1$=-2. At half height of the resonance the value of $\epsilon_1$ and its value at resonance are different by an amount which depends on the imaginary part of the dielectric function. At the half height point where the real part of the dielectric function is more negative than the resonance value,

$$\varepsilon_1 = - 2 \pm \varepsilon_2 . \tag{2-33}$$

Near resonance we can approximate the real part of the dielectric function with a Taylor's series expansion about the surface plasmon frequency

$$\epsilon_1 = -2 + \frac{d\epsilon_1}{d\omega}\Big|_{\omega=\omega_{sp}} (\omega - \omega_{sp}) \ . \tag{2-34}$$

If $\epsilon_2$ is small enough so that this linear approximation holds out to the half height frequency then

$$\omega = \omega_{sp} \pm \frac{\epsilon_2}{\epsilon_1'(\omega_{sp})} \ . \tag{2-35}$$

For small values of the imaginary part of the dielectric function Eq. (2-32) differs from the resonance value by $\epsilon_2^2/2$, so that the width of the resonance is small. Similar arguments may be made for spheroids.

Thus if the imaginary part of the dielectric function is small at a characteristic frequency, a well-defined resonance state may be observed in the absorbance spectrum. The quantum of this resonance oscillation is the well-known surface plasmon [2.7]. The frequency dependence of $\epsilon(\omega)$ is obtained from bulk optical data. For a nonmagnetic medium of complex index of refraction n+ik, we have

$$\epsilon = (n + ik)^2 \tag{2-36}$$

and so

$$\varepsilon_1 = n^2 - k^2 \tag{2-37}$$

and

$$\varepsilon_2 = 2nk \ . \tag{2-38}$$

k is the absorption constant of the bulk material and n is the real part of the index of refraction. Therefore the bulk optical properties give the dielectric function. Because the dielectric function is a function of frequency and mode, the boundary conditions give a dispersion relation for the geometry to which they are applied. If the dielectric function is a known function of frequency, the dispersion relation yields the resonant frequency as a function of the mode indices. For bound geometries the mode indices are discrete while for infinite surfaces the mode indices are continuous.

From the boundary conditions the potentials are determined and can be used to calculate the surface charge density, the volume charge density, and the induced dipole moment components for spheroids. For ellipsoids we determine the fields from the potentials and use the charge displacement vector to determine the dipole moment components. The radiation zone fields are written in terms of the dipole moments and used with the time-averaged Poynting vector to calculate the

absorption and scattering cross-sections. The total cross sections are used to calculate the optical absorbance.

## D. COORDINATE SYSTEMS

We have used three coordinate systems to calculate the electrodynamic properties of ellipsoidal and spheroidal particles. The most general of these coordinate systems is the ellipsoidal coordinate system in which there are three principal axes. Each has a unique length. Oblate and prolate spheroidal coordinates are special cases of ellipsoidal coordinates. These coordinate systems have two principal axes that are the same length and thus are specified completely by a semimajor and a semiminor axis. The spheroidal coordinates are obtained by a rotation of a system of confocal ellipses about an axis of symmetry. The oblate and prolate coordinates are distinguished according to whether the rotation takes place about the major or the minor axes of the ellipses.

### Oblate Spheroidal Coordinates

The oblate spheroidal coordinate system consists of families of mutually orthogonal confocal spheroids, single-sheeted hyperboloids and half planes [2.8]. The axis of revolution (the Cartesian z-axis) is collinear with the minor axes of the ellipses. The origin is at the ellipse centers and the coordinates are denoted $(\eta,\theta,\phi)$. A constant value of $\eta$ specifies the surface of a spheroid. The coordinate $\theta$

specifies a hyperboloid where $\theta$ is the angle between the axis of revolution and the asymptote of the hyperboloid. The azimuthal angle is $\phi$ and is measured relative to the x-axis of Cartesian coordinates about the z-axis as in spherical coordinates. Thus $\eta$ is a "radial coordinate" and $\theta$ is a "polar coordinate". The coordinate ranges are

$$\left.\begin{aligned} 0 < \eta < \infty \\ 0 < \theta < \pi \\ 0 < \phi < 2\pi \ . \end{aligned}\right\} \tag{2-39}$$

The family of oblate spheroids is generated by

$$\frac{x^2 + y^2}{1 + \eta^2} + \frac{z^2}{\eta^2} = a^2 \tag{2-40}$$

here a is the focal length. The family of single-sheeted hyperboloids is generated by

$$\frac{x^2 + y^2}{\sin^2\theta} - \frac{z^2}{\cos^2\theta} = a^2 \tag{2-41}$$

where a is the focal length. The transformation equations for Cartesian coordinates for any spatial point are

$$x = a(1 + \eta^2)^{\frac{1}{2}} \sin\theta \cos\phi \tag{2-42}$$

$$y = a(1 + \eta^2)^{\frac{1}{2}} \sin\theta \sin\phi \tag{2-43}$$

$$z = a\,\eta \cos\theta \ . \tag{2-44}$$

Figure 2-1 shows a set of coordinate surfaces $(\eta,\theta,\phi)$ [2.9]. It also shows the focal length a, the asymptote of the hyperbola and the angle

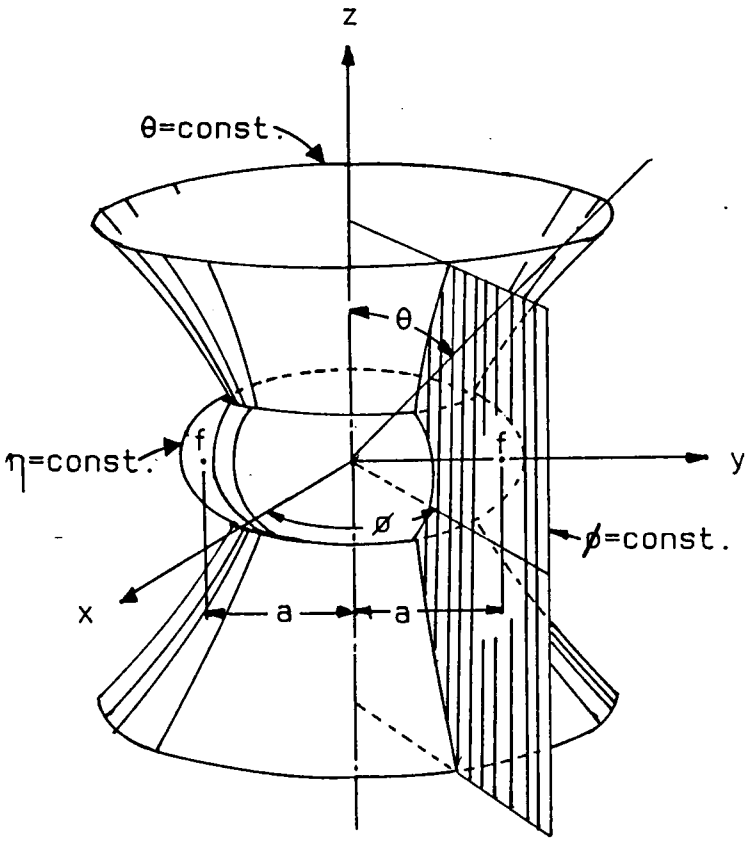



Figure 2-1. A set of coordinate surfaces for oblate spheroidal coordinates. The focal length, a, is shown along with the angle to the asymptote, θ, and the azimuthal angle $\phi$.

$\theta$. Figure 2-2 shows a cross section of the curves generated by a range of coordinates. The axis of rotation is the vertical axis. The surface of a spheroid and thus its shape is determined by

$$\eta = \eta_0 = \text{constant}$$

and the coordinate $\eta_0$ of a spheroid is related to the minor to major axis ratio R. If we call the semimajor axis length A then from Eq.'s (2-42) and (2-43) with $\theta=\pi/2$

$$x^2 + y^2 = a^2(1 + \eta_0^2) \Big|_{\theta=\pi/2} = A^2 \tag{2-45}$$

and from Eq. (2-44) with $\theta=0$, the semiminor axis is

$$B = a\eta_0 \Big|_{\theta=0} . \tag{2-46}$$

Combining these two equations we get

$$R = \frac{B}{A} = \frac{\eta_0}{(1 + \eta_0^2)^{\frac{1}{2}}} . \tag{2-47}$$

Thus for large values of $\eta_0$ the axis ratio approaches one and we get a sphere. For small values of $\eta_0$ the axis ratio is small and the particle is disk-shaped. We will refer to $\eta_0$ as the shape parameter for oblate spheroids.

Prolate Spheroidal Coordinates

The prolate spheroidal coordinates consist of families of confocal spheroids, hyperboloids of two sheets and half planes [2.10]. The axis

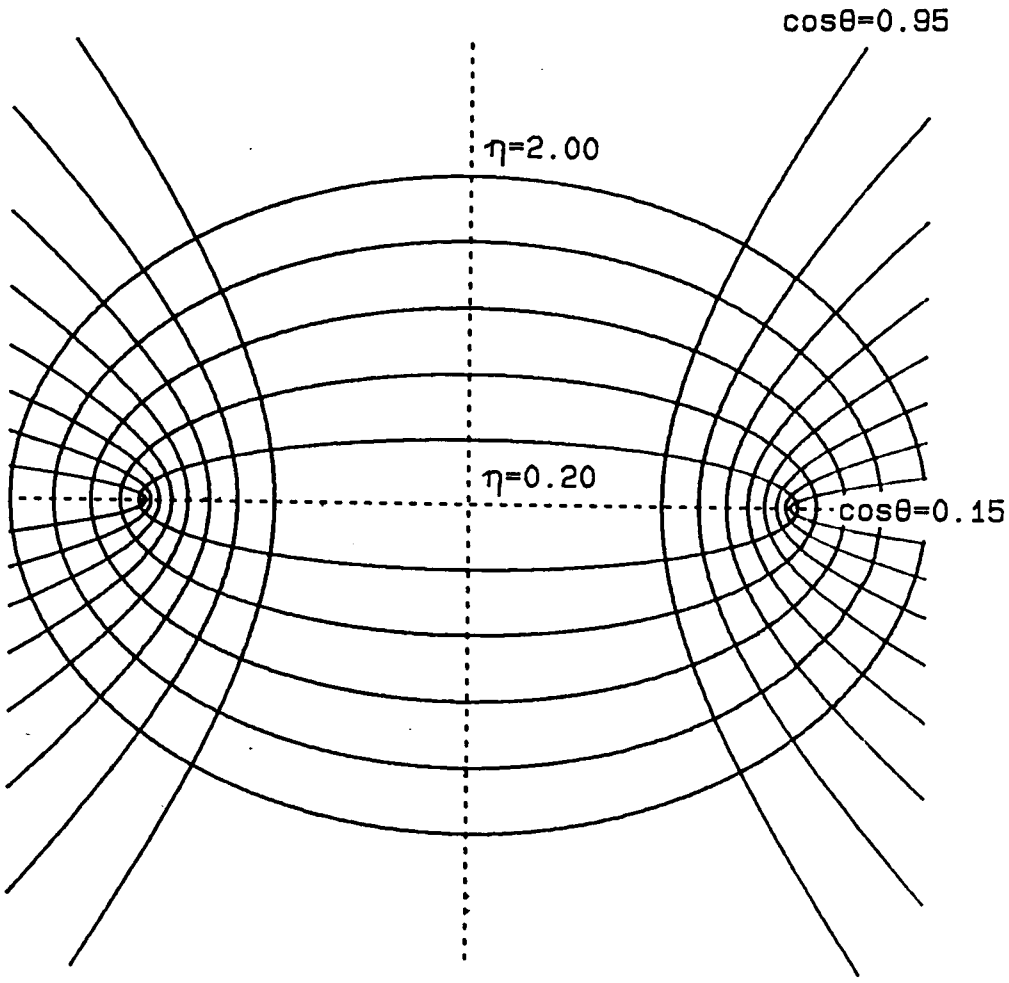



Figure 2-2. A cross section of the oblate spheroidal coordinate system. The full set of coordinates is obtained by rotation about the vertical axis.

of revolution (the Cartesian z-axis) is collinear with the major axes of the ellipses. The coordinates are denoted $(\eta', \theta, \phi)$. A constant value of $\eta'$ specifies the surface of a spheroid. The coordinate $\theta$ specifies a hyperboloid where $\theta$ is the angle between the asymptote of the hyperboloid and the axis of revolution. The angle $\phi$ is the azimuthal angle defined as in spherical coordinates. So again $\eta'$ is a "radial" coordinate and $\theta$ is a "polar" coordinate. The ranges for the coordinates are

$$\left.\begin{aligned} 1 < \eta' < \infty \\ 0 < \theta < \pi \\ 0 < \phi < 2\pi \ . \end{aligned}\right\} \qquad (2\text{-}48)$$

The family of prolate spheroids is generated by

$$\frac{x^2 + y^2}{(\eta'^2 - 1)} + \frac{z^2}{\eta'^2} = a^2 \qquad (2\text{-}49)$$

where a is the focal length. The family of hyperboloids of two sheets is generated by

$$\frac{z^2}{\cos^2\theta} - \frac{x^2 + y^2}{\sin^2\theta} = a^2 \qquad (2\text{-}50)$$

where a is the focal length. The transformation equations for Cartesian coordinates for any spatial point are

$$x = a(\eta'^2 - 1)^{\frac{1}{2}} \sin\theta \cos\phi \qquad (2\text{-}51)$$

$$y = a(\eta'^2 - 1)^{\frac{1}{2}} \sin\theta \cos\phi \qquad (2\text{-}52)$$

$$z = a\eta'\cos\theta \ . \tag{2-53}$$

Figure 2-3 shows a set of coordinate surfaces $(\eta',\theta,\phi)$ [2.11]. It also shows the focal length a, the asymptote of the hyperbola and the angle $\theta$ . Figure 2-4 shows the curves generated by several sets of coordinates. The axis of rotation is the vertical axis.

As in oblate coordinates the surface of a spheroid is determined by

$$\eta' = \eta_0' = \text{constant}$$

and the coordinate $\eta_0'$ is related to the minor to major axis ratio R. Again calling the semimajor axis A and the semiminor axis B and using the transformation Eq.'s (2-51),(2-52) and (2-53)

$$A = a\eta_0' \Big|_{\theta=0} \tag{2-54}$$

$$B^2 = x^2 + y^2 = a^2(\eta_0'^2 - 1) \Big|_{\theta=\pi/2} \tag{2-55}$$

$$R = \frac{B}{A} = \frac{(\eta'^2_0 - 1)^{\frac{1}{2}}}{\eta_0'} \ . \tag{2-56}$$

Now we see that for large values of $\eta_0'$ the axis ratio approaches one and we get a sphere. For small values of $\eta_0'$ the axis ratio is small and the particle becomes needle shaped. We also refer to $\eta_0'$ as the shape parameter for prolate spheroids.

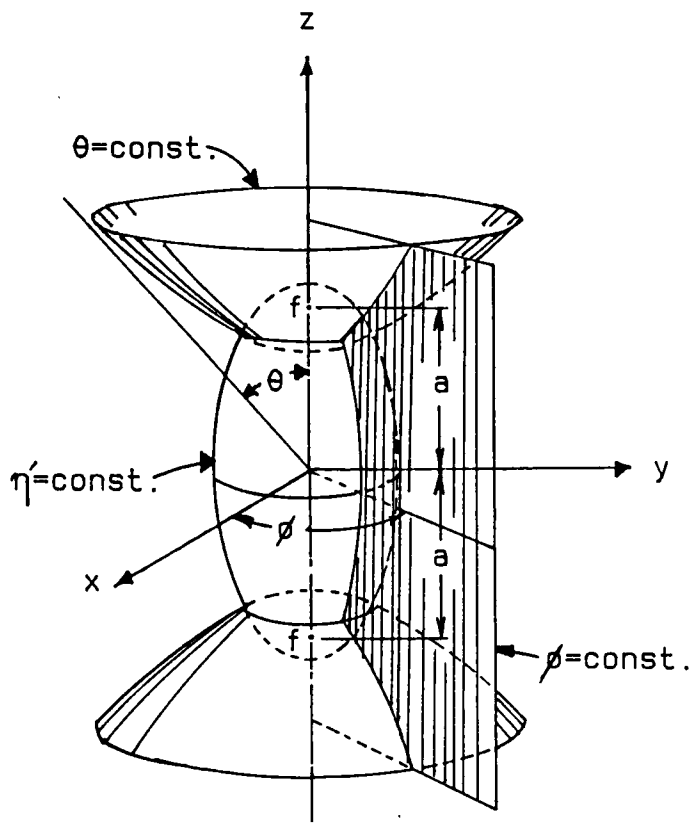



Figure 2-3. A set of coordinate surfaces for prolate spheroidal coordinates. The focal length, a, is shown along with the angle to the asymptote, $\theta$ , and the azimuthal angle $\phi$.

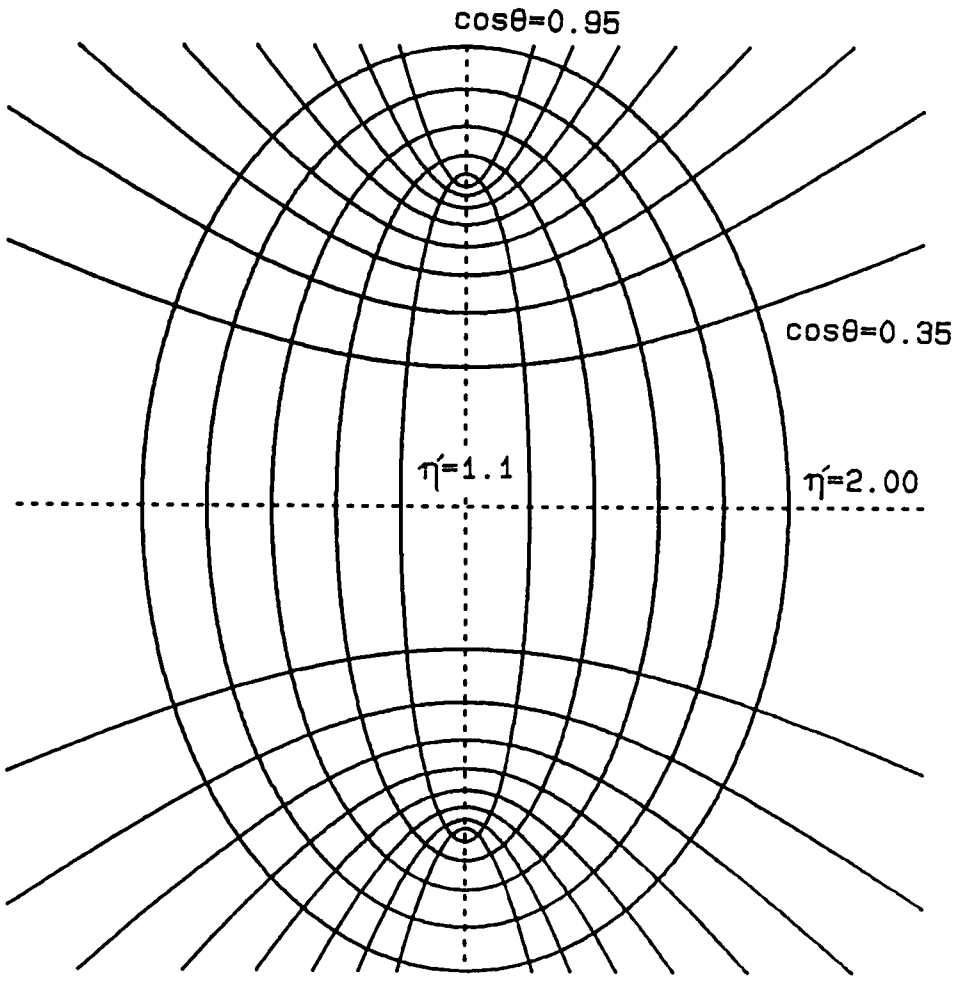



Figure 2-4. A cross section of the prolate spheroidal coordinate system. The full set of coordinates is obtained by rotation about the vertical axis.

Ellipsoidal Coordinates

The ellipsoidal coordinates consist of families of confocal ellipsoids, hyperboloids of one sheet and hyperboloids of two sheets [2.12]. In this coordinate system there is no axis of revolution. There are three semiprincipal axes and each axis has a unique length. The semiprincipal axes are (a,b,c) and we assume (a>b>c). The ellipsoidal coordinates are $(\eta,\xi,\zeta)$. To each point in space there corresponds a unique set of these coordinates. The surface $\eta$=constant specifies the surface of an ellipsoid. The coordinate $\xi$=constant is a hyperboloid of one sheet and $\zeta$=constant is a hyperboloid of two sheets. The ranges of the coordinates are

$$\begin{aligned} -c^2 &< \eta < \infty \\ -b^2 &< \xi < -c^2 \\ -a^2 &< \zeta < -b^2 \ . \end{aligned} \tag{2-57}$$

The family of confocal ellipsoids is generated by

$$\frac{x^2}{a^2+\eta} + \frac{y^2}{b^2+\eta} + \frac{z^2}{c^2+\eta} = 1 \ . \tag{2-58}$$

The families of hyperboloids of one sheet and hyperboloids of two sheets are respectively generated by

$$\frac{x^2}{a^2+\xi} + \frac{y^2}{b^2+\xi} + \frac{z^2}{c^2+\xi} = 1 \tag{2-59}$$

$$\frac{x^2}{a^2+\zeta} + \frac{y^2}{b^2+\zeta} + \frac{z^2}{c^2+\zeta} = 1 \ . \tag{2-60}$$

In each case a,b, and c are held constant. The transformation equations for Cartesian coordinates for any spatial point are

$$x = \pm\left[\frac{(\eta + a^2)(\xi + a^2)(\zeta + a^2)}{(b^2 - a^2)(c^2 - a^2)}\right]^{\frac{1}{2}} \tag{2-61}$$

$$y = \pm\left[\frac{(\eta + b^2)(\xi + b^2)(\zeta + b^2)}{(c^2 - b^2)(a^2 - b^2)}\right]^{\frac{1}{2}} \tag{2-62}$$

$$z = \pm\left[\frac{(\eta + c^2)(\xi + c^2)(\zeta + c^2)}{(a^2 - c^2)(b^2 - c^2)}\right]^{\frac{1}{2}} \tag{2-63}$$

The scale factors or metrical coefficients are

$$h_1 = \frac{1}{2}\left[\frac{(\eta - \xi)(\eta - \zeta)}{(\eta + a^2)(\eta + b^2)(\eta + c^2)}\right]^{\frac{1}{2}} \tag{2-64}$$

$$h_2 = \frac{1}{2}\left[\frac{(\xi - \eta)(\xi - \zeta)}{(\xi + a^2)(\xi + b^2)(\xi + c^2)}\right]^{\frac{1}{2}} \tag{2-65}$$

$$h_3 = \frac{1}{2}\left[\frac{(\zeta - \eta)(\zeta - \xi)}{(\zeta + a^2)(\zeta + b^2)(\zeta + c^2)}\right]^{\frac{1}{2}} \tag{2-66}$$

If we use the abbreviation

$$R_s = [(s + a^2)(s + b^2)(s + c^2)]^{\frac{1}{2}} \quad (s=\eta,\xi,\zeta) \tag{2-67}$$

then the Laplacian of a scalar $\Phi$ is

$$\nabla^2\Phi = \frac{4}{(\eta + \xi)(\eta - \zeta)(\xi - \zeta)}\left[(\xi - \zeta)R_\eta \frac{\partial}{\partial\eta}\left(R_\eta \frac{\partial\Phi}{\partial\eta}\right)\right.$$

$$\left. + (\zeta - \eta)\, R_\xi \frac{\partial}{\partial\xi}\left(R_\xi \frac{\partial\Phi}{\partial\xi}\right) + (\eta - \xi)\, R_\zeta \frac{\partial\Phi}{\partial\zeta}\left(R_\zeta \frac{\partial\Phi}{\partial\zeta}\right)\right] . \tag{2-68}$$

As the values of $\eta$ approach infinity the ellipsoid becomes a sphere of infinite radius. As $\eta$ approaches $-c^2$ the ellipsoid is flattened into an elliptical disk lying in the xy-plane. So we also use $\eta$ here as the shape parameter for ellipsoids. Any cross section of ellipsoids appears the same as the figures for oblate and prolate spheroids. Figure 2-5 shows the ellipsoidal coordinate surfaces for ellipsoids ($\eta$=const.) and hyperboloids ($\xi$=const.) and ($\zeta$=const.) [2.13].

## E. THE DIELECTRIC RESPONSE

Using the oblate and prolate coordinate systems we can use Laplace's equation and the boundary conditions (2-28) and (2-29) to obtain the allowed values for the dielectric response function $\epsilon(\omega)$ at resonance. When used with the experimentally determined values of the dielectric function for a material which forms a spheroid or ellipsoid a dispersion relation for real spheroidal or ellipsoidal particles is obtained.

### Oblate Spheroidal Coordinates

For an oblate spheroid the solution to Laplace's equation inside and outside the spheroid are given in Appendix A. They are respectively

$$\Phi_{in} = \sum_{\ell mp} A_{\ell mp}\, Q_{\ell m}(i\eta_0) P_{\ell m}(i\eta)\, Y^{p}_{\ell m}(\theta\phi) \qquad (2\text{-}69)$$

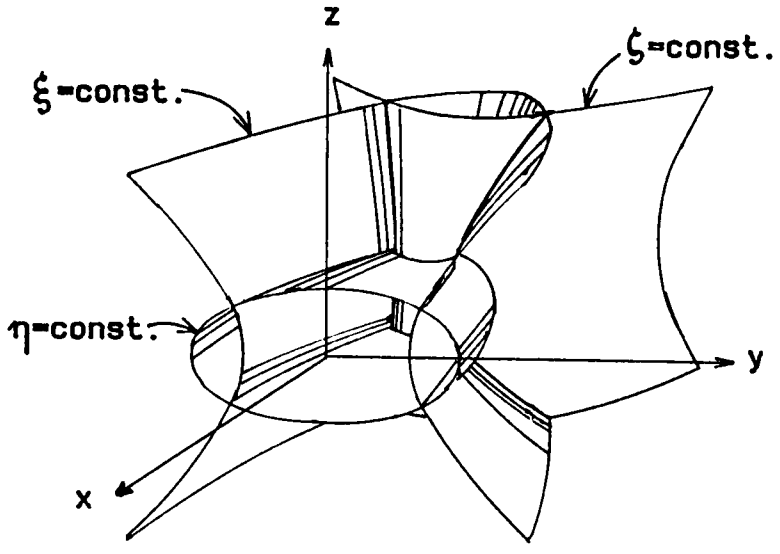



Figure 2-5. A set of coordinate surfaces for ellipsoidal coordinates. The surfaces are ellipsoids, hyperboloids of one sheet and hyperboloids of two sheets.

and

$$\Phi_{out} = \sum_{\ell mp} B_{\ell mp}\, Q_{\ell m}(i\eta)\, P_{\ell m}(i\eta_0)\, Y^p_{\ell m}(\theta\phi) \ . \qquad (2\text{-}70)$$

The $P_{\ell m}$ and $Q_{\ell m}$ are associated Legendre functions with imaginary argument and the $Y^p_{\ell m}(\theta,\phi)$ are the real spherical harmonics defined in Appendix A. We sum over the integers $\ell$=1,2,3...; m=0,1,2...l; p=$\pm$1. The $\ell$=1 terms of the Legendre functions of imaginary argument are [2.14]

$$P_{10} = i\eta \qquad (2\text{-}71)$$

$$P_{11} = i(1 + \eta^2)^{\frac{1}{2}} \qquad (2\text{-}72)$$

$$Q_{10} = \eta \cot^{-1}\eta - 1 \qquad (2\text{-}73)$$

$$Q_{11} = (1 + \eta^2)^{\frac{1}{2}}\left(\cot^{-1}\eta - \frac{\eta}{1 + \eta^2}\right) \ . \qquad (2\text{-}74)$$

The $\ell$=1 spherical harmonics are[2.15]

$$Y^{-1}_{10}(\theta,\phi) = \sqrt{\frac{3}{4\pi}}\cos\theta \qquad (2\text{-}75)$$

$$Y^{1}_{11}(\theta,\phi) = \sqrt{\frac{3}{4\pi}}\sin\theta\cos\phi \qquad (2\text{-}76)$$

$$Y^{-1}_{11}(\theta,\phi) = \sqrt{\frac{3}{4\pi}}\sin\theta\sin\phi \ . \qquad (2\text{-}77)$$

The $A_{\ell mp}$ and $B_{\ell mp}$ are functions of time. We Fourier analyze them to remove the time dependence and handle the Fourier components separately. The Fourier transform is

$$\tilde{f}(\omega) = \int_{-\infty}^{\infty} f(t) e^{i\omega t} dt \tag{2-78}$$

and the inverse transform is

$$f(t) = \frac{1}{2\pi} \int_{-\infty}^{\infty} \tilde{f}(\omega) e^{-i\omega t} d\omega \ . \tag{2-79}$$

So we have

$$\tilde{\Phi}_{in} = \sum_{\ell mp} \tilde{A}_{\ell mp} \, Q_{\ell m}(i\eta_0) \, P_{\ell m}(i\eta) \, Y^p_{\ell m}(\theta\phi) \tag{2-80}$$

$$\tilde{\Phi}_{out} = \sum_{\ell mp} \tilde{B}_{\ell mp} \, Q_{\ell m}(i\eta) \, P_{\ell m}(i\eta_0) \, Y^p_{\ell m}(\theta\phi) \ . \tag{2-81}$$

The orthogonality condition for the real spherical harmonics is

$$\int_0^{\pi} \sin\theta \, d\theta \int_0^{2\pi} d\phi \, Y^p_{\ell m}(\theta\phi) \, Y^{p'}_{\ell' m'}(\theta\phi) = \delta_{\ell}^{\ell'} \, \delta_{m}^{m'} \, \delta_{p}^{p'} \tag{2-82}$$

where $\delta_m^n$ is the Kronecker delta. Applying this orthogonality condition to boundary condition (2-28) we get

$$\tilde{A}_{\ell mp} = \tilde{B}_{\ell mp} \tag{2-83}$$

From Appendix A

$$\hat{e}_\eta \cdot \nabla \equiv \frac{1}{h_\eta} \frac{\partial}{\partial \eta} = \frac{i}{h_\eta} \frac{\partial}{\partial (i\eta)} \tag{2-84}$$

where $h_\eta$ is a scale factor given in Appendix A. Thus boundary condition (2-29) gives

$$\varepsilon(\omega) \sum_{\ell mp} \tilde{A}_{\ell mp} Q_{\ell m}(i\eta_0) P'_{\ell m}(i\eta)\Big|_{\eta=\eta_0} Y^p_{\ell m} = \sum_{\ell mp} \tilde{B}_{\ell mp} Q'_{\ell m}(i\eta)\Big|_{\eta=\eta_0} P_{\ell m}(i\eta_0)\, Y^p_{\ell m} \tag{2-85}$$

where we have used $L'_{\ell m}(i\eta)\Big|_{\eta=\eta_0} = \frac{\partial}{\partial(i\eta)}(L_{\ell m})$ for any quantity $L_{\ell m}(i\eta)$. Orthogonality of the real spherical harmonics yields the dispersion relation for oblate spheroids.

$$\varepsilon(\omega) = \varepsilon_{\ell m} = \left.\frac{P_{\ell m}(i\eta_0)\, Q'_{\ell m}(i\eta)}{Q_{\ell m}(i\eta_0)\, P_{\ell m}(i\eta)}\right|_{\eta=\eta_0} \tag{2-86}$$

Figure 2-6 shows the dielectric response function as a function of the shape parameter for the oblate spheroidal geometry. The $\ell$=1 terms of the dielectric response function are

$$\varepsilon_{10} = 1 + \frac{1}{(1 + \eta_0^2)(\eta_0 \cot^{-1}\eta_0 - 1)} \tag{2-87}$$

$$\varepsilon_{11} = 1 - \frac{2}{(1 + \eta_0^2)(\eta_0 \cot^{-1}\eta_0 - \eta_0^2)} . \tag{2-88}$$

For large $\eta_0$ this dielectric function becomes the value for spheres.

$$\varepsilon_{\ell m}(\omega) \xrightarrow[\eta_0 \to \infty]{} - \frac{(\ell + 1)}{\ell} \tag{2-89}$$

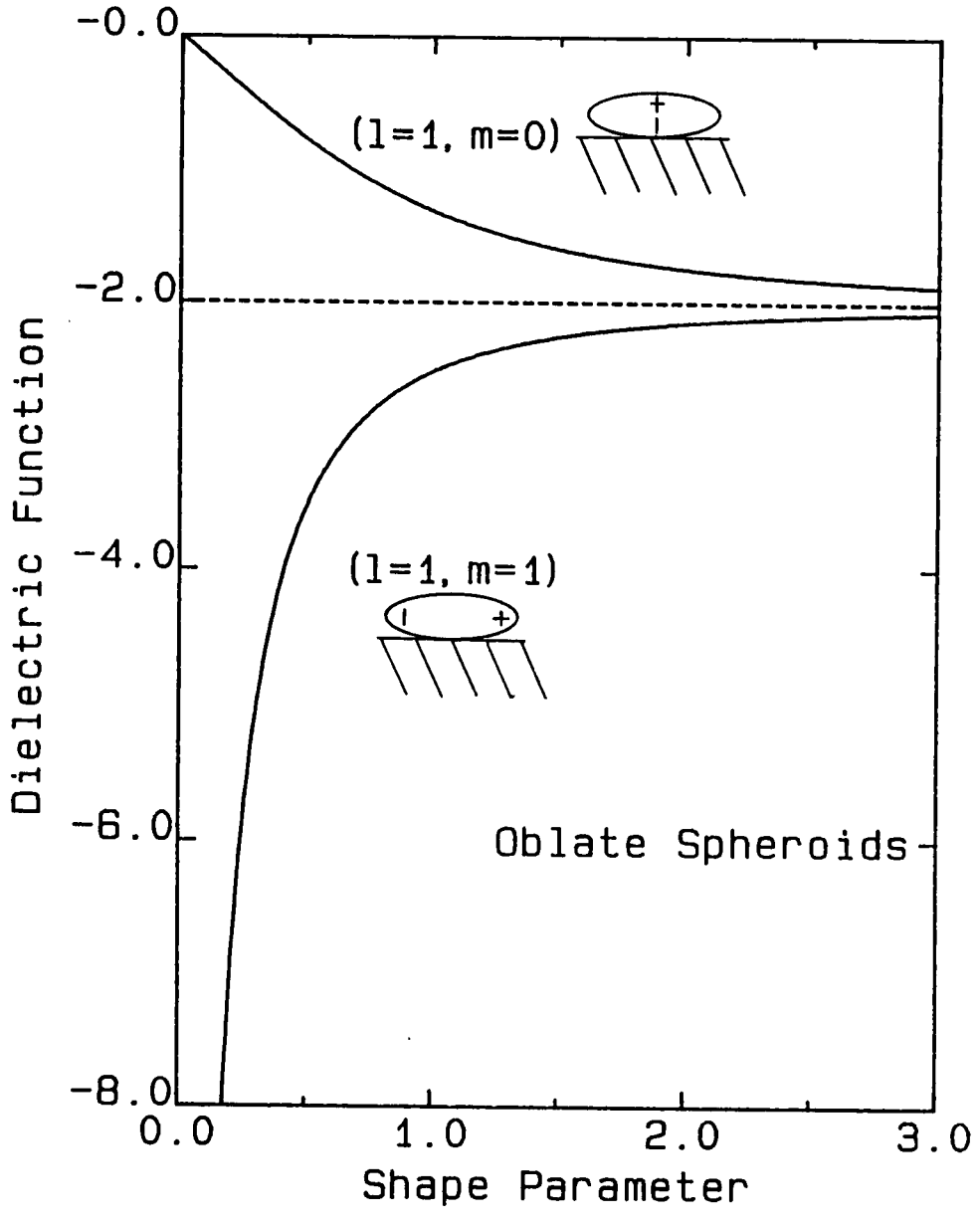



Figure 2-6. The dieleltric function for the two dipole modes of surface plasmon oscillations on oblate spheroids as a function of shape parameter. Large values of the shape parameter correspond to spherical particles, and small values correspond to disk-shaped particles.

Prolate Spheroidal Coordinates

For a prolate spheroid the solution to Laplace's equation inside and outside the spheroid are given in Appendix A. They are

$$\Phi_{in} = \sum_{\ell mp} \tilde{A}'_{\ell mp}\, Q_{\ell m}(\eta'_0)\, P_{\ell m}(\eta')\, Y^{p}_{\ell m}(\theta\phi) \tag{2-90}$$

$$\Phi_{out} = \sum_{\ell mp} \tilde{B}'_{\ell mp}\, Q_{\ell m}(\eta')\, P_{\ell m}(\eta'_0)\, Y^{p}_{\ell m}(\theta\phi) \ . \tag{2-91}$$

Here $P_{\ell m}$ and $Q_{\ell m}$ are the associated Legendre functions of real argument and $Y^{p}_{\ell m}$ are the real spherical harmonics. The $\ell$=1 terms of the Legendre functions of real argument are [2.16]

$$P_{10} = \eta' \tag{2-92}$$

$$P_{11} = (\eta'^2 - 1)^{\frac{1}{2}} \tag{2-93}$$

$$Q_{10} = \frac{\eta'}{2}\, \ell n\left(\frac{\eta' + 1}{\eta' - 1}\right) - 1 \tag{2-94}$$

$$Q_{11} = (\eta'^2 - 1)^{\frac{1}{2}}\left[\frac{1}{2}\, \ell n\left(\frac{\eta' + 1}{\eta' - 1}\right) + \frac{\eta'}{1 - \eta'^2}\right] \ . \tag{2-95}$$

Applying the boundary conditions (2-28) and (2-29) we get the dispersion relation for prolate spheroids.

$$\varepsilon(\omega) = \varepsilon_{\ell m}(\omega) \equiv \left.\frac{P_{\ell m}(\eta'_0)\, Q'_{\ell m}(\eta'_0)}{Q_{\ell m}(\eta'_0)\, P'_{\ell m}(\eta'_0)}\right|_{\eta' = \eta'_0} \tag{2-96}$$

Figure 2-7 shows the dielectric response function as a function of shape parameter for the prolate spheroidal geometry. The $\ell$=1 terms of the dielectric response function are

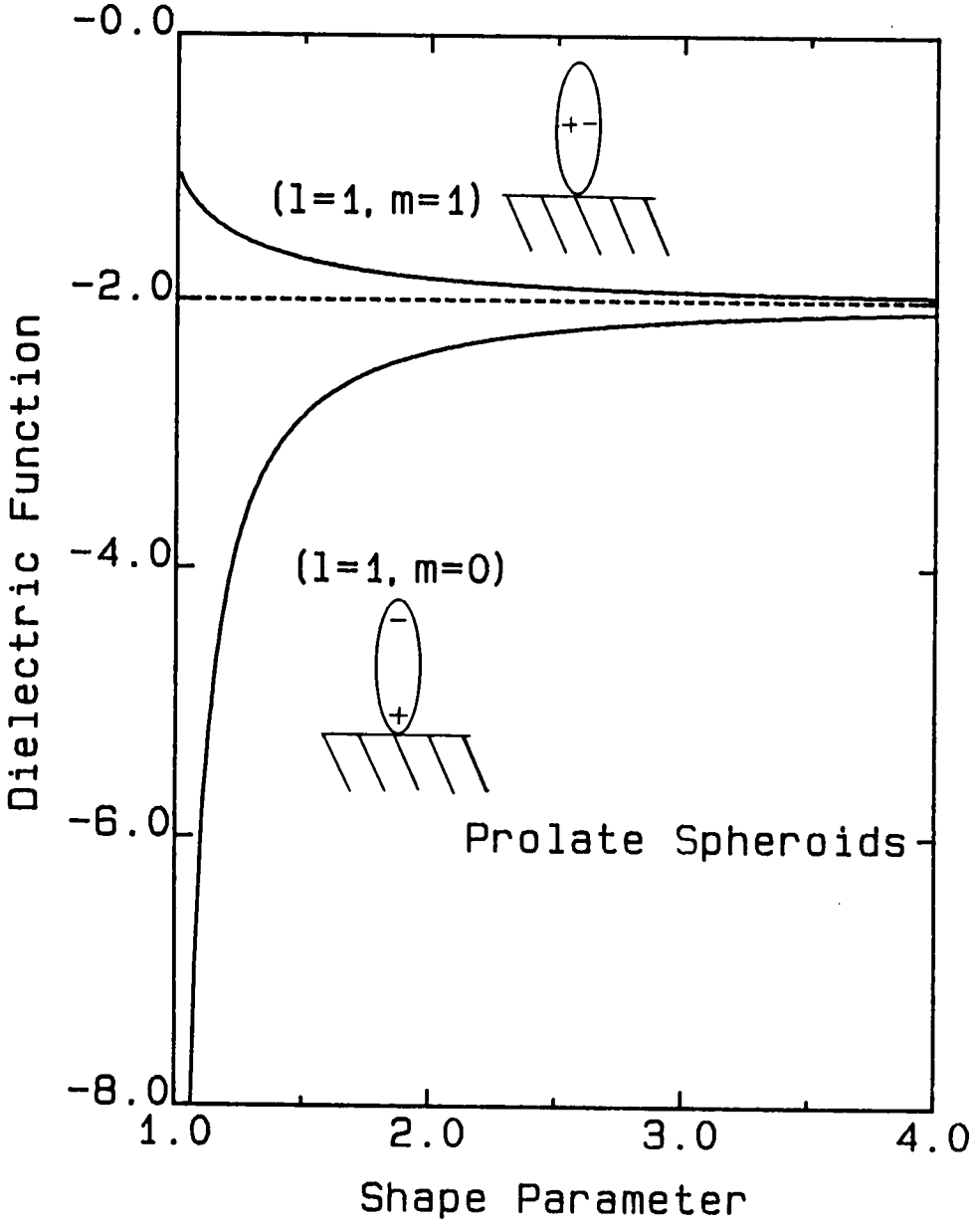



Figure 2-7. The dielectric function for the two dipole modes of surface plasmon oscillations on prolate spheroids as a function of shape parameter. Large values of the shape parameter correspond to spherical particles, and small values correspond to needle-shaped particles.

$$\varepsilon_{10}(\omega) = 1 + \frac{1}{(1 - \eta_0'^2)\,\frac{\eta_0'}{2}\,\ell n(\frac{\eta_0' + 1}{\eta_0' - 1}) + \eta_0'^2 - 1} \tag{2-97}$$

$$\varepsilon_{11}(\omega) = 1 - \frac{2}{(1 - \eta_0'^2)\,\frac{\eta_0'}{2}\,\ell n(\frac{\eta_0' + 1}{\eta_0' - 1}) + \eta_0'^2} \tag{2-98}$$

As in the oblate case for large $\eta_0'$ the dielectric function becomes the value for spheres.

$$\varepsilon_{\ell m}(\omega) \xrightarrow[\eta_0' \to \infty]{} - \frac{(\ell + 1)}{\ell} \tag{2-99}$$

We can also easily treat the case of a spheroid in a uniform field. By using the boundary conditions (2-28) and (2-29) the potentials for a prolate spheroid in a uniform time varying field (in the dipole approximation) can be written

$$\tilde{\Phi}_{in} = \sum_{mp} a\ \frac{\overline{4\pi}}{3}\,\tilde{E}_{1mp}\,\frac{W_{1m}}{Z_{1m}}\bigg|_{\eta'=\eta_0'} P_{1m}(\eta)\ Y^{P}_{1m}(\theta\phi) \tag{2-100}$$

$$\tilde{\Phi}_{out} = \sum_{mp} a\ \frac{\overline{4\pi}}{3}\,\tilde{E}_{1mp}\left\{\frac{P'_{1m}(\eta')[t-1]}{Z_{1m}(\eta')}\bigg|_{\eta'=\eta_0'} P_{1m}(\eta_0)\ Q_{1m}(\eta) - P_{1m}(\eta')\right\} Y^{P}_{1m}(\theta\phi)\ , \tag{2-101}$$

where

$$W_{1m}(\eta_0') = P_{1m}(\eta_0')\ Q'_{1m}(\eta')\bigg|_{\eta'=\eta_0'} - Q_{1m}(\eta_0')\ P'_{1m}(\eta')\bigg|_{\eta'=\eta_0'} \tag{2-102}$$

is the Wronskian for the Legendre functions and $Z_{1m}(\eta')$ is defined by

$$Z_{1\,m}(\eta') = \varepsilon(\omega)\, P'_{1\,m}(\eta') \Big|_{\eta'=\eta'_0} Q_{1\,m}(\eta'_0) - P_{1\,m}(\eta_0)\, Q'_{1\,m}(\eta'_0) \Big|_{\eta'=\eta'_0} \tag{2-103}$$

The surface charge density is found from the discontinuity in the normal component of the electric field vector

$$\left[(\vec{E}_{out} - \vec{E}) \cdot \hat{e}_{\eta'}\right]\Big|_{\eta'=\eta'_0} = 4\pi\sigma \tag{2-104}$$

where $\hat{e}_{\eta'}$ is the unit surface normal vector. This gives

$$\sigma = \frac{1}{4\pi} \sum_{mp} \hat{e}_{\eta'} \cdot (\nabla\Phi_{in} - \nabla\Phi_{out})\Big|_{\eta'=\eta'_0} . \tag{2-105}$$

Since we are considering an idealized surface charge density the volume charge density and the surface charge density are related by [2.17]

$$\rho = \frac{\sigma\, \delta(\eta - \eta_0)}{h_\eta} \tag{2-106}$$

or

$$\tilde{\rho} = - \frac{\delta(\eta' - \eta'_0)\sqrt{\frac{4\pi}{3}}}{4\pi a(\eta'^2 - \cos^2\theta)} \sum_{mp} \frac{(-1)^{m+1}(1+m)!\tilde{E}_{1\,mp} P'_{1\,m}(\eta') Y^{p}_{1\,m}(\theta\phi)}{\varepsilon(\omega) P'_{1\,m}(\eta') Q_{1\,m}(\eta'_0) - P_{1\,m}(\eta'_0) Q'_{1\,m}(\eta')}\Bigg|_{\eta'=\eta'_0} \tag{2-107}$$

where we have used the expression for the Wronskian in reference [2.18]. From the dipole volume charge density we can find the components of the induced dipole moment by integrating over the volume of the spheroid [2.19].

$$\tilde{p}_x = \int h_\eta \, d\eta \int h_\theta \, d\theta \int h_\phi \, d\phi \tilde{\rho} x \ , \tag{2-108}$$

with similar expressions for y and z. The dipole moment components are

$$\tilde{p}_x = \frac{-2a^3[\epsilon - 1](\eta_0'^2 - 1)^{\frac{1}{2}} P_{11}(\eta') \, \tilde{E}_x}{3[\epsilon(\omega) P_{11}'(\eta') Q_{11}(\eta_0') - P_{11}(\eta_0') Q_{11}'(\eta')]}\Bigg|_{\eta'=\eta_0'} = \alpha_x \tilde{E}_x \tag{2-109}$$

$$\tilde{p}_y = \frac{-2a^3[\epsilon - 1](\eta_0'^2 - 1)^{\frac{1}{2}} P_{11}'(\eta') \, \tilde{E}_y}{3[\epsilon(\omega) P_{11}'(\eta') Q_{11}(\eta_0') - P_{11}(\eta_0') Q_{11}'(\eta')]}\Bigg|_{\eta'=\eta_0'} = \alpha_y \tilde{E}_y \tag{2-110}$$

$$\tilde{p}_z = \frac{a^3 \eta_0' [\epsilon - 1] P_{10}'(\eta') \, \tilde{E}_z}{3[\epsilon(\omega) P_{10}'(\eta') Q_{10}(\eta_0') - P_{10}(\eta_0') Q_{10}'(\eta')]}\Bigg|_{\eta'=\eta_0'} = \alpha_z E_z \ . \tag{2-111}$$

Resonances in the spheroid correspond to a maximum in the dipole moment as a function of frequency. At the resonant frequency Re $\epsilon(\omega)=\epsilon_{\ell m}(\omega)$. We can obtain $\epsilon_{\ell m}(\eta_o')$ by setting the denominator of the dipole moment equal to zero. The dipole moment, however remains finite due to the imaginary part of $\epsilon(\omega)$.

Ellipsoidal Coordinates

For an ellipsoid the solutions to Laplace's equation are the ellipsoidal harmonics and are rather complicated. However following Stratton [2.20] we may construct a few elementary solutions that will

be sufficient for calculating the absorbance of light by ellipsoids in the dipole approximation.

In ellipsoidal coordinates Laplace's equation is

$$(\xi - \zeta)R_\eta \frac{\partial}{\partial \eta}\left(R_\eta \frac{\partial \Phi}{\partial \eta}\right) + (\zeta - \eta)R_\xi \frac{\partial}{\partial \xi}\left(R_\xi \frac{\partial \Phi}{\partial \xi}\right)$$

$$+ (\eta - \xi)\, R_\zeta \frac{\partial}{\partial \zeta}\left(R_\zeta \frac{\partial \Phi}{\partial \zeta}\right) = 0 \,, \qquad (2\text{-}112)$$

where $R_s$ has been defined in Eq. (2-67). We assume the ellipsoid surface is defined by $\eta=\eta_o$ and therefore the principal axes have lengths $(a^2+\eta_o)$, $(b^2+\eta_o)$ and $(c^2+\eta_o)$ from Eq. (2-58).

Now we consider an ellipsoid in a uniform time varying field $E_o$ which is directed arbitrarily with respect to the reference system and has known components $E_{ox}$ ,$E_{oy}$ ,$E_{oz}$ along the ellipsoid axes. We assume the ellipsoid has a dielectric function $\epsilon(\omega)$ and that it is immersed in a vacuum. If we first examine the $E_{ox}$ component, the Fourier frequency component of the potential outside the ellipsoid will be

$$\tilde{\Phi}_{out} = \tilde{\Phi}_0 + \tilde{\Phi}_{1\,out} \qquad (2\text{-}113)$$

where $\tilde{\Phi}_o$ is the potential of the applied field in the dipole approximation,

$$\tilde{\Phi}_0 = -\tilde{E}_{ox}x = -\tilde{E}_{ox}\left[\frac{(\eta + a^2)(\xi + a^2)(\zeta + a^2)}{(b^2 - a^2)(c^2 - a^2)}\right]^{\frac{1}{2}} = \tilde{C}_1 F_1(\eta)F_2(\xi)F_3(\zeta) \,, \qquad (2\text{-}114)$$

and $\tilde{\Phi}_{1out}$ is the potential due to the ellipsoid. When the boundary conditions are satisfied, the induced potential, $\tilde{\Phi}_{1out}$, will vary functionally over the surface $\eta$=constant in exactly the same manner as $\tilde{\Phi}_o$. It will, however, be regular at infinity. We presume, then, that $\tilde{\Phi}_{1out}$ is a function of the form

$$\tilde{\Phi}_{1\ out} = \tilde{C}_2 G_1(\eta) F_2(\xi) F_3(\zeta) \tag{2-115}$$

where $F_2(\xi)=(\xi+a^2)^{1/2}$ and $F_3(\zeta)=(\zeta+a^2)^{1/2}$.

If we substitute Eq. (2-114) into Laplace's equation, the result is an ordinary second-order differential equation which has two solutions. We already know $F_1(\eta)=(\eta+a^2)^{1/2}$ is a solution. To find $G_1(\eta)$ we use [2.21]

$$y_2(x) = y_1(x) \int \frac{e^{-\int p(x_1)dx_1}}{[y_1(x)]^2} dx , \tag{2-116}$$

where $y_1(x)=F_1(\eta)$ and $P(x_1)=\frac{1}{R_\eta} = \frac{d}{d\eta}(\ell nR)$. This yields the induced potential

$$\tilde{\Phi}_{1\ out} = \tilde{\Phi}_0 \frac{\tilde{C}_2}{\tilde{C}_1} \int_{\eta_0}^{\infty} \frac{d\eta}{(\eta + a^2)R_\eta} \tag{2-117}$$

and so the potential outside the ellipsoid is

$$\tilde{\Phi}_{out} = F_1(\eta)F_2(\xi)F_3(\zeta) \left[\tilde{C}_1 + \tilde{C}_2 \int_{\eta_0}^{\infty} \frac{ds}{(s + a^2)R_s}\right] \tag{2-118}$$

where $F_1(\eta), F_2(\xi), F_3(\zeta)$, and $\tilde{C}_1$ are determined from $\Phi_o$. The s is a dummy integration variable. Similarly inside the ellipsoid

$$\tilde{\Phi}_{in} = \tilde{C}_3 F_1(\eta) F_2(\xi) F_3(\zeta) \ . \tag{2-119}$$

The constants $\tilde{C}_2$ and $\tilde{C}_3$ are determined by the boundary conditions (2-28) and (2-29). And so since $\tilde{\Phi}_o = -\tilde{E}_{ox} x$ the potential inside the ellipsoid due to the x-component of the field is

$$\tilde{\Phi}_{in} = \frac{-\tilde{E}_{ox} x}{1 + \frac{R_{\eta_0}}{2} [\varepsilon(\omega) - 1] A_1} \tag{2-120}$$

with

$$A_1 = \int_{\eta_0}^{\infty} \frac{ds}{(s + a^2) R_s}$$

and the field inside is

$$\tilde{E}_{x_{in}} = \frac{\tilde{E}_{ox}}{1 + \frac{R_{\eta_0}}{2} [\varepsilon - 1] A_1} \ . \tag{2-121}$$

We obtain the other field components and the resultant potentials by simply replacing the parameter $a^2$ by $b^2$ or $c^2$ in the $(s+a^2)$ term of $A_1$ and $E_{ox}$ by $E_{oy}$ or $E_{oz}$.

Outside the ellipsoid the potential due to the x-component of the field is obtained from Eq. (2-118).

$$\tilde{\Phi}_{out} = \tilde{\Phi}_0 \frac{1 + \frac{R_{\eta_0}}{2}[\varepsilon - 1)\int_{\eta_0}^{\eta} \frac{ds}{(s + a^2)R_s}}{1 + \frac{R_{\eta_0}}{2}[\varepsilon - 1]\int_{\eta_0}^{\infty} \frac{ds}{(s + a^2)R_s}}, \tag{2-122}$$

with corresponding potentials for the y and z components. To obtain the dispersion relation for ellipsoids we set $C_1$ equal to zero in Eq. (2-118) and apply the boundary conditions (2-28) and (2-29).

$$\tilde{\Phi}_{in}\Big|_{\eta=\eta_0} = \tilde{\Phi}_{out}\Big|_{\eta=\eta_0} \tag{2-28}$$

$$\varepsilon(\omega)\hat{e}_\eta \cdot \nabla\tilde{\Phi}_{in}\Big|_{\eta=\eta_0} = \tilde{e}_\eta \cdot \nabla\tilde{\Phi}_{out}\Big|_{\eta=\eta_0} . \tag{2-29}$$

These respectively yield the equations

$$\tilde{C}_3 = \tilde{C}_2 A_1 \tag{2-123}$$

and

$$\frac{\varepsilon_1(\omega)\tilde{C}_3}{2(\eta_0 + a^2)^{\frac{1}{2}}} = \frac{\tilde{C}_2 A_1}{2(\eta_0 + a^2)^{\frac{1}{2}}} + (\eta_0 + a^2)^{\frac{1}{2}}\left[\frac{-\tilde{C}_2}{(\eta_0 + a^2)R_{\eta_0}}\right]. \tag{2-124}$$

Solving for $\epsilon_1(\omega)$ the dispersion relation is

$$\varepsilon_1(\omega) = 1 - \frac{2}{R_{\eta_0} A_1} . \tag{2-125}$$

This yields the allowed values of resonance for charge-density oscillations along the a-axis of the ellipsoid (parallel to the x-axis). To obtain the b-axis or the c-axis resonance we simply

replace $A_1$ by $A_2$ or $A_3$ respectively where

$$A_2 = \int_{\eta_0}^{\infty} \frac{ds}{(s + b^2)R_s} , \tag{2-126}$$

$$A_3 = \int_{\eta_0}^{\infty} \frac{ds}{(s + c^2)R_s} . \tag{2-127}$$

Figure 2-8 shows the dielectric response as a function of shape for the three resonant modes in ellipsoidal geometry.

## F. THE SPHEROIDAL AND SPHERICAL LIMITS

Oblate and prolate coordinates are special cases of ellipsoidal coordinates. If two of the ellipsoidal axes are equal in length then the integral in the dispersion relation may be evaluated analytically and the dispersion relation reduces to the values for oblate and prolate spheroids.

If a=b>c then the ellipsoid is an oblate spheroid and

$$\varepsilon_1(\omega) = \varepsilon_2(\omega) = 1 - \frac{2}{(\eta_0 + a^2)(\eta_0 + c^2)^{\frac{1}{2}} \int_{\eta_0}^{\infty} \frac{ds}{(s + a^2)^2(s + c^2)^{\frac{1}{2}}}} \tag{2-128}$$

Calling the integral I, integration by parts gives

$$I = \frac{(s + c^2)^{\frac{1}{2}}}{(a^2 - c^2)(s + a^2)}\Bigg|_{\eta_0}^{\infty} + \frac{1}{2(a^2 - c^2)} \int_{\eta_0}^{\infty} \frac{ds}{(s + a^2)(s + c^2)^{\frac{1}{2}}} . \tag{2-129}$$

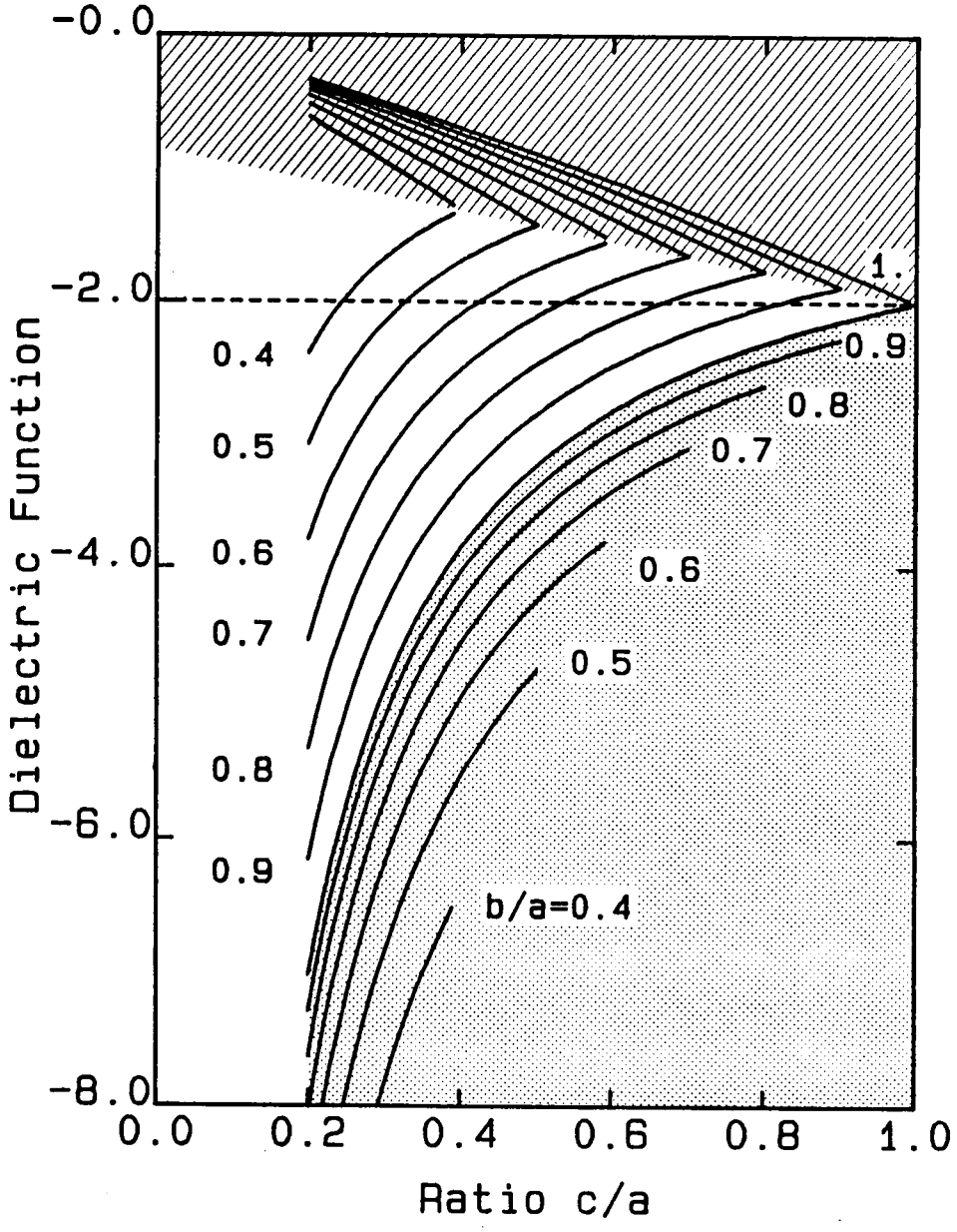



Figure 2-8. Dielectric response as a function of axis ratio c/a for values of the ratio b/a for resonant charge-density-oscillation modes in silver ellipsoids. Mode 1 is oscillations along the a axis shown in the dotted area, mode 2 is oscillations along the b-axis shown in the unshaded area, and mode 3 is oscillations along the c axis shown in the hatched area.

Evaluating the integral in the second term [2.22] and using the identity $\cot^{-1}x=\pi/2-\tan^{-1}x$

$$I = \frac{-(\eta_0 + c^2)^{\frac{1}{2}}}{(a^2 - c^2)(a^2 + \eta_0)} + \frac{1}{2(a^2 - c^2)} \left\{ \frac{2}{(a^2 - c^2)^{\frac{1}{2}}} \cot^{-1}\left[\frac{\eta_0 + c^2}{a^2 - c^2}\right] \right\} . \tag{2-130}$$

If we note that $a^2-c^2=\eta_0+a^2-(\eta_0+c^2)$ and let $(\eta_0+a^2) = r_0(1+\eta_0)^{\frac{1}{2}}$ and $(\eta_0+c^2)^{\frac{1}{2}}=r_0\eta$ where $\eta$ is the shape parameter and $r_0$ is the semimajor axis for oblate spheroids then

$$(\eta_0 + a^2)(\eta_0 + c^2)^{\frac{1}{2}} \int_{\eta_0}^{\infty} \frac{ds}{(s + a^2)(s + c^2)^{\frac{1}{2}}}$$

becomes

$$\eta(1 + \eta^2) \cot^{-1}\eta - \eta^2 ,$$

and

$$\varepsilon_2 = \varepsilon_2 = \varepsilon_{11} = 1 - \frac{2}{\eta(1 + \eta^2) \cot^{-1}\eta - \eta^2} . \tag{2-88}$$

This is the same result obtained in the oblate calculation for the ($\ell$=1,m=1) mode . For $\epsilon_3(\omega)$ we have

$$\varepsilon_3(\omega) = 1 - \frac{1}{(\eta_0 + a^2)(\eta_0 + c^2) \int_{\eta_0}^{\infty} \frac{ds}{(s + c^2)^{3/2}(s + a^2)}} \tag{2-131}$$

Again calling the integral I, integration by parts gives

$$I = \frac{-2}{(s + c^2)^{\frac{1}{2}}(s + a^2)}\Bigg|_{\eta_0}^{\infty} - 2\int_{\eta_0}^{\infty} \frac{ds}{(s + c^2)^{\frac{1}{2}}(s + a^2)^2} . \qquad (2\text{-}132)$$

The second term is the same integral evaluated previously, so carrying out the integration and substituting the spheroidal parameters gives

$$(\eta_0 + a^2)(\eta_0 + c^2)^{\frac{1}{2}} \int_{\eta_0}^{\infty} \frac{ds}{(s + c^2)^{3/2}(s + a^2)} = -2\eta(1 + \eta^2)\cot^{-1}\eta + 2\eta^2 . \qquad (2\text{-}133)$$

So the result is the allowed values of the dielectric function for the ($\ell$=1,m=0) mode in oblate coordinates;

$$\varepsilon_3(\omega) = \varepsilon_{10}(\omega) = 1 + \frac{1}{\eta(1 + \eta^2)\cot^{-1}\eta - (1 + \eta^2)} . \qquad (2\text{-}87)$$

For prolate spheroids a>b=c and so

$$\varepsilon_2 = \varepsilon_3 = 1 - \frac{2}{(\eta_0 + a^2)^{\frac{1}{2}}(\eta_0 + c^2)\int_{\eta_0}^{\infty}(s + c^2)(s + a^2)^{\frac{1}{2}}} . \qquad (2\text{-}134)$$

The integral is the same form as the one in Eq. (2-129) so

$$I = \frac{(s + a^2)^{\frac{1}{2}}}{(c^2 - a^2)(s + c^2)}\Bigg|_{\eta_0}^{\infty} + \frac{1}{2(c^2 - a^2)}\int_{\eta_0}^{\infty} \frac{ds}{(s + c^2)(s + a^2)^{\frac{1}{2}}} . \qquad (2\text{-}135)$$

Evaluating the integral in the second term and using a different form of the result [2.22] we get

$$I = \frac{-(\eta_0 + a^2)}{(c^2 - a^2)(\eta_0 + c^2)} + \frac{1}{2(c^2 - a^2)} \left[ \frac{1}{(a^2 - c^2)} \ln \left( \frac{(\eta_0 + a^2) + (a^2 - c^2)}{(\eta_0 + a^2) - (a^2 - c^2)} \right) \right].$$

(2-136)

If we let $(\eta_0+a^2)^{1/2}=r_0$ and $(\eta_0+c^2)^{1/2}=r_0(\eta^2-1)^{1/2}$ with $\eta$ and $r_0$ the shape parameter and semimajor axis for prolate spheroids, then

$$(\eta_0 + a^2)^{1/2}(\eta_0 + c^2) \int_{\eta_0}^{\infty} \frac{ds}{(s + c^2)(s + a^2)^{1/2}} = \eta^2 + \frac{\eta}{2} (1 - \eta^2) \, n\left(\frac{\eta + 1}{\eta - 1}\right)$$

(2-137)

and

$$\varepsilon_2 = \varepsilon_3 = \varepsilon_{11}(\omega) = 1 - \frac{\eta(1 - \eta^2)}{2} \ln\left(\frac{\eta + 1}{\eta - 1}\right) + \eta^2 \, . \qquad (2\text{-}89)$$

This is the ($\ell$=1,m=1) mode for prolate spheroids. For $\varepsilon_1$,

$$\varepsilon_1 = 1 - \frac{2}{(\eta_0 + c^2)(\eta_0 + a^2)^{1/2} \int_{\eta_0}^{\infty} \frac{ds}{(s + a^2)\,(s + c^2)^{1/2}}} \qquad (2\text{-}138)$$

The integral has the same form as in Eq. (2-132). Evaluating the integral and substituting the prolate parameters gives

$$\varepsilon_1 = \varepsilon_{10}(\omega) = 1 + \frac{1}{\eta^2 - 1 + \frac{1}{2} \eta(1 - \eta^2) \ln\left(\frac{\eta + 1}{\eta - 1}\right)} \qquad (2\text{-}97)$$

The result is the ($\ell$=1,m=0) mode for prolate spheroids.

For $\eta_0$ large compared with $a^2, b^2$, or $c^2$, $R_{\eta_0}$ approaches $\eta_0^{3/2}$ so that

$$A_{\eta_0} = \int_{\eta_0}^{\infty} \frac{ds}{s^{5/2}} \tag{2-139}$$

and performing the integration

$$A_{\eta_0} = \frac{2}{3} \eta_0^{-3/2} , \tag{2-140}$$

so the dielectric function is

$$\varepsilon_1 \xrightarrow[\eta_0 \to \infty]{} 1 - \frac{1}{\eta_0^{3/2}(\frac{2}{3} \eta_0^{-3/2})} = -2 . \tag{2-141}$$

Thus for large values of $\eta_0$ the dielectric function becomes the value for spheres.

## G. DIPOLE MOMENTS AND THE POLARIZABILITY

In order to calculate the optical absorbance for spheroidal and ellipsoidal particles we require the total electromagnetic cross section. The cross section is obtained by using the dipole moment or equivalently the polarizability. We have calculated the dipole moment for a prolate spheroid in vacuum in Eq.'s (2-109)-(2-111) and the dipole moment for an oblate spheroid has been previously calculated [2-23].

For any dielectric we recall

$$\vec{D} = \vec{E}_{in} + 4\pi\vec{P} \ , \tag{2-142}$$

in Gaussian units, where $\vec{D}$ is the displacement vector and $\vec{P}$ is the polarization vector. Since the dielectric is linear and isotropic we write

$$\vec{P} = \frac{[\varepsilon - 1]}{4\pi} \vec{E}_{in} \ . \tag{2-143}$$

Using $\vec{E}_{in}$ from Eq. (2-121) the x-component of the polarization vector for an ellipsoid is

$$P_x = \frac{[\varepsilon - 1]E_{ox}}{4\pi(1 + \frac{R_{\eta_0}}{2} [\varepsilon - 1]A_1)} \tag{2-144}$$

The polarization vector is the dipole moment per unit volume. Using the volume of an ellipsoid, the x-component of the dipole moment is

$$p_x = \frac{2abc[\varepsilon(\omega) - 1]/3}{2 + R_{\eta_0} A_1[\varepsilon(\omega) - 1]} E_{ox} \ . \tag{2-145}$$

Writing the dipole moment in terms of the allowed values of the dielectric function we get

$$p_x = \frac{abc[\varepsilon(\omega) - 1]/3}{1 - \frac{\varepsilon(\omega) - 1}{\varepsilon_1(\omega) - 1}} E_{ox} \ . \tag{2-146}$$

Since $p_x = \alpha_x E_{ox}$ then

$$\alpha_x = \frac{abc[\epsilon(\omega) - 1]/3}{1 - \frac{\epsilon(\omega) - 1}{\epsilon_1(\omega) - 1}} . \qquad (2\text{-}147)$$

We obtain $\alpha_y$ or $\alpha_z$ by replacing $\epsilon_1(\omega)$ with $\epsilon_2(\omega)$ or $\epsilon_3(\omega)$ respectively. As in spheroidal calculations there is a maximum in the dipole moment when Re $\epsilon(\omega)=\epsilon_i(\omega)$ with i=1,2 or 3.

## H. CROSS SECTIONS

From the expression for the induced dipole moments the scattered fields in the far (radiation) zone may be calculated using [2.24]

$$\vec{E}_{sca} = \frac{\omega^2 e^{ikr}}{c^2 r} [(\hat{n} \times \vec{p}) \times \hat{n}] . \qquad (2\text{-}148)$$

$\hat{n}$ is a unit vector in the observation direction, r is the distance from the scatterer and $\vec{p}$ is the dipole moment of the scatterer.

The total or extinction cross section is defined as the ratio of the total power taken from the incident wave to incident power per unit area. It may be obtained using the optical theorem [2.25]. The total cross section is the sum of the scattering and absorption cross sections.

If we consider a scatterer with an incident plane monocromatic wave then the scattered fields propagate outward and are observed at some distant point. The total fields at all points in space are the sum of the incident fields and the scattered fields. So

$$E = E_i + E_s \qquad B = B_i + B_s \ , \tag{2-149}$$

where $E_i$ and $B_i$ are the incident fields and $E_s$ and $B_s$ are the scattered fields. We assume the scatterers are dissapative and will absorb energy from the incident wave. The absorbed power can be calculated by integrating the inward-going component of the Poynting vector of the total fields over a sphere that encloses the scatterer;

$$P_{abs} = -\frac{c}{8\pi} \oint_{sphere} Re(\vec{E} \times \vec{B}^*) \cdot \hat{n} da \ . \tag{2-150}$$

Here $\hat{n}$ is the outwardly directed normal to the sphere of integration and thus the minus sign is required. If we use Eqs. (2-149), then the power absorbed is

$$P_{abs} = -\frac{c}{8\pi} \oint_{sphere} Re[\vec{E}_i \times \vec{B}_i^* + \vec{E}_s \times \vec{B}_i^* + \vec{E}_i \times \vec{B}_s^* + \vec{E}_s \times \vec{B}_s^*] \cdot \hat{n} da. \tag{2-151}$$

The scattered power can be evaluated as an integral over a sphere of the outwardly directed component of the scattered Poynting vector;

$$P_{scatt} = \frac{c}{8\pi} \oint_{sphere} Re[\vec{E}_s \times \vec{B}_s^*] \cdot \hat{n} da \ . \tag{2-152}$$

So the total power taken from the incident beam by the scatterer is the sum of the absorbed and scattered power,

$$P_{tot} = -\frac{c}{8\pi}\oint_{sphere} Re[\vec{E}_i \times \vec{B}_i^* + \vec{E}_i \times \vec{B}_s^* + \vec{E}_s \times \vec{B}_i^*] \cdot \hat{n}da \ . \quad (2\text{-}153)$$

The first term is the time-averaged Poynting vector of the incident wave and is zero. So

$$P_{tot} = -\frac{c}{8\pi}\oint_{sphere} Re[\vec{E}_i \times \vec{B}_s^* + \vec{E}_s \times \vec{B}_i^*] \cdot \hat{n}da \ . \quad (2\text{-}154)$$

Now the incident power per unit area is [2.25]

$$\frac{P_{inc}}{area} = \frac{c}{8\pi}|E_0|^2 \ , \quad (2\text{-}155)$$

so the total cross section is

$$\sigma_{tot} = \frac{-\frac{c}{8\pi}\oint_{sphere} Re[\vec{E}_i \times \vec{B}_s^* + \vec{E}_s \times \vec{B}_i^*] \cdot \hat{n}da}{\frac{c}{8\pi}|E_0|^2} \ . \quad (2\text{-}156)$$

In the far zone the electromagnetic wave is transverse and the vacuum electric and magnetic fields are related by

$$\vec{B} = \hat{n} \times \vec{E} \ . \quad (2\text{-}157)$$

Using this relationship we write the total cross section as

$$\sigma_{tot} = -\frac{\oint_{sphere} Re[\vec{E}_i \times (\hat{n} \times E_s^*) + \vec{E}_s \times (\hat{n}_i \times \vec{E}_i^*)] \cdot \hat{n}da}{|E_0|^2} \ , \quad (2\text{-}158)$$

where $\hat{n}_i$ is a unit vector in the direction of propagation of the incident wave. The two unit vectors, $\hat{n}$ and $\hat{n}_i$, may be written in terms of Cartesian coordinates;

$$\hat{n} = \sin\theta \cos\phi\ \hat{i} + \sin\theta \sin\phi\ \hat{j} - \cos\theta\ \hat{k} \qquad (2\text{-}159)$$

$$\hat{n}_i = \sin\Theta \cos\Phi\ \hat{i} + \sin\Theta \sin\Phi\ \hat{j} - \cos\Theta\ \hat{k}\ . \qquad (2\text{-}160)$$

Here we assume that the point of observation is on the minus z side of the x-y plane and that the angles and are measured with respect to the positive z-axis as illustrated in figure 2-9.

We will consider incident light that is polarized either in the plane of incidence (p-polarization) or perpendicular to the plane of incidence (s-polarization). The plane of incidence is defined by the propagation vector of the incident light ($\hat{n}_i$) and the normal vector to the sample surface (the z-axis). The incident electric fields are

$$E_i\Big|_{s\text{-}pol} = E_0 e^{i\vec{k}\cdot\vec{r}}(-\sin\Phi\ \hat{i} + \cos\Phi\ \hat{j})\ , \qquad (2\text{-}161)$$

$$E_i\Big|_{p\text{-}pol} = E_0 e^{i\vec{k}\cdot\vec{r}}(\cos\Theta(\cos\Phi\ \hat{i} + \sin\Phi\ \hat{j}) + \sin\Theta\ \hat{k})\ . \qquad (2\text{-}162)$$

The induced dipole moment is $\overleftrightarrow{p}=\overleftrightarrow{\alpha}\ \vec{E}$ and thus takes the form of the incident electric field except that it is calculated in the vicinity of the source and therefore the term $e^{i\vec{k}\cdot\vec{r}}\approx 1$. With these expressions we can evaluate the cross sections from Eq. (2-158).

For oblate and prolate spheroids we have symmetry about the z-axis so that calculations should be independent of the azimuthal angle $\Phi$

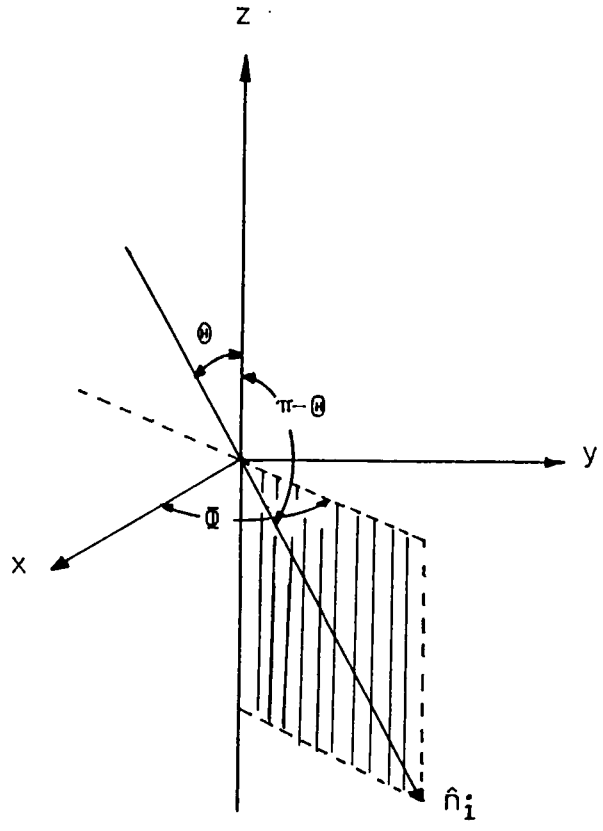



Figure 2-9. The angles Θ and Φ that the incident propagation vector $n_i$ makes with respect to the z- and x-axes.

associated with the incident wave. Therefore $\hat{n}_i$ and the expressions for the incident electric fields reduce to

$$\hat{n}_i = \sin\theta\, \hat{j} - \cos\theta\, \hat{k} , \tag{2-163}$$

$$\vec{E}_i\Big|_{s\text{-pol}} = E_0 e^{i\vec{k}\cdot\vec{r}}\, \hat{i} , \tag{2-164}$$

$$\vec{E}_i\Big|_{p\text{-pol}} = E_0 e^{i\vec{k}\cdot\vec{r}}(\cos\theta\, \hat{j} + \sin\theta\, \hat{k}) . \tag{2-165}$$

Evaluation of the oblate cross sections have been carried out previously [2.26] and the results are

$$\sigma_{tot}\Big|_{s\text{-pol}} = \frac{4\pi\omega}{c} \operatorname{Im} \alpha_x , \tag{2-166}$$

$$\sigma_{tot}\Big|_{p\text{-pol}} = \frac{4\pi\omega}{c} (\operatorname{Im} \alpha_x \cos^2\theta + \operatorname{Im} \alpha_z \sin^2\theta) . \tag{2-167}$$

The prolate cross sections have an identical form and will differ only in the expressions of the polarizabilities.

For ellipsoids there is no azimuthal symmetry and so we use Eqs. (2-159),(2-160),(2-161), and (2-162). For s-polarization we use Eq. (2-161) and the dipole moment is

$$\vec{P} = E_0(-\alpha_x \sin\Phi\, \hat{i} + \alpha_y \cos\Phi\, \hat{j}) . \tag{2-168}$$

Figure 2-10 shows the relationship between the incident electric vector and the coordinate system for s-polarization. Carrying out this calculation we find

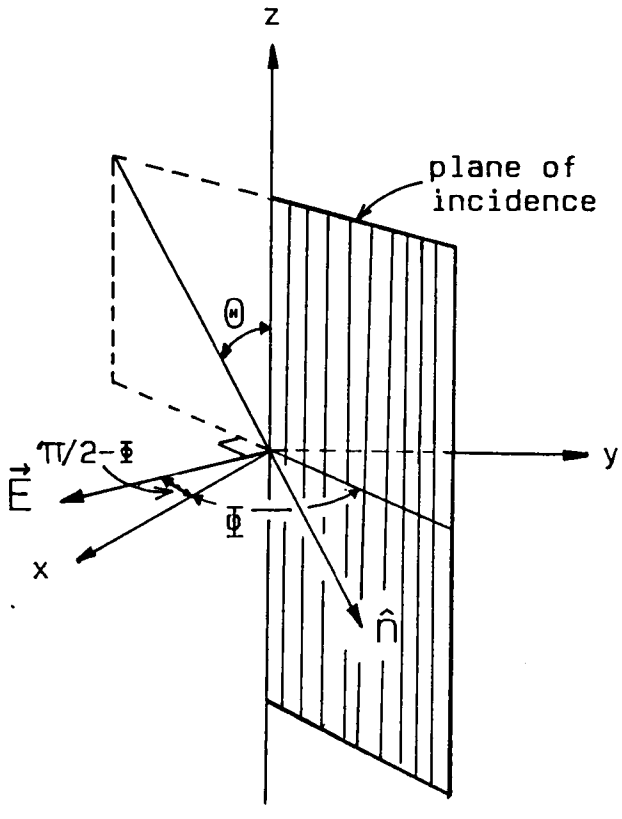



Figure 2-10. The relationship between the incident electric vector and the coordinate axes for s-polarization. The angles of incidence $\Theta$ and $\Phi$ are shown along with the plane of incidence and the propagation vector.

$$\sigma_{tot}\Big|_{s\text{-}pol} = \frac{4\pi\omega}{c}\left[\text{Im}\ \alpha_x \sin^2\Phi + \text{Im}\ \alpha_y \cos^2\Phi\right] . \qquad (2\text{-}169)$$

For p-polarization we use Eq. (2-162) and the dipole moment is

$$\vec{P} = E_0(\alpha_x \cos\Theta \cos\Phi\ \hat{i} + \alpha_y \cos\Theta \sin\Phi\ \hat{j} + \alpha_z \sin\Theta\ \hat{k}) . \qquad (2\text{-}170)$$

Figure 2-11 shows the relationship between the incident electric field and the coordinate system for p-polarization. Evaluating Eq. (2-158) we find

$$\sigma_{tot}\Big|_{p\text{-}pol} = \frac{4\pi\omega}{c}\left[(\text{Im}\ \alpha_x \cos^2\Phi + \text{Im}\ \alpha_y \sin^2\Phi)\cos^2\Theta + \text{Im}\ \alpha_z \sin^2\Theta\right] . \qquad (2\text{-}171)$$

The details of the evaluation of the cross section for each polarization is straightforward but long. The major steps in evaluating the cross sections are included in Appendix B.

It is important to distinguish between the part of the total cross section due to scattering and the part due to absorption. We define the scattering cross section as the ratio of the scattered power to the incident power per unit area [2.27].

$$\sigma_{sca} = \frac{\frac{c}{8\pi}\oint_{sphere} \text{Re}[\vec{E}_{sca} \times \vec{B}^*_{sca}] \cdot \hat{n}\,da}{\frac{c}{8\pi}\,\text{Re}\,|E_0|^2} \qquad (2\text{-}172)$$

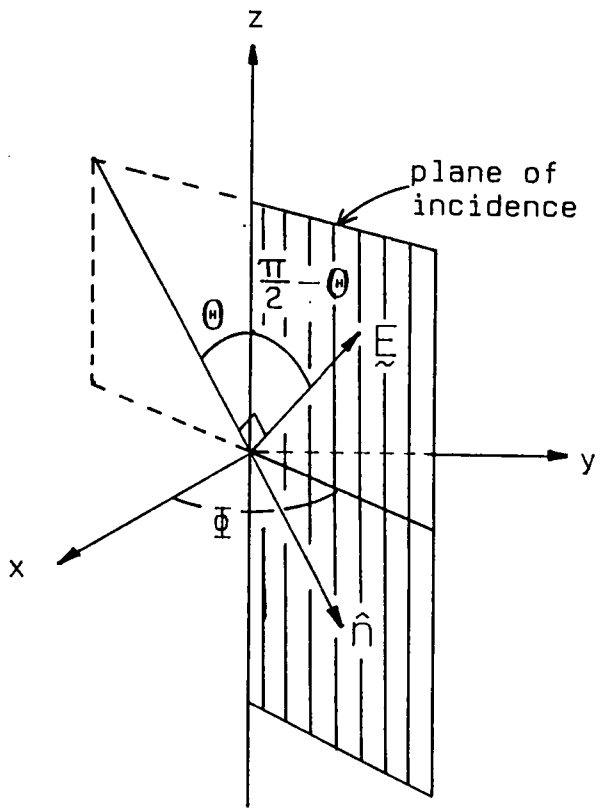



Figure 2-11. The relationship between the incident electric vector and the coordinate axes for p-polarization. The angles of incidence $\Theta$ and $\Phi$ are shown along with the plane of incidence and the propagation vector.

Carrying out this calculation we find that for spheroids [2.28]

$$\sigma_{sca}\Big|_{s\text{-}pol} = \frac{8\pi\omega^4}{3c^4} |\alpha_x|^2 \tag{2-173}$$

and

$$\sigma_{sca}\Big|_{p\text{-}pol} = \frac{8\pi\omega^4}{3c^4} [|\alpha_y|^2 \cos^2\Theta + |\alpha_z|^2 \sin^2\Theta] . \tag{2-174}$$

For ellipsoids we find

$$\sigma_{sca}\Big|_{s\text{-}pol} = \frac{8\pi\omega^4}{3c^4} [|\alpha_x|^2 \sin^2\Phi + |\alpha_y|^2 \cos^2\Phi] \tag{2-175}$$

and

$$\sigma_{sca}\Big|_{p\text{-}pol} = \frac{8\pi\omega^4}{3c^4} [(|\alpha_x|^2 \cos^2\Phi + |\alpha_y|^2 \sin^2\Phi)\cos^2\Theta + |\alpha_z|^2 \sin^2\Theta] . \tag{2-176}$$

The absorption cross section may be found by subtracting the scattering cross section from the total cross section for each polarization.

A maximum in the cross sction occurs when there is a minimum in the denominator of the polarizability expressions (see Eq. 2-147). Therefore a peak in the cross section will occur where Re $\epsilon(\omega)=\epsilon_i(\omega)$. The polarizability remains finite, however, due to the imaginary part of the dielectric function $\epsilon(\omega)$. The dielectric function is obtained from the bulk optical data [2.29] for the material from which the

spheroid or ellipsoid is formed. Figures 2-12 and 2-13 are plots of oblate and prolate mode energies for the resonant dipole modes of silver spheroids. Figure 2-14 is a plot of the mode energies for the resonant dipole modes of ellipsoidal silver particles.

Each component of the polarizability is associated with a different resonant mode for an ellipsoid. For spheroids, by symmetry, $\alpha_x=\alpha_y$ and so we only have a single resonance mode for the x and y directions. For each polarizability component in the cross section expressions, we should expect a corresponding maximum in the cross section. By examining the expression for the polarizabilities in each case, we see that the total cross sections are proportional to $V\lambda^{-1}$ while the scattering cross sections are proportional to $V^2\lambda^{-4}$. This implies a much stronger dependence on wavelength and particle size for the scattering cross section. However comparing calculations of the total and scattering cross section we have found that the ratio of the scattering cross section to the total cross section is constant if the particle volume is held constant and the shape is changed. The change in shape changes the wavelength of the peak resonance and also the magnitude of the dielectric function terms so that the cross section ratio remains constant. On the other hand, if the volume is allowed to change then the ratio of scattering to total cross section changes in proportion to the volume. Figure 2-15 shows the scattering to total cross section ratio as a function of wavelength for different shapes of ellipsoids. The ellipsoid volume is not held constant.

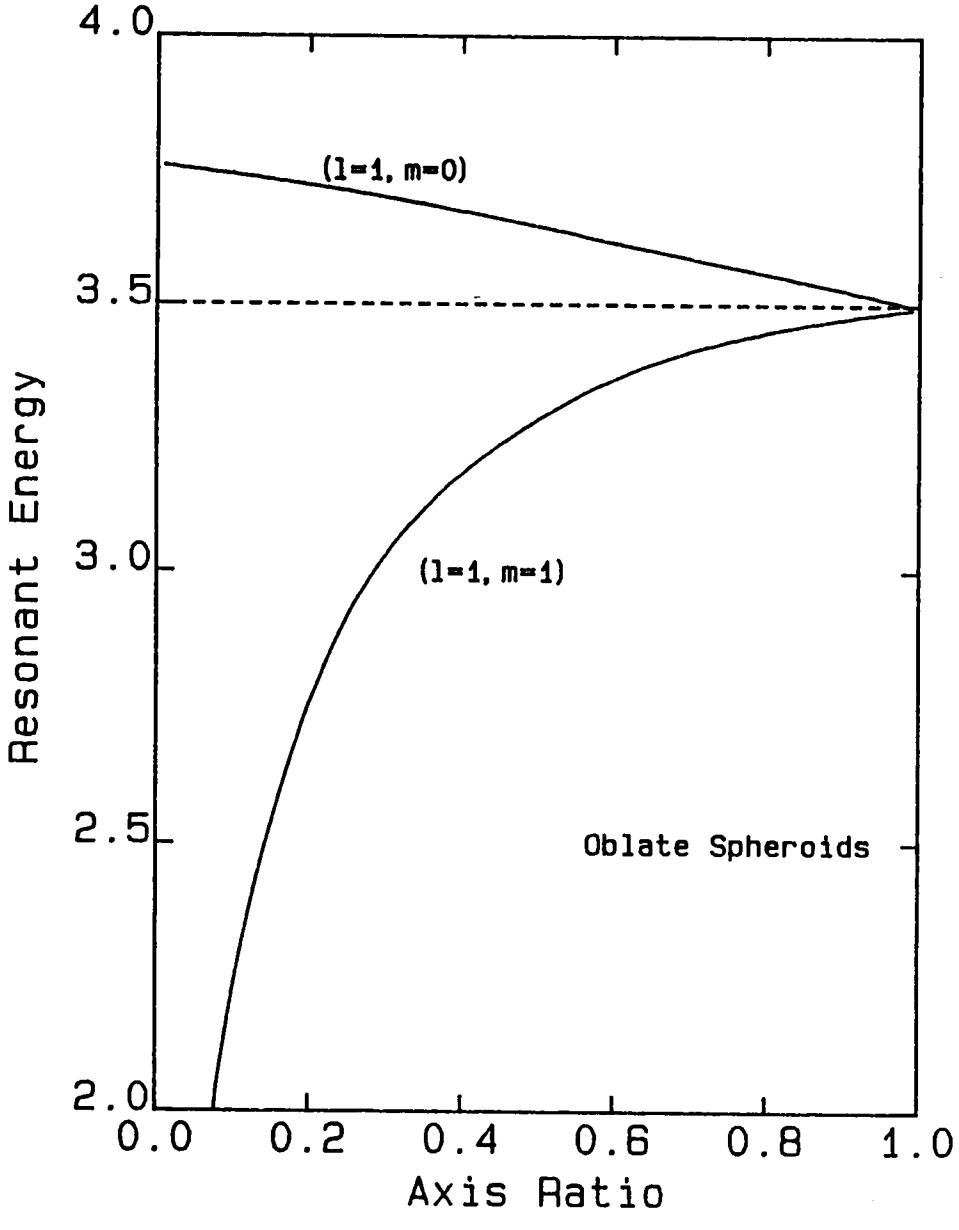



Figure 2-12. The calculated mode energies for the two dipole modes for oblate silver spheroids as a function of shape parameter.

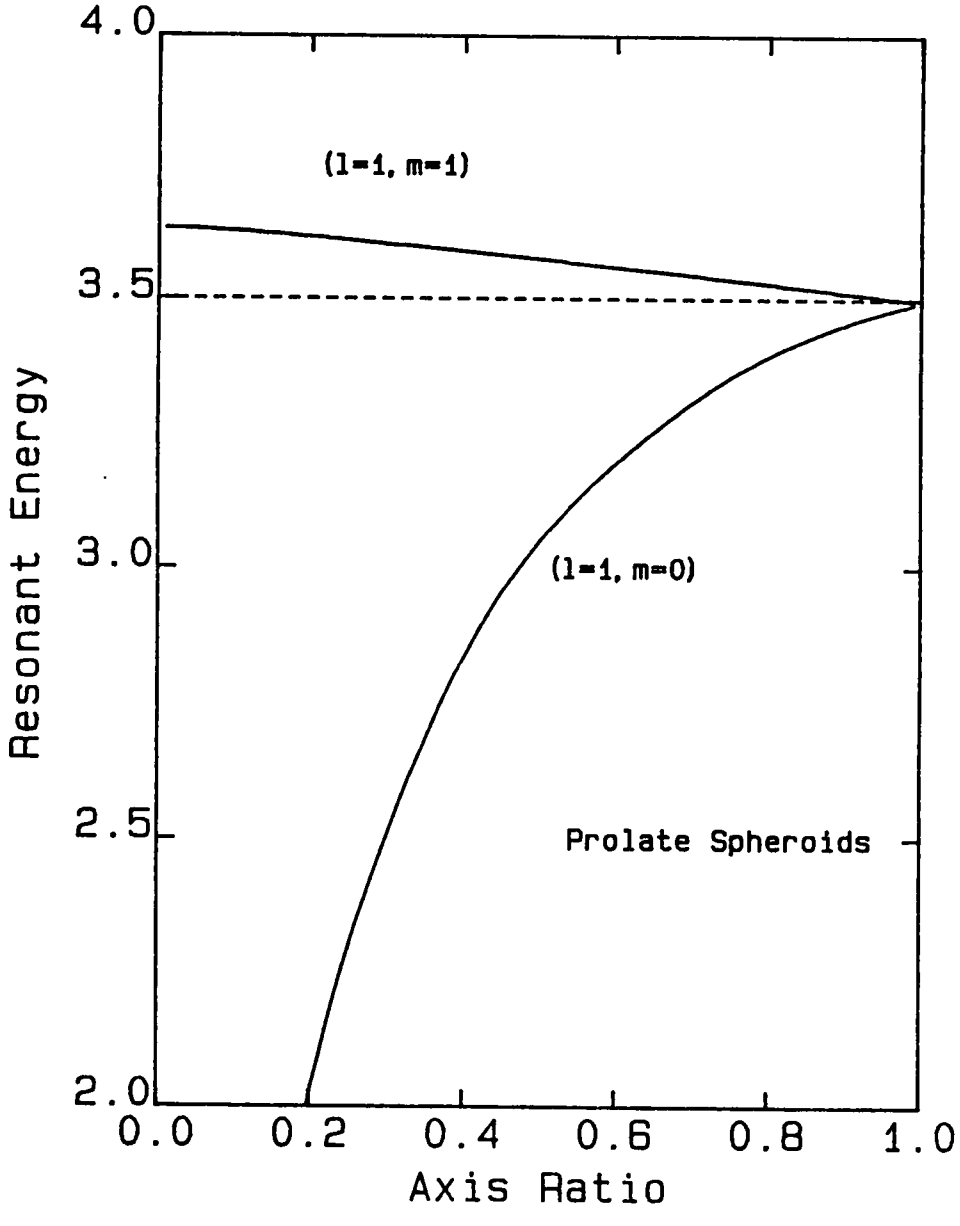



Figure 2-13. The calculated mode energies for the two dipole modes for prolate silver spheroids as a function of shape parameter.

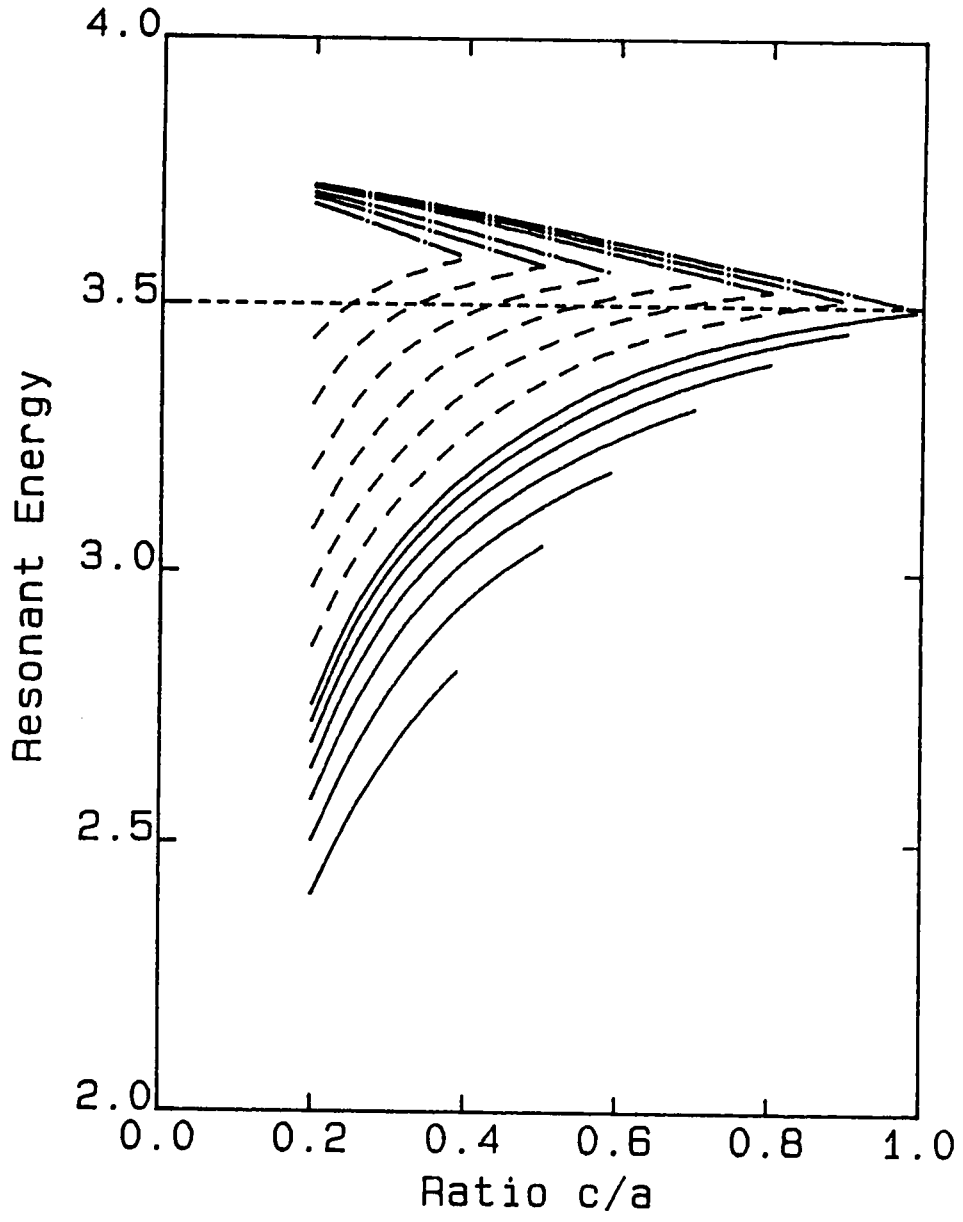



Figure 2-14. Dielectric response as a function of axis ratio c/a for values of ratio b/a for resonant charge-density-oscillation modes in silver ellipsoids. Oscillations along the a axis are the solid lines, oscillations along the b axis are the dashed lines, and oscillations along the c axis are the dash-dotted lines.

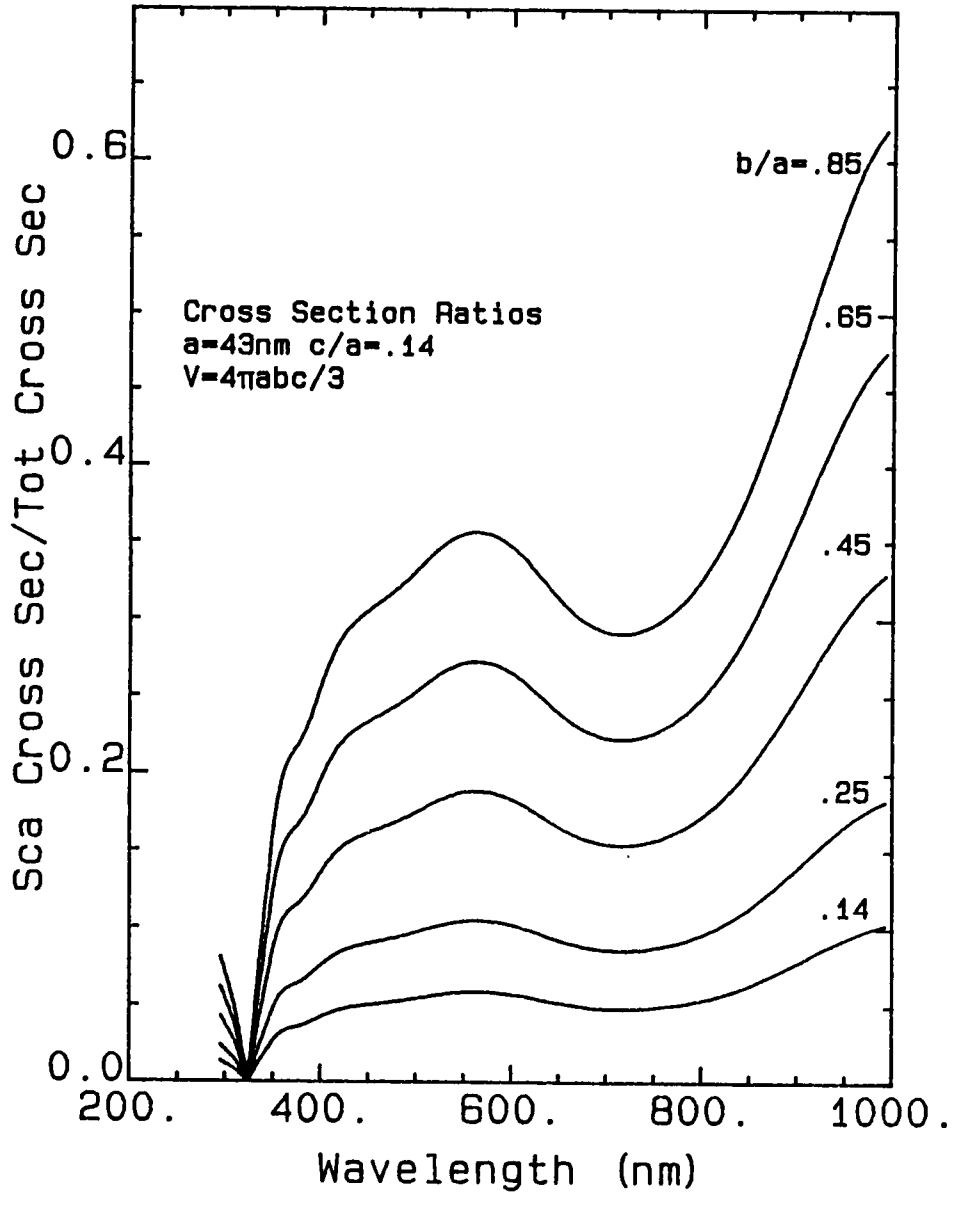



Figure 2-15. The ratio of scattering cross section to total cross section as a function of the wavelength for different shapes of ellipsoids. The volume equation is shown and the volume is not held constant for changes in shape.

## I. THE OPTICAL ABSORBANCE

The optical absorbance is defined as

$$A = \log_{10}\left(\frac{I_o}{I_t}\right) , \tag{2-177}$$

where $I_o$ is the incident intensity and $I_t$ is the transmitted intensity. Light incident on silver particles is transmitted scattered or absorbed by stimulating surface plasmons. So

$$I_o = I_s + I_t + I_a , \tag{2-178}$$

where $I_s$ , $I_t$ , and $I_a$ are the scattered, transmitted, and absorbed intensities respectively. By rearranging we get

$$\frac{I_o}{I_t} = \frac{1}{1 - (I_s/I_o - I_a/I_o)} . \tag{2-179}$$

The scattering and absorption cross sections are related to the respective intensities by

$$\frac{I_s}{I_o} = N\sigma_{sca} \tag{2-180}$$

and

$$\frac{I_a}{I_o} = N\sigma_{abs} . \tag{2-181}$$

Here N is the number of particles per unit area. Since the total cross section is the sum of the scattering and the absorption sections

$$\frac{I_o}{I_t} = \frac{1}{1 - N\sigma_{tot}} \tag{2-182}$$

or

$$A = \log_{10}\left(\frac{1}{1 - N\sigma_{tot}}\right) . \qquad (2\text{-}183)$$

# CHAPTER III

# EXPERIMENT

## A. INTRODUCTION

We describe a simple technique for producing arrays of small silver particles approximately ellipsoidal in shape. The ellipsoids were produced in a well-defined orientation so that each sample contained ellipsoids with parallel principal axes. Samples of this type were made by producing a patterned substrate and depositing silver onto the substrate. We have qualitatively characterized the resulting particles as to size, shape and interparticle spacing by scanning electron microscopy.

## B. SAMPLE PREPARATION

Silver ellipsoidal particles were formed by using microlithography to produce a large patterned area on a quartz substrate. We then deposited silver on the substrate to form silver ellipsoids. Figure 3-1 shows a general schematic for the production of silver ellipsoids.

Quartz microscope slides [3.1] were scribed and sectioned into 1 X 1 inch squares. The slides were thoroughly cleaned and placed in an electron beam evaporation system which was evacuated to $3 \times 10^{-7}$ Torr. $SiO_2$ was evaporated on the slides at a rate of 0.5 nm/sec to a thickness of 500 nm. The thickness and rate was measured by using a quartz crystal thickness monitor.

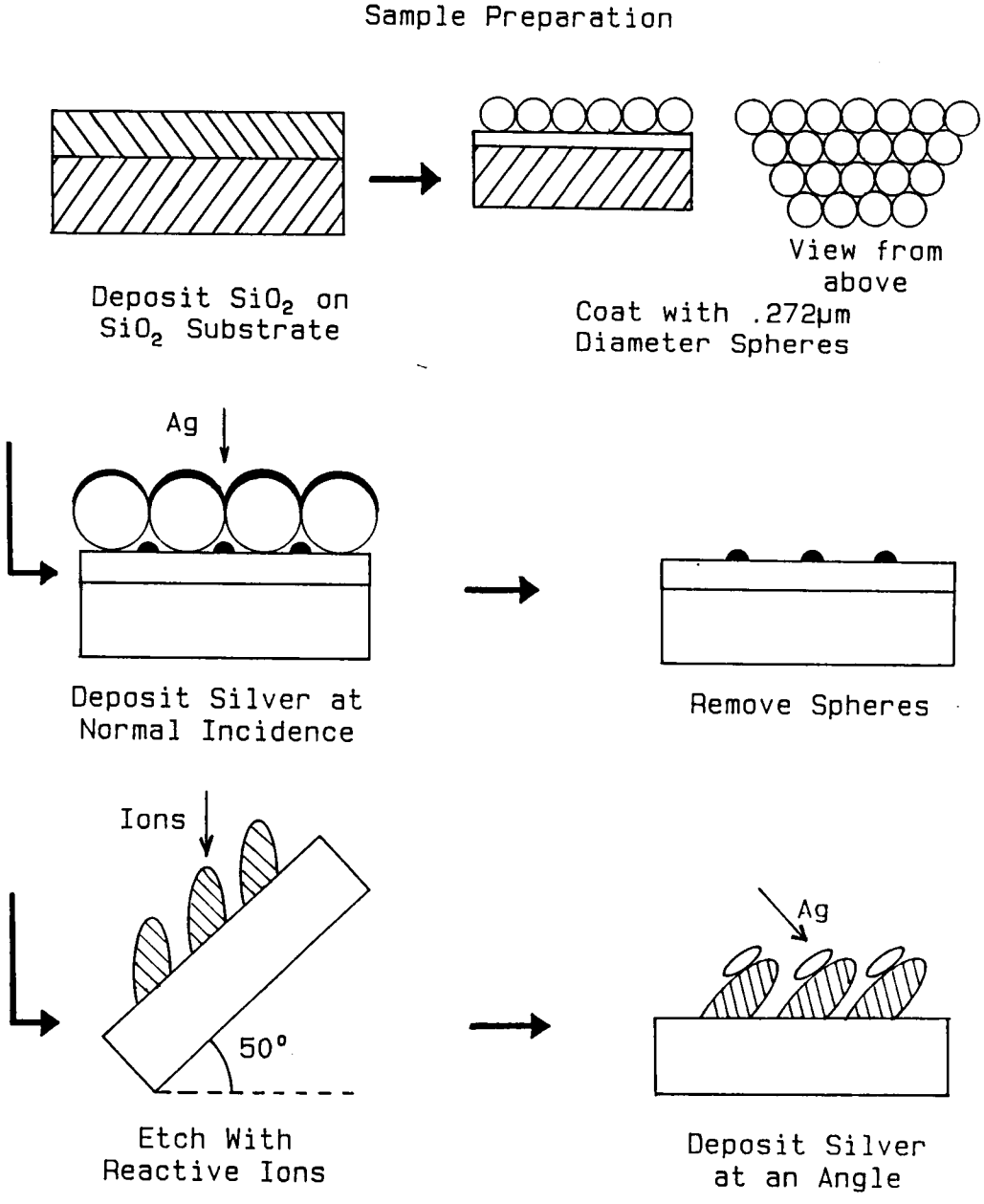



Figure 3-1. A general schematic for the production of silver ellipsoids. The patterned substrate allows the formation of ellipsoids with parallel principal axes.

The adhesion of the evaporated $SiO_2$ to the quartz slide was found to be sensitive to the cleanliness of the substrate and the pressure of the evaporation system. The slides were cleaned with a detergent [3.2] and rinsed in distilled water for 5 min. They were then placed in an ultrasonic cleaner in an acetone bath for 5 min and then in the ultrasonic cleaner in a methanol bath for 5 min. The slides were flooded with methanol directly from the original container and blown dry with nitrogen. They were placed immediately in the electron beam evaporator and it was evacuated. Quartz evaporated onto substrates that were not clean or evaporated at pressures higher than about $6 \times 10^{-6}$ Torr would separate from the substrate and flake off. The vacuum system for the e-beam evaporator is an oil free cryopumped system [3.3]. Quartz depositions made in this system were much more successful because of the lack of oil contamination and the high pumping speed of the cryopump.

Quartz was deposited onto the slides to provide a medium in which to reactive-ion etch the patterned structures. Because of its crystal structure, the deposited quartz layer etches under reactive-ion etching approximately ten times faster than the fused quartz of the original slide. However, it has almost identical optical properties for light in the 300-800 nm wavelength range.

These coated slides were then covered by a densely packed monolayer of 272 nm diameter polystyrene spheres [3.4]. This was accomplished by spin coating the slides with a mixture of the

polystyrene spheres and distilled,deionized water. The standard mixture from the manufacturer was diluted from 10% solids to 3.3% solids. The slides were flooded with the mixture using a microliter pipette and spun at 1000 rpm in a standard spin coater until dry (approximately 40 sec). Figures 3-2 and 3-3 are electron micrographs of a monolayer of spheres. The spheres are ordered in close packed arrays ranging from a few spheres to several thousand. The arrays are separated by grain boundaries and include point defects and dislocations.

The slides were returned to the electron beam evaporator and coated with a layer of silver 40 nm thick and at a rate of 5 nm/sec. The densely packed arrays of spheres act as a deposition mask for the silver coating [3.5] so that the quartz substrate is coated with silver only at openings between spheres.

The spheres were removed from the substrate by ultrasonic cleaning in methylene chloride. This leaves small triangular patches of silver from the sphere openings in ordered arrays on the quartz. The residual methylene chloride was removed by ultrasonic cleaning in methanol. The silver patches were used as an etch mask in anisotropic reactive-ion etching to produce quartz posts on the substrate. Figure 3-4 shows the deposited silver particles on a quartz substrate.

The etching system is a standard 13.5 MHz rf sputter-etch system [3.6] with planar parallel cathodes that may be dc biased to drive ions toward either cathode. The bias voltage may be varied from zero up to

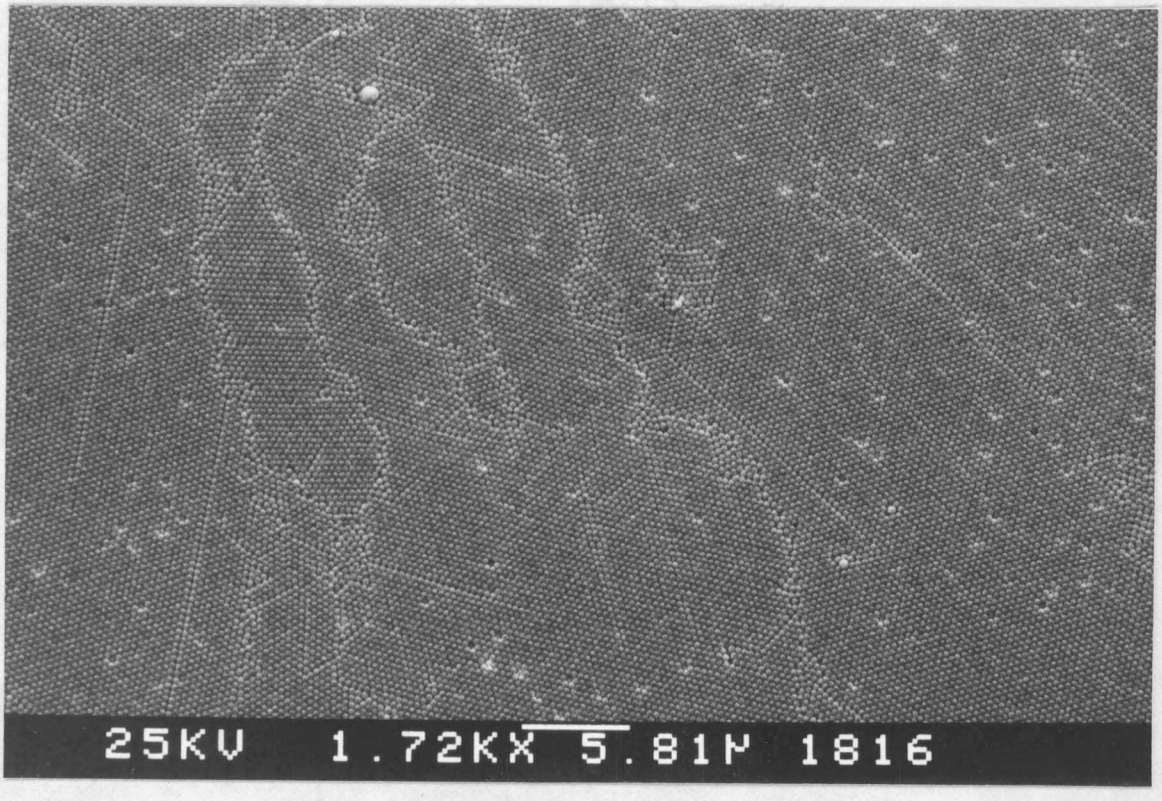



Figure 3-2. A monolayer of 272-nm-diameter polystyrene spheres on a substrate. The substrate was flooded with a 3.3% solids mixture of spheres and water and spun at 1000 rpm until dry. A grain boundary and dislocations are visible. The bar indicates a length of 5.18 $\mu$m.

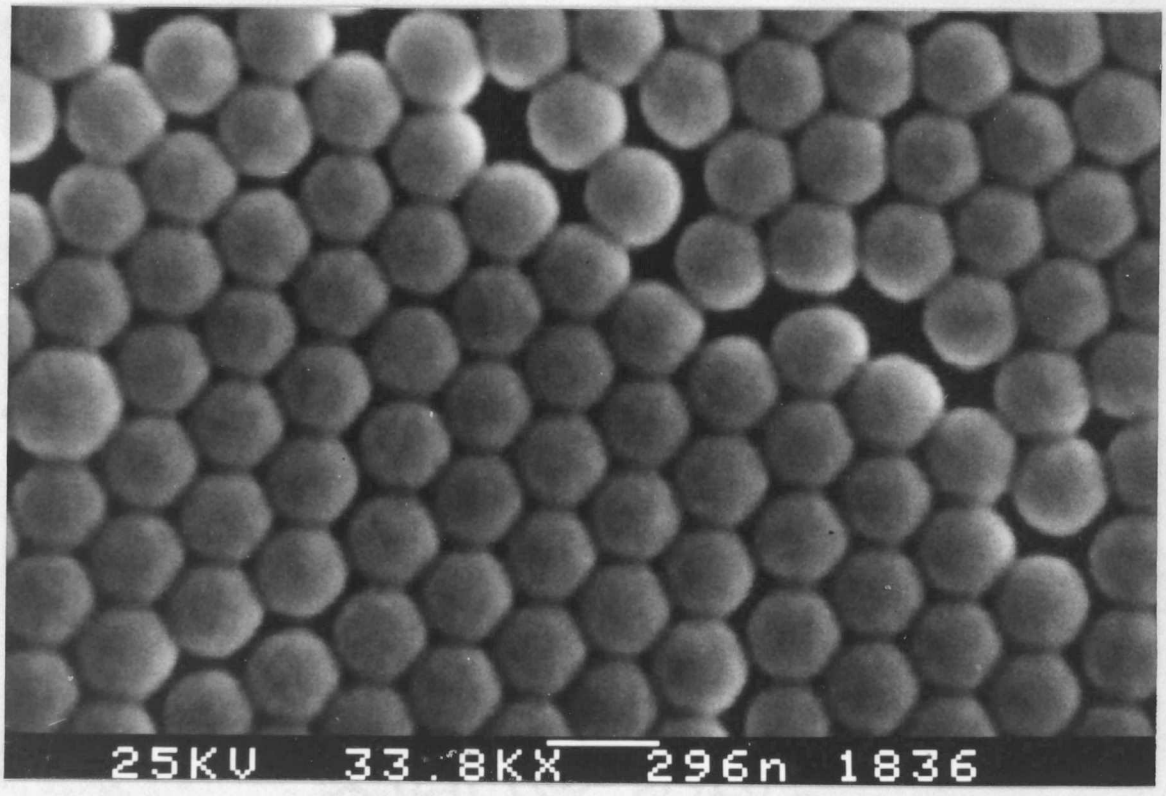



Figure 3-3. A monolayer of 272-nm-diameter polystyrene spheres on a substrate. The substrate was flooded with a 3.3% solids mixture of spheres and water and spun at 1000 rpm until dry. A grain boundary and dislocations are visible. The bar indicates a length of 296 nm.

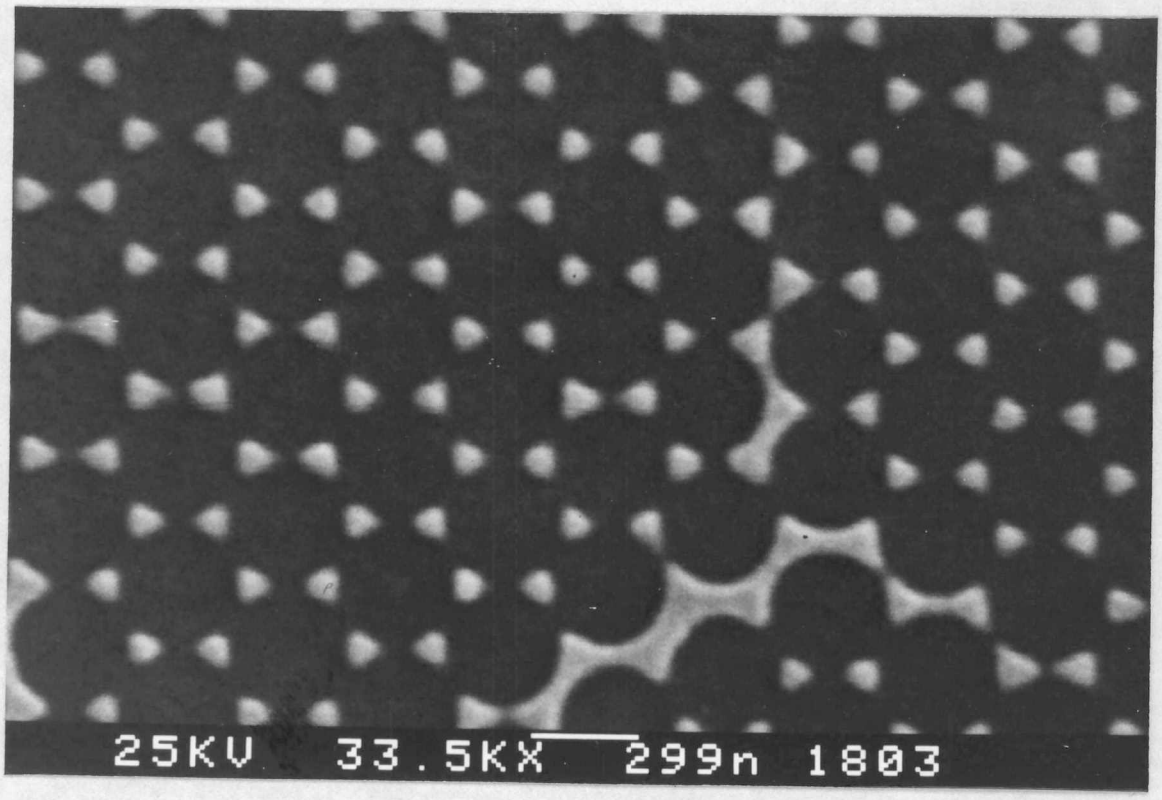



Figure 3-4. A silver-particle array fabricated by depositing silver over a densely packed array of 272-nm-diameter spheres. The spheres were dissolved by ultrasonic cleaning in methylene chloride. The bar indicates a length of 299 nm.

700 volts. The etch system is evacuated by an oil based diffusion pump with an $LN_2$ trap and backed by a direct drive mechanical roughing pump. Base pressures of $10^{-5}$ Torr are obtainable with this system.

In this case the etching system was biased to drive reactive ions toward the bottom cathode where the sample was placed. The sample was thus subjected to anisotropic etching along the sample normal. By etching with $CHF_3$ and using the ordered arrays of silver particles to mask the substrate directly under each particle, ordered arrays of posts were produced.

The etch procedure is initiated by roughing the system to 35$\mu$m and back-filling with $CHF_3$ several times. The system is then pumped to $1 \times 10^{-5}$ Torr. Using a needle valve the pressure is raised to 2$\mu$m with $CHF_3$ and the etch is begun. We have emperically determined that etching with an input power of 50 W and a bias voltage of 300 V for 30-32 min produces posts that are approximately 200 nm tall and somewhat less than 70 nm in diameter. We found that the etch rate slowed by a factor of two to three if the diffusion pump was throttled to achieve the etch pressure. The fastest rate consistently occured if the pump was left open and the 2$\mu$m etch pressure was reached by admitting $CHF_3$ to the system.

Placing the quartz substrate at a 50° angle with respect to the bottom cathode produces posts that lean at about a 40° angle with respect to the substrate normal. This technique produces a large patterned array of oriented posts. Figure 3-5 is an electron

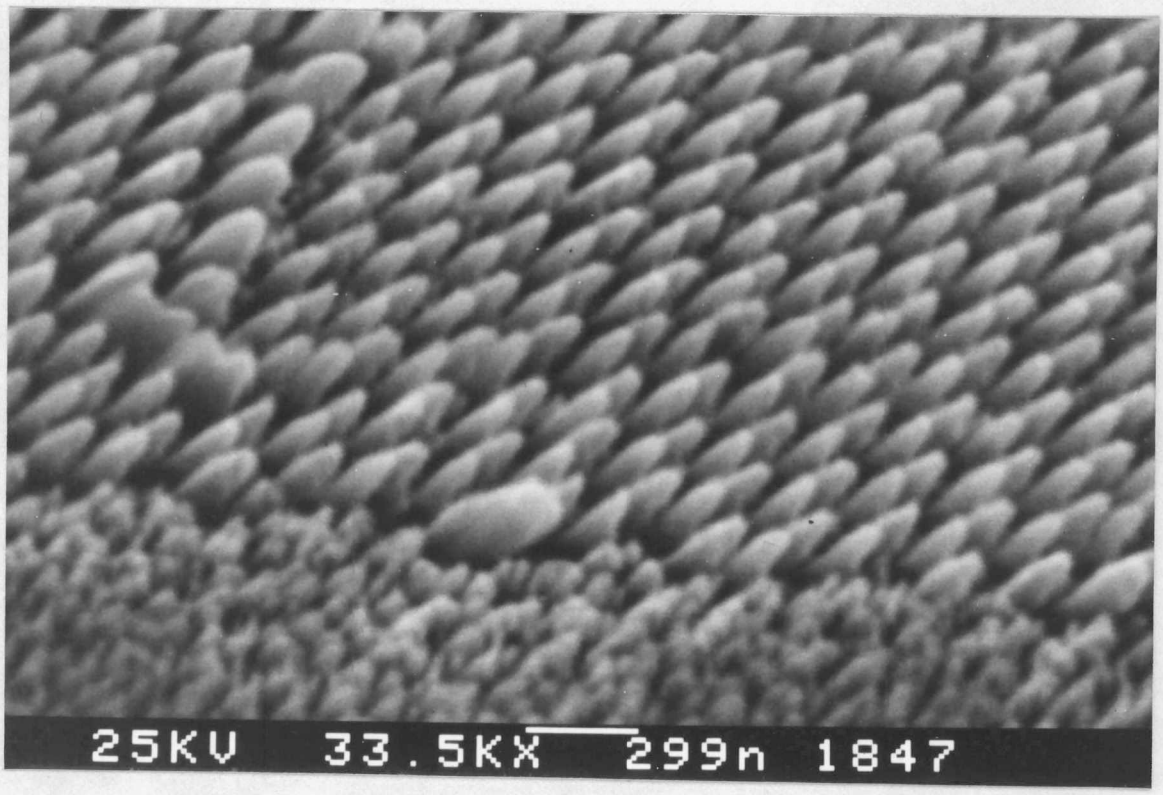



Figure 3-5. $SiO_2$ posts fabricated by reactive-ion etching in $CHF_3$. The posts have short range order and lean at ~40° with respect to the substrate normal. Silver is deposited at near normal to the post axes (e.g., from the left here) to produce silver ellipsoids. This view is at 50° with respect to the substrate normal. The bar indicates a length of 299 nm.

micrograph of a set of etched posts. Silver deposited obliquely produces elongated particles with parallel principal axes.

Silver ellipsoids were formed on the sides of the posts by using an evaporation direction in the plane containing the sample normal and the post axes. The angle was chosen so that silver would be deposited at near normal incidence to the side of the posts. The use of these inclined posts resulted in more uniformly shaped particles than samples that were etched normally. The shadowing of the posts by one another helped to prevent silver from being deposited on areas of the substrate between posts. The angle of the substrate could be varied to produce particles with different axis ratios. Figure 3-6 shows silver deposited on a set of posts at 35° with respect to the sample normal. The silver thickness was measured with the crystal thickness monitor oriented so silver was deposited along the crystal normal. The post sides were nearly parallel to the crystal surface so that about the same depth of silver was deposited on the post sides as was indicated by the thickness monitor. The direction of deposition is from the left in this micrograph and the view is at 50° with respect to the sample normal. The post structures are very durable. They can be chemically cleaned and reused for subsequent silver depositions without damage to the posts.

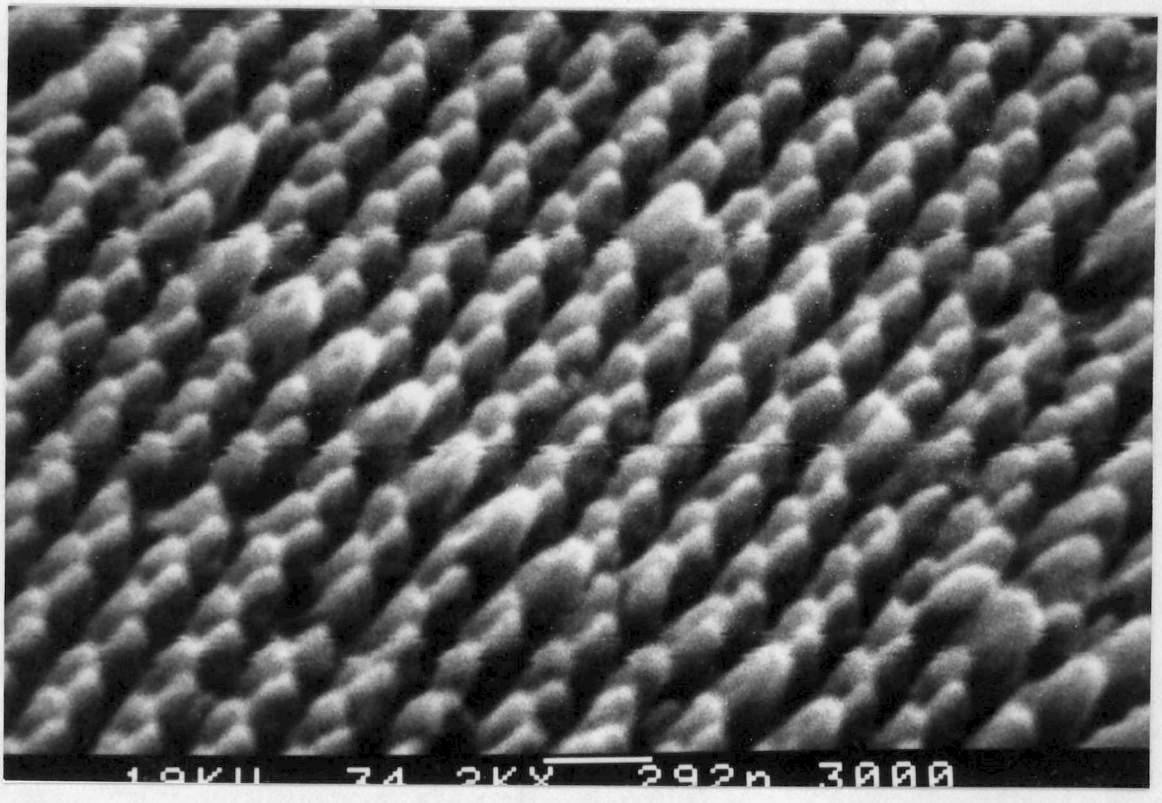



Figure 3-6. Silver deposited on a set of posts at 35° with respect to the sample normal. This view is at 50° with respect to the sample normal. The bar indicates a length of 292 nm.

## C. APPARATUS

The absorbance data were taken with a Shimadzu UV-250 recording spectrophotometer [3.7]. The UV-250 is a double monochromator with a concave holographic and a planar holographic grating. It has a halogen and a deuterium light source and is capable of measuring both absorbance and transmittance over a wavelength range of 190 to 900 nm. Figure 3-7 is a schematic of the components of the spectrophotometer. The UV-250 sample chamber contains a sample and a reference cell. The incoming light is chopped, alternately passing through each cell. The chopping frequency is 60 Hz. The light from each cell is detected by a single photomultiplier tube. The reference signal is used as part of a feedback loop to control the detector gain so that the reference signal is maintained at a constant level. Thus the sample signal is proportional to the sample transmittance. The signal is read through an analogue to digital converter by a microprocessor which makes a baseline correction, performs a smoothing computation and makes a logarithmic conversion. The spectrum curves can be output in graphic form or the data printed out. The UV-250 also has an IEEE interface which allows direct communication with a PDP 11/02 microcomputer. The 11/02 can control the UV-250 to collect data and transfer the data directly to a floppy disk for analysis.

For all the data taken, a set of quartz posts without any deposited silver was used in the reference cell. So the measured absorbance is proportional to the ratio of the intensity of the light

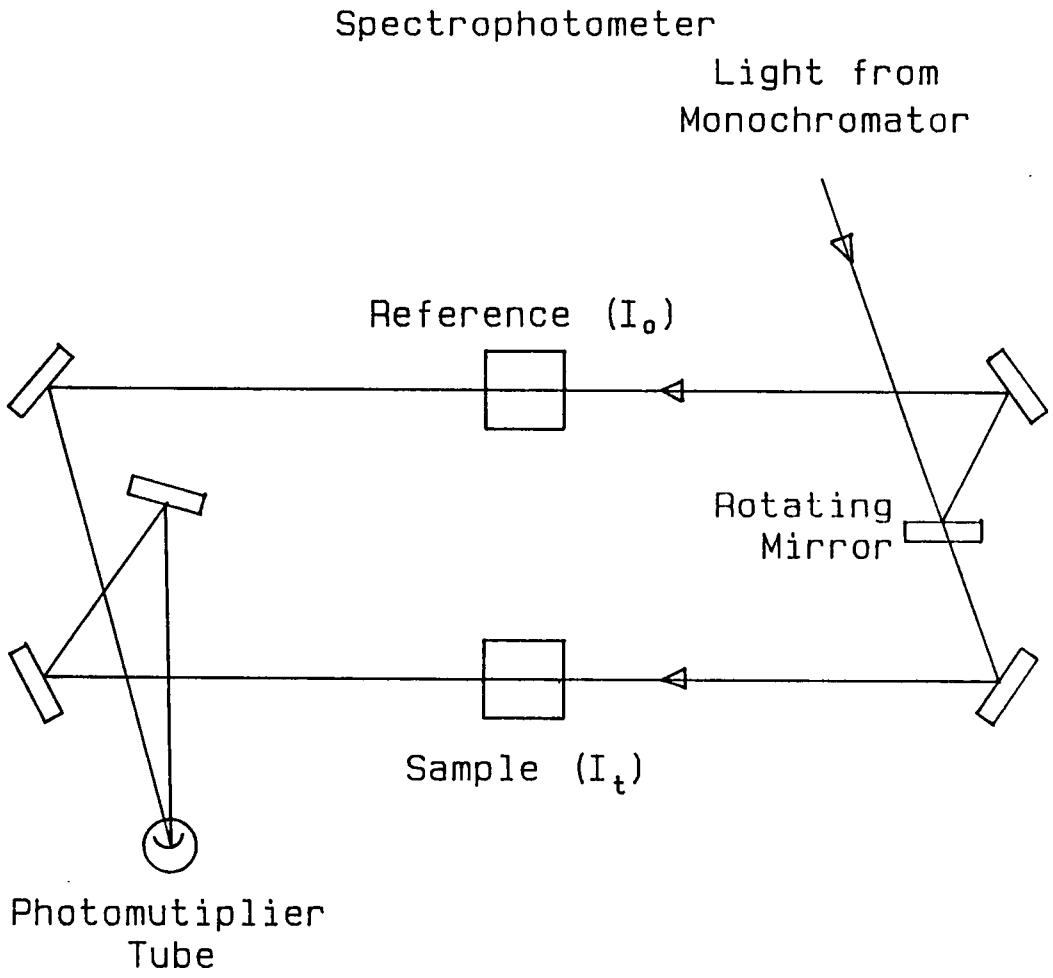



Figure 3-7. A schematic of the components of the spectrophotometer. The sample chamber contains a sample and a reference cell and the light from each cell is detected by a single photomultiplier.

passing through the posts with no silver to the intensity of the light passing through the sample. Since there is a reflectivity difference between a quartz-air interface and a quartz-silver interface, simply using a set of posts with no silver may not be an adequate reference. Absorbance from posts without silver was measured and found to contribute no structure to the absorbance curves. Because the reflection and absorption due to quartz posts is relatively small and without structure, the calculated and experimental absorbance would be expected to differ only slightly in height but would have identical structure. Therefore a set of quartz posts without silver is an adequate reference.

Angular dependence of the absorbance is a primary goal of this experiment. In order to vary the angle of incidence of the light, sample mounts were constructed to rotate both sample and reference slides. The final design utilizes Newport Corporation's mini series rotary stages [3.8] and an aluminum slide holder mounted on the rotary stage. The stages allow the angle of incidence to be set to within $\pm 1$ degree.

Because the light beam is focused from the last mirror to a point in the sample chamber, there is an angular spread in the incident light. This total spread is less than five degrees and since we are interested in a more general angular dependence this effect may be neglected.

To measure absorbance as a function of the polarization of incident light, two Polaroid UV polarizers were mounted in front of the sample and reference cells of the sample chamber. This allows light to be polarized along principal axes of the particles. We use the standard convention for labeling polarization states. P-polarized light is polarized in the plane defined by the incident wave vector and the substrate normal. S-polarized light is polarized perpendicular to this plane.

## D. DATA-TAKING PROCEDURE

Samples were prepared for data acquisition cleaning and depositing fresh silver. The first step in sample preparation was to dip a set of posts in dilute nitric acid (10% by volume) for about 15 sec. This would remove any silver left over from the etch mask for a new sample or remove any deposite dsilver particles if the sample had been previously used. The posts were then cleaned in an ultrasonic cleaner with an acetone bath for 5 min and a methanol bath for 5 min. The posts were flooded with methanol from the original container and blown dry with nitrogen. The cleaned sample was placed at the desired angle of silver deposition in the e-beam evaporator and it was evacuated to $1 \times 10^{-6}$ Torr. The silver was deposited at 1 to 2 nm/sec up to the desired depth. We found that slow deposition rates (<0.5 nm/sec) produced particles that were ellipsoidal or spheroidal in nature but closer to a spherical shape than those produced by depositing silver

more rapidly. We believe that this is due to the small contact area between the post and the deposited silver. At slower evaporation rates the silver has more time for its surface tension to form a more spherical shape.

Once the silver deposition was complete the optical measurements were begun within a few minutes and all measurements were completed usually within an hour. This short period of time helped to minimize the effects due to contamination by air.

To take data a baseline was run on the UV-250 with the polarizers in place just prior to each measurement. The UV-250 automatically makes a baseline correction before it displays the absorbance data. Each change in polarization requires a new baseline to be established before measurements can be made. The data were transferred to a PDP 11/02 via an IEEE interface and a program written by R.J. Warmack. The data could then be stored on a floppy disk and displayed directly using a graphics terminal and a PDP 11/23.

# CHAPTER IV

# EXPERIMENTAL RESULTS AND COMPARISON WITH THEORY

## A. INTRODUCTION

In Chapter II it was shown that the optical absorbance is related to the total electrodynamic cross section. This cross section is a function of the incident angle, wavelength, and polarization of the incoming light. For silver ellipsoidal and spheroidal particles the dependence of the cross section on these parameters is determined by the shape and the bulk optical properties of silver. Figure 4-1 shows the experimental parameters. The angles are measured relative to the Cartesian coordinate axes shown in the same manner as in spherical coordinates. The experimental results are displayed as graphs of absorbance as a function of the wavelength of the incident light and compared with theoretical calculations of absorbance.

## B. RESULTS AND COMPARISONS

The data shown in all figures was taken using a sample with leaning posts and with 15 nm of evaporated silver at 35° with respect to the sample normal. Study of scanning electron micrographs revealed that these silver deposition parameters produced particles with an average a- and b- semiprincipal axis lengths of about 60 nm and 35 nm respectively. The c-semiaxis is approximately parallel to the direction of evaporation. This makes the dimension of the particle

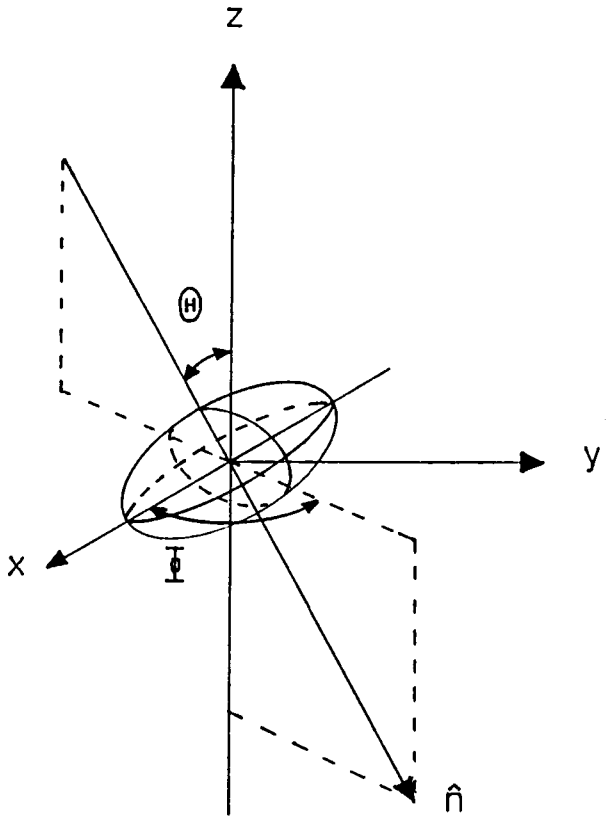



Figure 4-1. Experimental parameters. The angles Θ and Φ are measured relative to the z- and x-axes and x is along the post axis.

along the c-axis approximately equal to the silver thickness. Therefore, the c-semiaxis length is roughly half the evaporation depth.

Figure 4-2 is the optical absorbance for p-polarized light as a function of the wavelength at $\Phi$=0°, $\theta$=0° (i.e. polarized along the a-axis). The measured absorbance is the dotted line and the calculated absorbance is the solid line. There is a shoulder at 460 nm in the experimental absorbance that is not predicted by the theory. Figure 4-3 is s-polarized data for the same angles. The measured absorbance here has a strong peak at 520 nm that is not predicted by the theory. This additional structure in the absorbance curves is believed to be due to the formation of a second type of particle that has a different shape and is oriented differently with respect to the post axes. This second type of particle is a small percentage of the total; most of which are the type previously described. While both particles are ellipsoid like in shape, the type 1 particle is nearly prolate with the b- and c-axes similar in length but shorter than the a-axis. The type 2 particle has oblate characteristics with the a- and b-axes similar in length but longer than the c-axis. The a-axis of the type 1 particles are oriented parallel to the post axes and the a-axis of the type 2 particles are oriented perpendicular to the post axes.

The type 2 particle is produced as a result of the packing arrangement of the spheres used in making the etch mask. Because the polystyrene spheres from close packed arrays, the silver patches that form the mask are arranged hexagonally about each sphere. In this

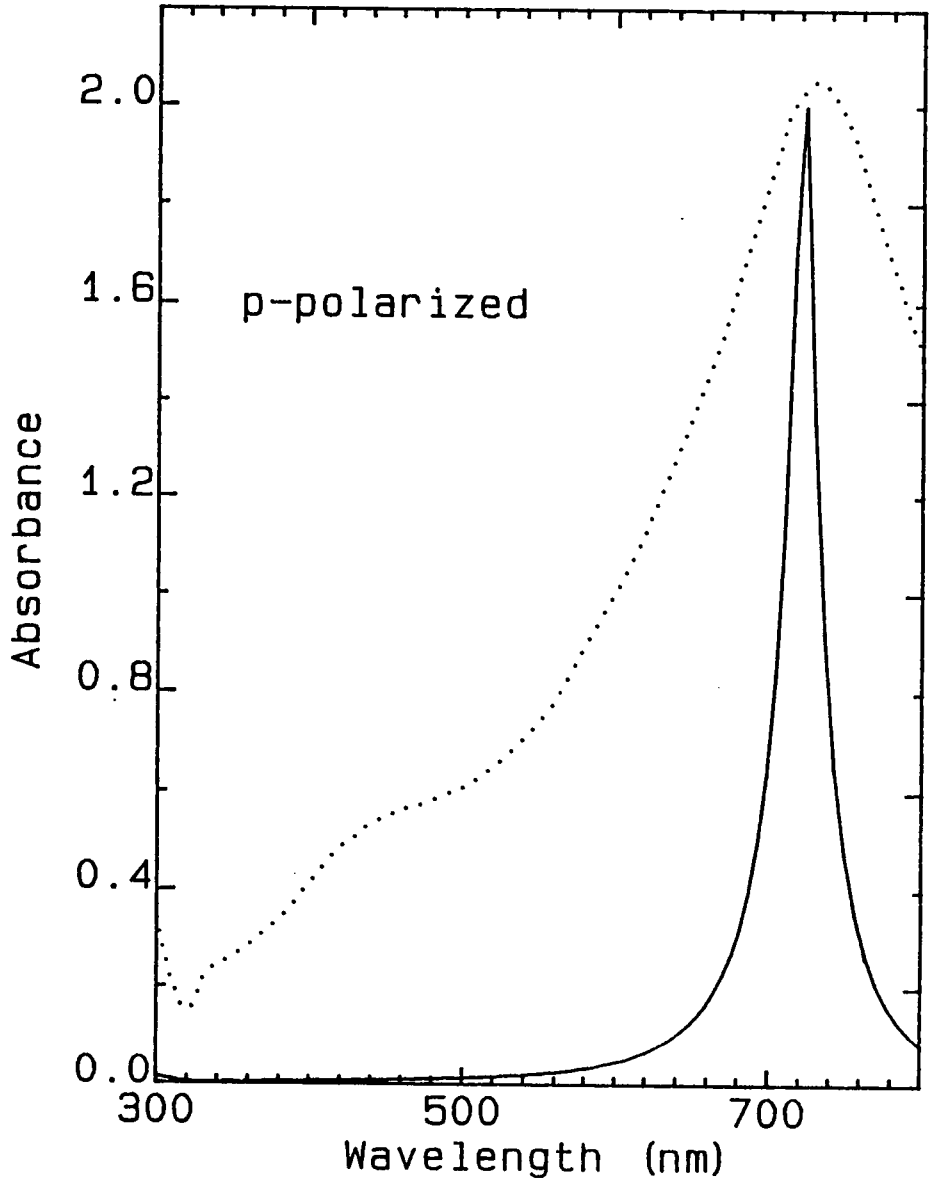



Figure 4-2. Comparison of experimental and theoretical absorbance for p-polarized light for a single ellipsoid. The solid curve represents the calculations and the dotted curve represents the data for 15 nm of silver deposited at 35° with respect to the sample normal. The angles of incidence are $\Phi$=0° and $\theta$=0°.

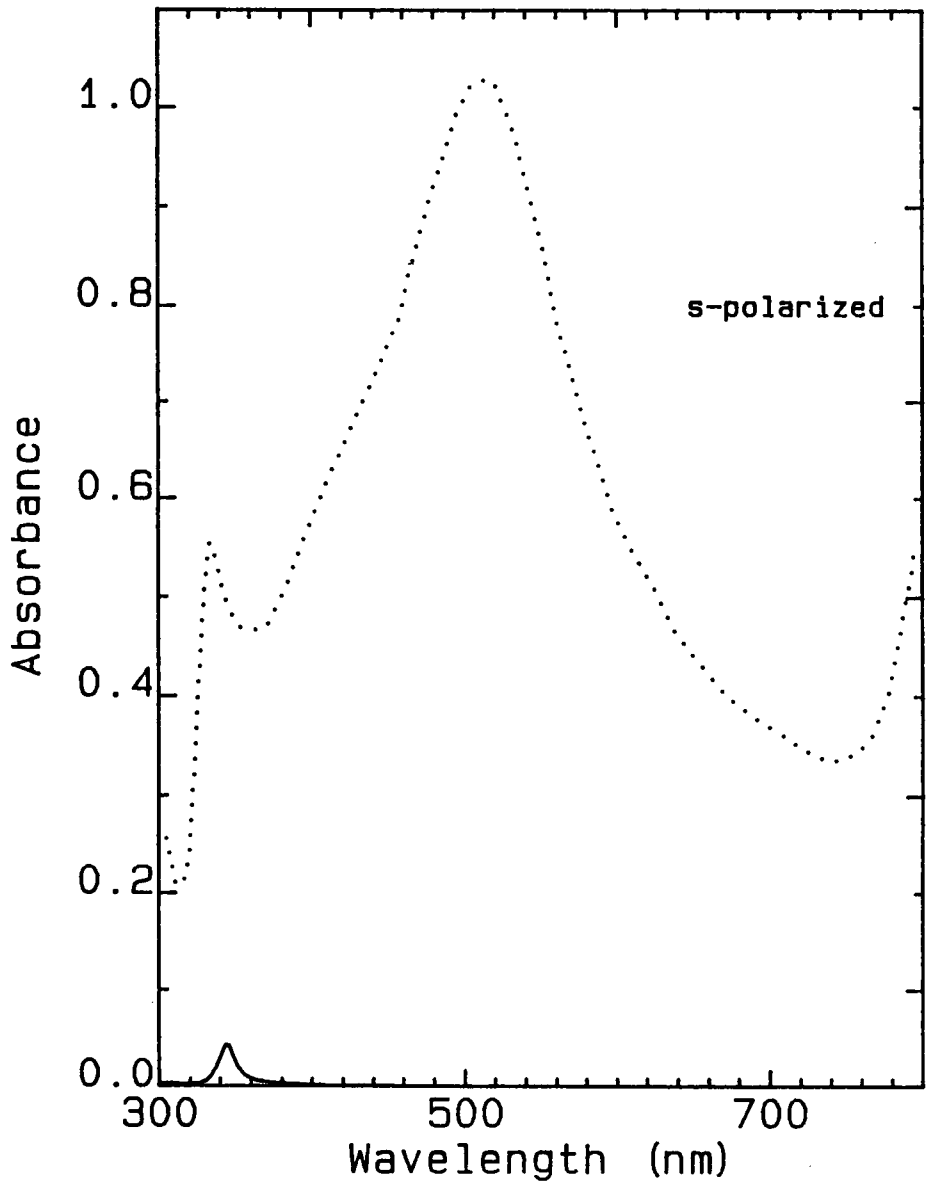



Figure 4-3. Comparison of experimental and theoretical absorbance for s-polarized light for a single ellipsoid. The solid curve represents the calculations and the dotted curve represents the data for 15 nm of silver deposited at 35° with respect to the sample normal. The angles of incidence are $\Phi$=0° and $\theta$=0°.

configuration each patch has three nearest neighbors that are within a few tens of nanometers (see Fig. 3-3). The posts formed in this way can occasionally produce silver particles that bridge these adjacent posts. Also, because there are grain boundaries and dislocations the sphere arrays are not always perfectly close packed. When this occurs the silver particles that form the mask can be within a few nanometers of each other or even be formed connected together. This in turn yields posts that are separated by only a few nanometers, are joined together along the lower part of their lengths separated only near the top, or are formed as a single structure. Scanning electron micrographs show that about 14% of the structures are formed from two posts joined together. About 5% of the structures are formed from more than two posts. Deposited silver on these structures can form the type 2 particle and silver deposited on the posts not fully separated or very close together can bridge between them forming a single particle supported by both posts. Figure 4-4 illustrates the conditions under which this might occur.

By adding a second particle to the calculated absorbance that is an ellipsoid in shape but with its longest axis perpendicular to the post axis, we can predict all of the peaks that appear in the optical absorbance. We have used a simple superposition of absorbance from the two particles to predict the peak positions. Figure 4-5 is the optical absorbance as a function of wavelength for p-polarization for the the same angles of incidence as in Figure 4-2 but assuming two kinds of

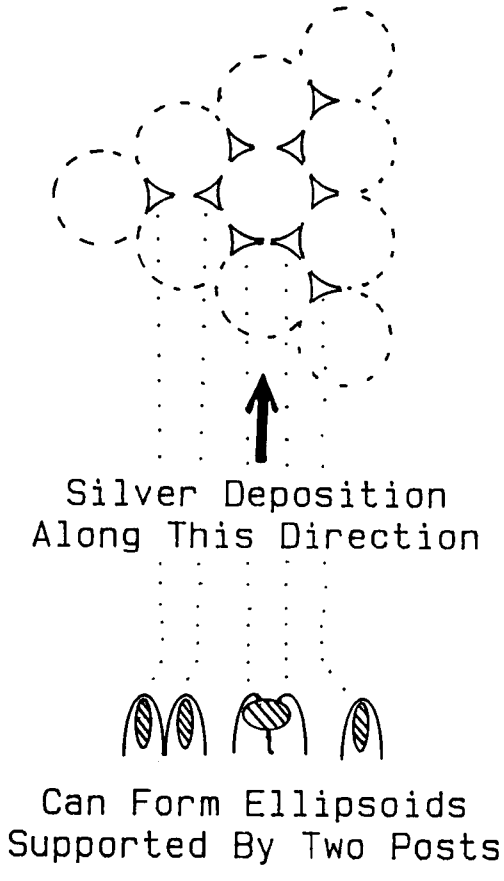



Figure 4-4. Conditions under which silver bridges form across the small gap between close lying posts to form a single ellipsoid.

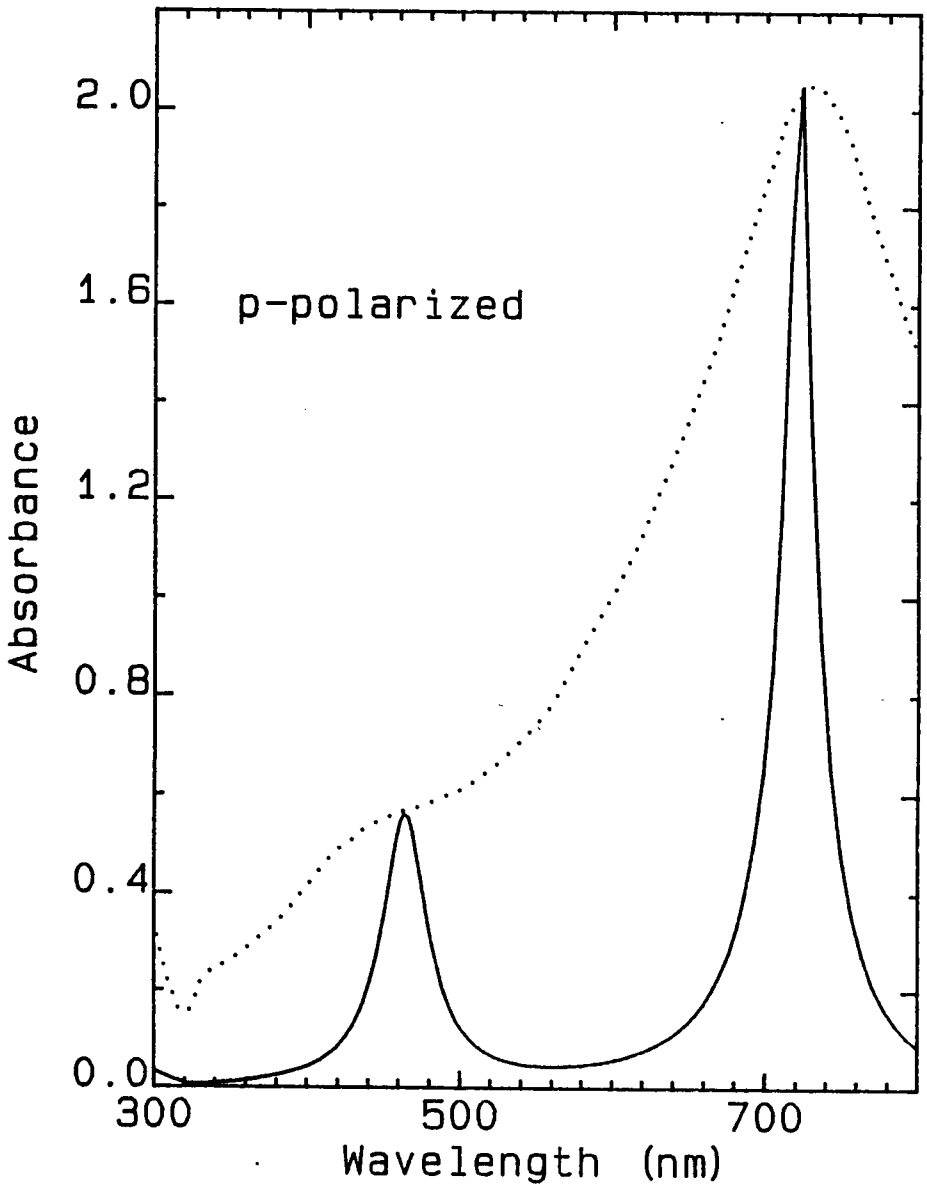



Figure 4-5. Comparison of measured and calculated absorbance for p-polarized light for two ellipsoids. The solid curve represents the calculations using two ellipsoids with the longest principal axes perpendicular to each other. The dotted curve represents experimental data with the same parameters as those used in Figure 4-2.

particles for the calculated absorbance. Figure 4-6 is s-polarization at the same angles for the two particle model. The fitting parameters used are semiprincipal axis length a=60 nm with axis ratios b/a=0.165 and c/a=0.145 for particle type 1 and a=35 nm with axis ratios b/a=0.84 and c/a=0.14 for particle type 2.

Scanning electron micrographs show that some of the nearby posts have silver particles bridged together to form a single particle. From the micrographs, the total number of type 2 particles ranged from 17.5 % up to 22 % on various parts of the sample. This is in reasonably good agreement with the calculated prediction of 22 %. The additional number of type 2 particles is due to silver bridging on close lying posts.

Because the posts are in ordered arrays separated by grain boundaries, the domains defined in this way are azimuthally oriented in a random fashion with respect to each other and to the direction of evaporation. This results in post shadowing during the evaporation process that varies from one array domain to another and so there is a distribution of a- and b-axis lengths. We have chosen to use a Gaussian distribution of shapes centered about the single shape that most closely matches the absorbance peaks.

Figure 4-7 is absorbance as a function of wavelength for s-polarized light with incident angles $\Phi$=0° and $\Theta$=0°. Recall that the angles are measured relative to the z-axis and the x-axis as in spherical coordinates. For type 1 particles the axes (a,b,c) are

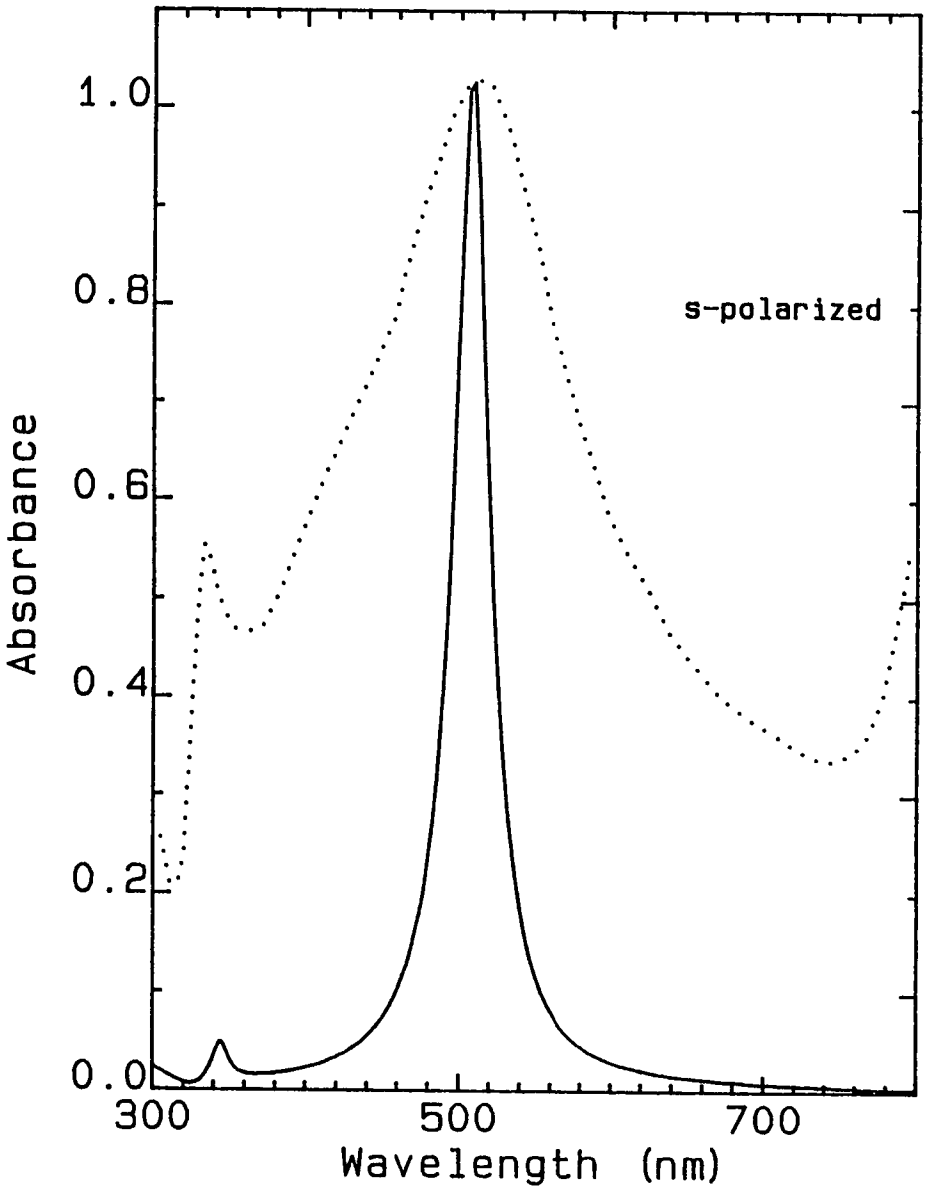



Figure 4-6. Comparison of measured and calculated absorbance for s-polarized light for two ellipsoids. The solid curve represents the calculations using two ellipsoids with the longest principal axes perpendicular to each other. The dotted curve represents experimental data with the same parameters as those used in Figure 4-2.

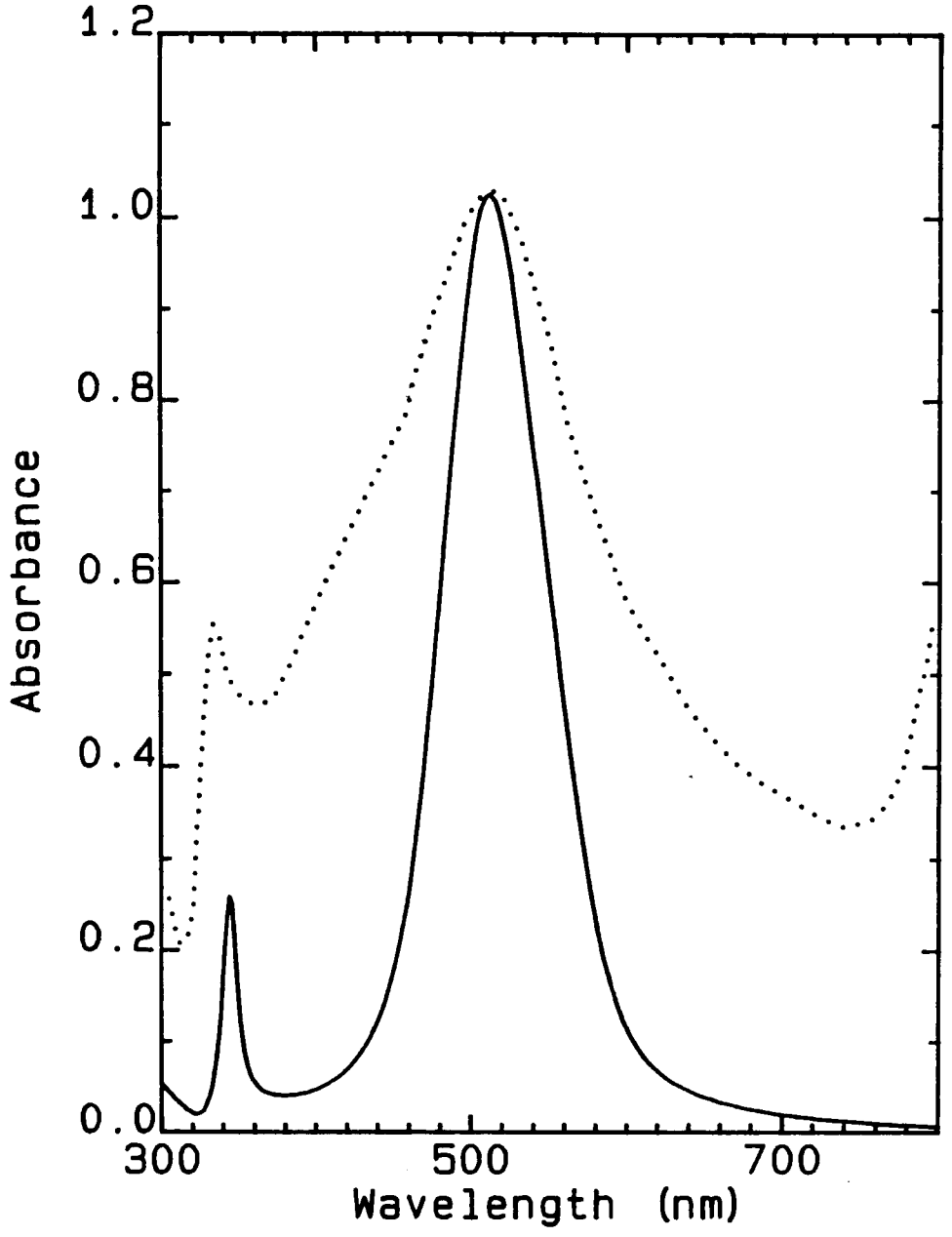



Figure 4-7. Comparison of experimental and theoretical absorbance for s-polarized light at $\Phi$=0°, $\Theta$=0°. The solid curve is theoretical absorbance using two ellipsoids whose longest principal axes are perpendicular to one another. A Gaussian shape distribution has been included. The dotted curve is experimental data for 15 nm of silver deposited at 35° to the sample normal.

parallel to (x,y,z) respectively while for type 2 particles the axes (b,a,c) are parallel to (x,y,z) respectively. This choice of coordinate axes makes the post axis parallel to the x-axis. The calculated curves were generated by choosing shape and size parameters which gave the best fit to the experimental data. The fitting parameters used are semiprincipal axis length a=60 nm with axis ratios b/a=0.165 and c/a=0.145 for particle type 1 and a=35 nm with axis ratios b/a=0.84 and c/a=0.14 for particle type 2. Axis lengths were broadened by Gaussian distribution widths 2.5 nm and 1.3 nm for particle type 1 and 2 respectively. Figure 4-8 and Figure 4-9 are absorbance as a function of wavelength for s-polarization for $\Phi$=0° and $\theta$=45° and 90° respectively Figures 4-10,4-11, and 4-12 are absorbance as a function wavelength for p-polarized light for the same angles and calculational parameters. Here slightly smaller distribution widths were used.

For s-polarized light the data shows two absorbance peaks for which the heights vary only slightly with changing angle. The additional structure beyond 700 nm is the result of the failure of the polarizers at those wavelengths. The peak at 340 nm is due to a charge-density oscillation along the b-axis of the type 1 particles and the peak at 500 nm is due to charge-density oscillation along the a-axis of the type 2 particles.

The p-polarized data shows absorbance peaks with heights that vary as a function of incident angle. At normal incidence ($\theta$=0°) there is

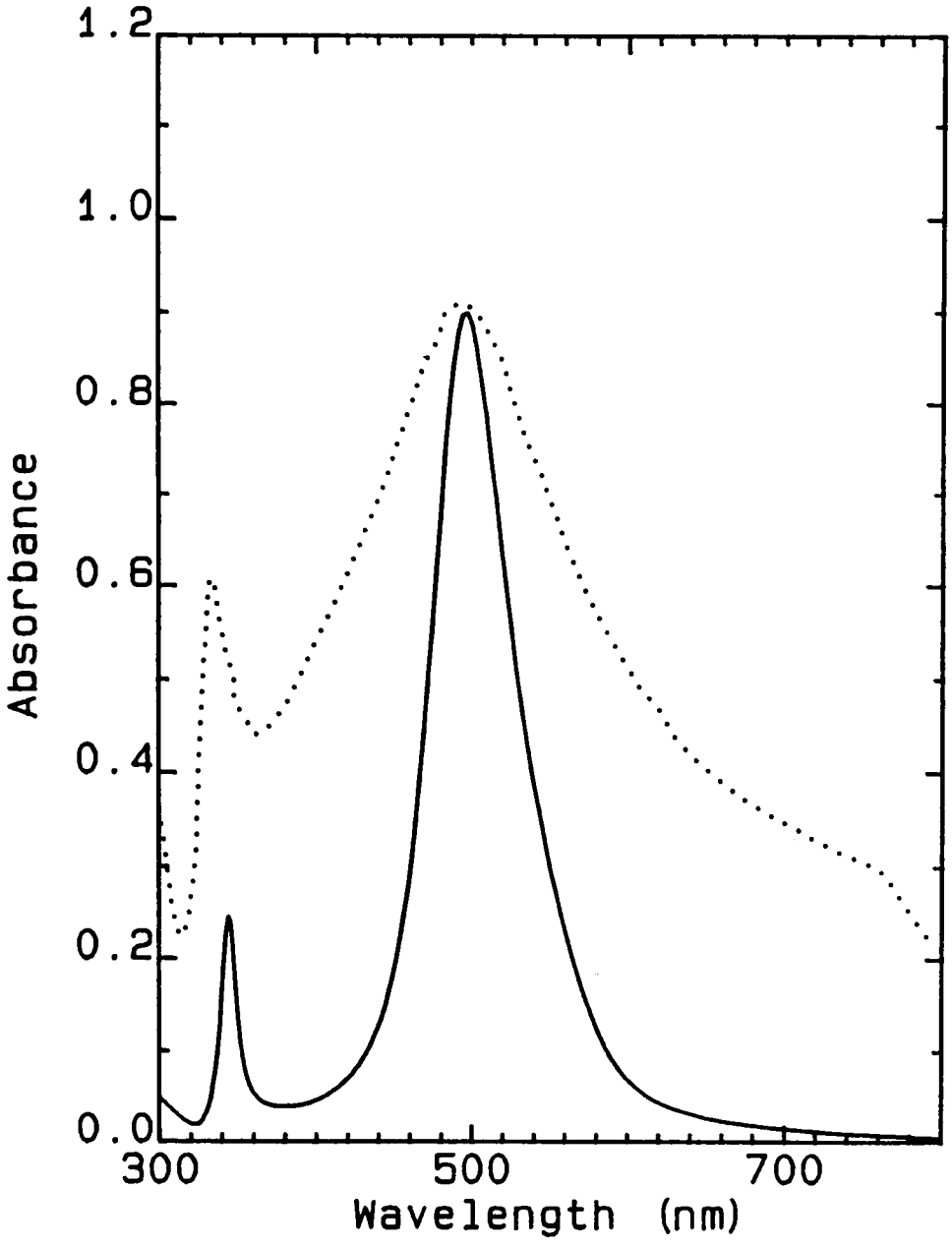



Figure 4-8. Comparison of experimental and theoretical absorbance for s-polarized light at $\Phi$=0°, $\theta$=45°. The solid curve is theoretical absorbance using two ellipsoids whose longest principal axes are perpendicular to one another. A Gaussian shape distribution has been included. The dotted curve is experimental data for 15 nm of silver deposited at 35° to the sample normal.

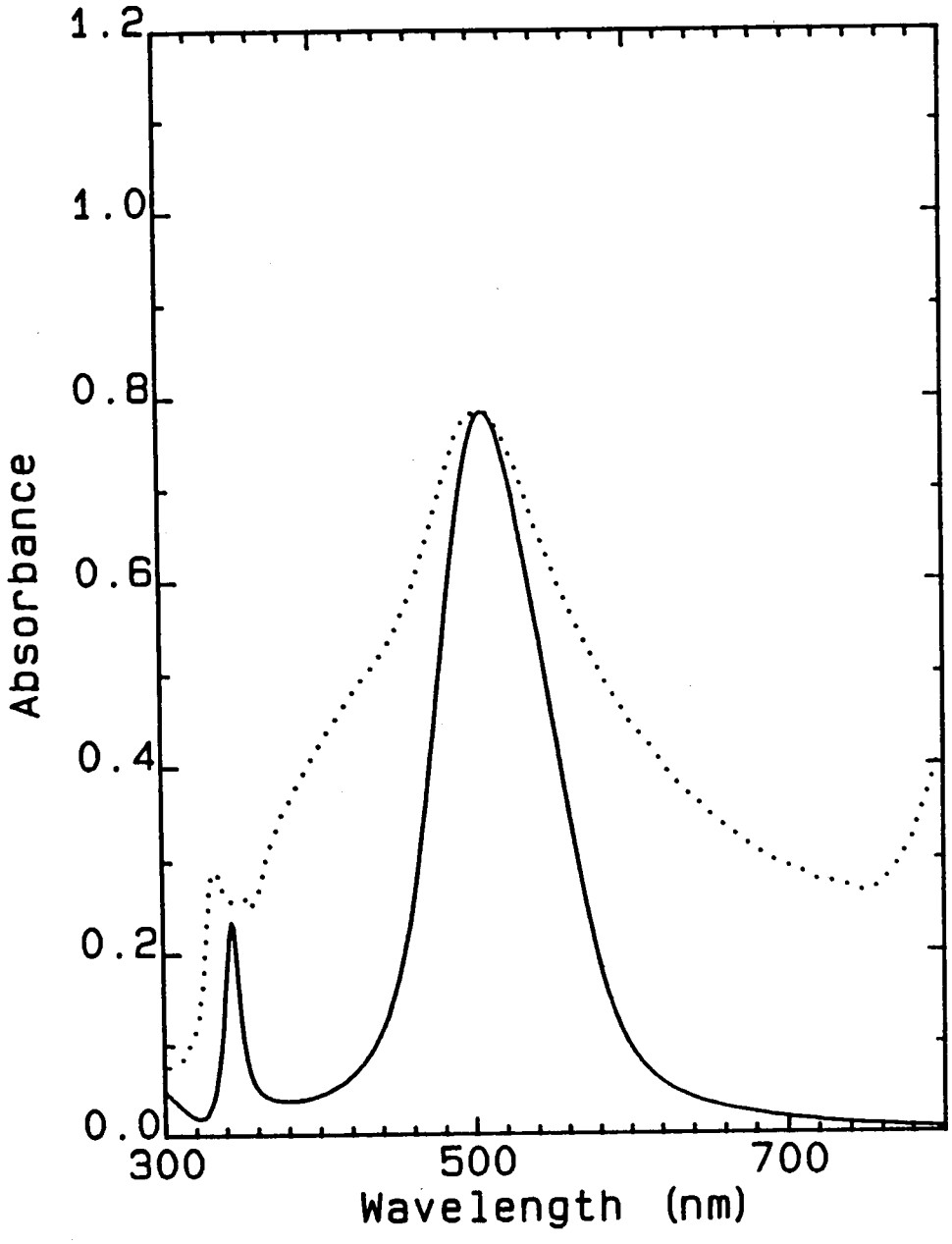



Figure 4-9. Comparison of experimental and theoretical absorbance for s-polarized light at $\Phi$=0°, $\theta$=90°. The solid curve is theoretical absorbance using two ellipsoids whose longest principal axes are perpendicular to one another. A Gaussian shape distribution has been included. The dotted curve is experimental data for 15 nm of silver deposited at 35° to the sample normal.

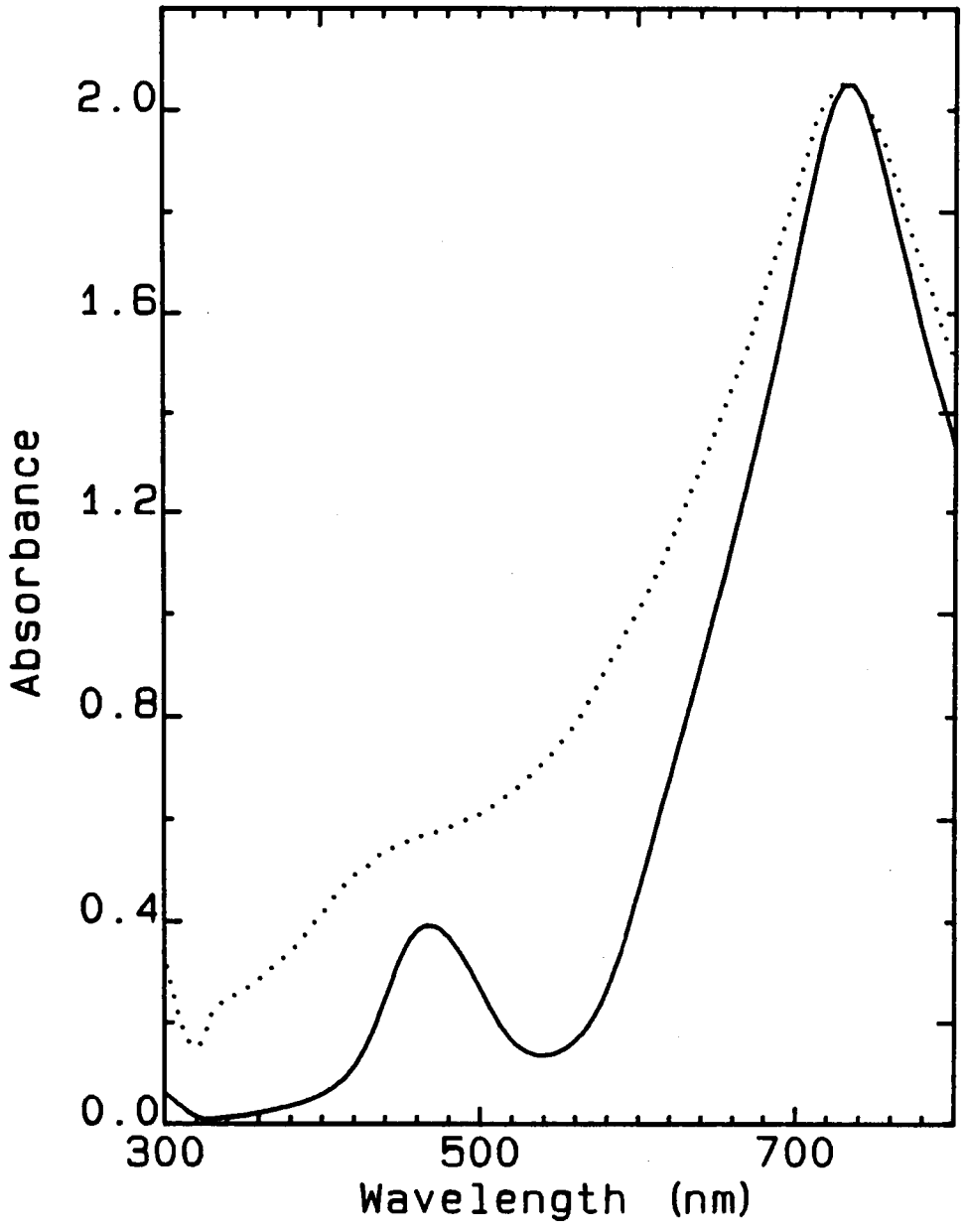



Figure 4-10. Comparison of experimental and theoretical absorbance for p-polarized light at $\Phi$=0°, $\Theta$=0°. The solid curve is theoretical absorbance using two ellipsoids whose longest principal axes are perpendicular to one another. A Gaussian shape distribution has been included. The dotted curve is experimental data for 15 nm of silver deposited at 35° to the sample normal.

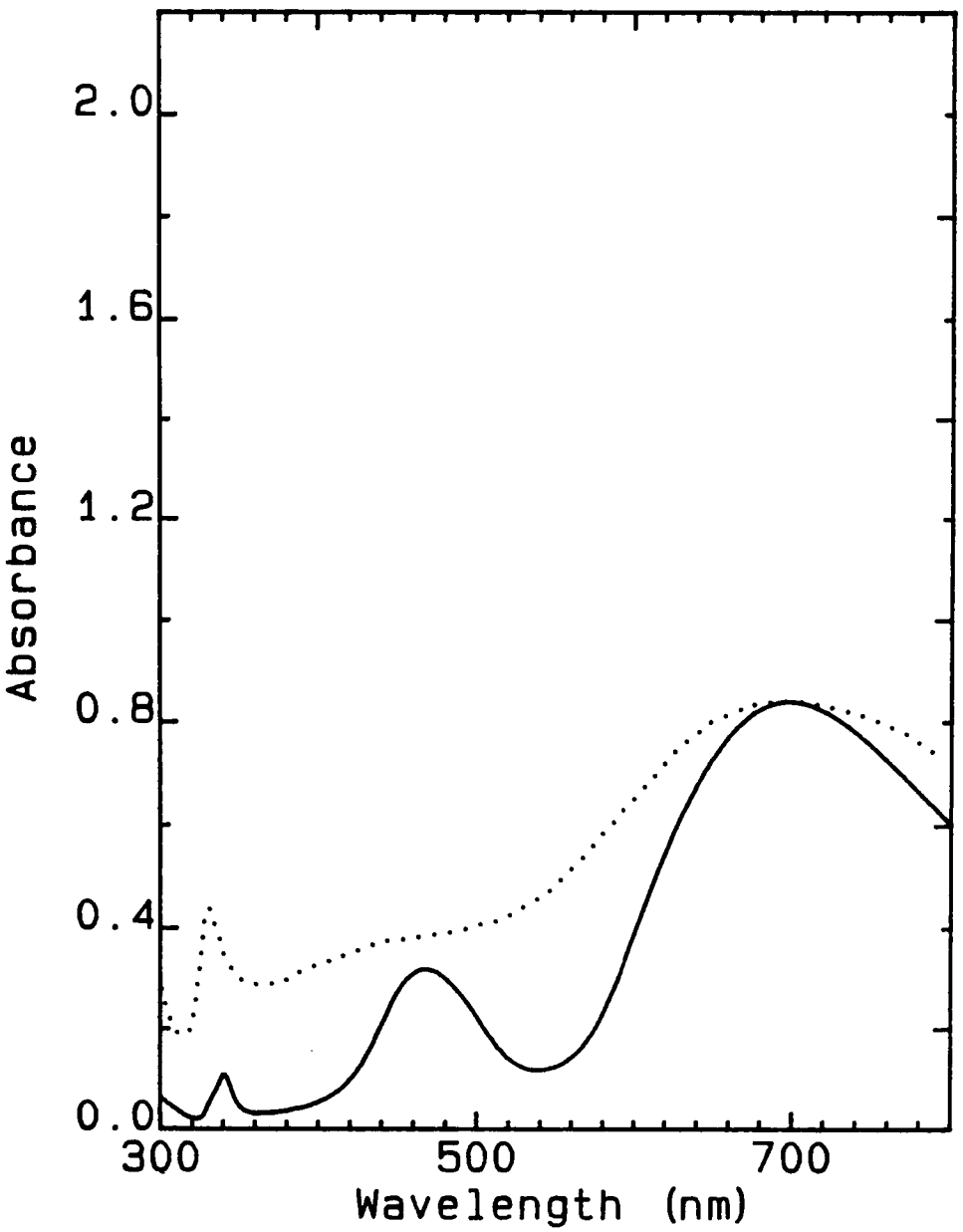



Figure 4-11. Comparison of experimental and theoretical absorbance for p-polarized light at $\Phi$=0°, $\theta$=45°. The solid curve is theoretical absorbance using two ellipsoids whose longest principal axes are perpendicular to one another. A Gaussian shape distribution has been included. The dotted curve is experimental data for 15 nm of silver deposited at 35° to the sample normal.

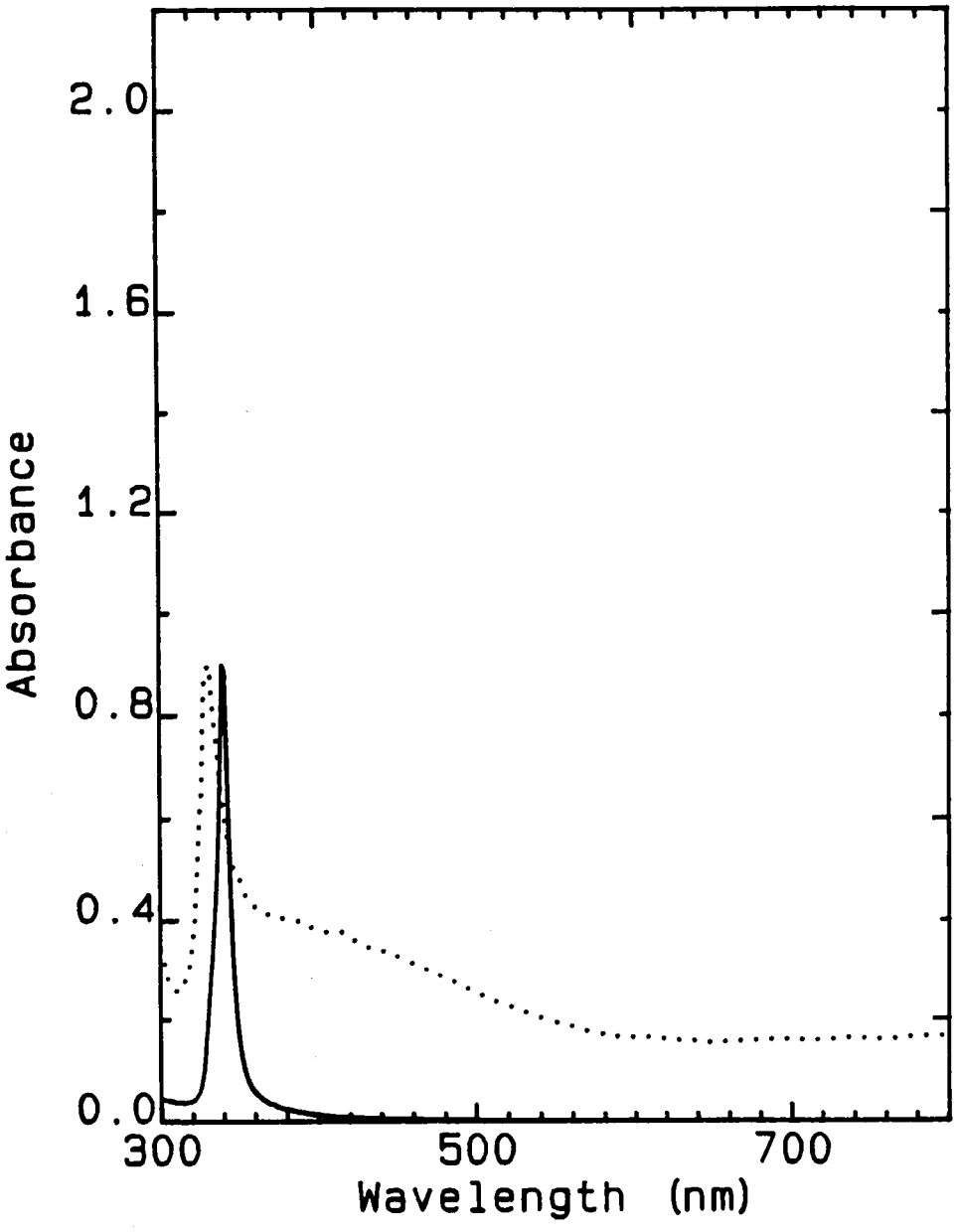



Figure 4-12. Comparison of experimental and theoretical absorbance for p-polarized light at $\Phi$=0°, $\theta$=90°. The solid curve is theoretical absorbance using two ellipsoids whose longest principal axes are perpendicular to one another. A Gaussian shape distribution has been included. The dotted curve is experimental data for 15 nm of silver deposited at 35° to the sample normal. .

an absorbance peak at 720 nm and a peak at 480 nm. These two peaks grow progressively weaker with increasing angle and do not appear in the 90° data. Another peak at 340 nm does not appear in the normal incidence data and grows with increasing angle. For p-polarization at normal incidence the electric vector is parallel to the post axis. Thus a charge-density oscillation is stimulated along the a-axis of the type 1 particles and the b-axis of the type 2 particles resulting in the absorbance peaks at 720 nm and 480 nm respectively. For angles between 0° and 90° the electric vector has a component parallel and a component perpendicular to the post axis. This stimulates oscillations along the a- and c-axis of type 1 particles and along the b- and c-axis of type 2 particles. In the 45° data the absorbance peak at 340 nm is the result of c-axis oscillations of both particles with resonances at nearly the same wavelength. The 720 nm and 480 nm peaks are, as in the normal incidence data, oscillations along the a-axis of type 1 particles and the b-axis of type 2 particles. At 90° the electric vector is completely perpendicular to the post axis and stimulates oscillations only along the c-axes of both types of particles. Therefore the only absorbance peak is the 340 nm peak in this case.

Figure 4-13 shows a comparison of the experimental results with the calculations for silver ellipsoids. The allowed values of the dielectric function were calculated using Eq. (2-125). The optical data for silver was used to find the oscillation energies of these values for silver. The triangles and the boxes represent the modes for

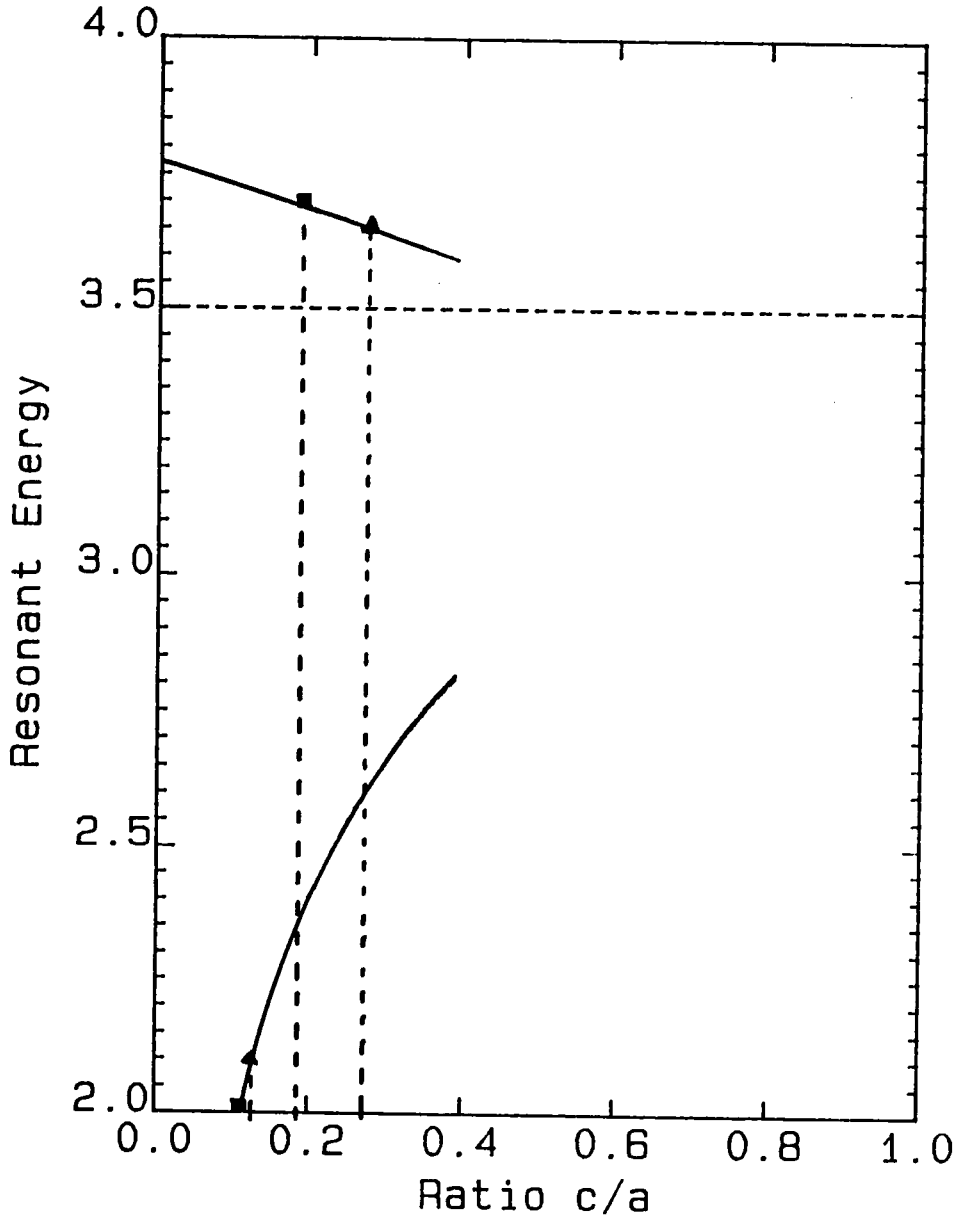



Figure 4-13. A comparison of the measured resonance peaks with those calculated for silver from the allowed values of the dielectric function and the bulk silver optical data. The squares are the a-axis and the c-axis measured resonace positions for one shape and the triangles are the same resonance modes for a different shape. The solid lines are the calculated resonant energies as a function of shape

two different shapes. The resonant mode along the a-axis and the resonant mode along the c-axis is shown. The two modes predict a most probable shape range for the particle.

In all the absorbance data shown here the measured absorbance is higher in general than the calculated absorbance. The calculations do not account for bulk absorbance of the silver that forms the particles. Also, there is silver deposited on the flat parts of the substrate that contributes to the absorbance of the samples. For comparison, the absorbance of a thin film of silver was measured and is shown in Figures 4-14 and 4-15 for the two polarizations used in this study. The film thickness was 14 nm.

It may be argued that some of the effects attributed to this second type of ellipsoid could actually be higher order oscillation modes resulting from particle size effects. For wavelengths used in this experiment, higher order modes occur concurrently with effects due to retardation. The effects of retardation are to broaden and red shift resonance peaks. To investigate this possibility we made two additional systematic studies of silver ellipsoids formed on posts.

In the first study we formed ellipsoids with thicker depositions of silver while keeping the angle of evaporation the same. Since the average a-axis and b-axis lengths are determined by evaporation angle, post diameter, and shadowing of posts by one another, these axis lengths are independent of evaporation depth. The c-axis lengths will vary directly with the thickness of the evaporated silver. For

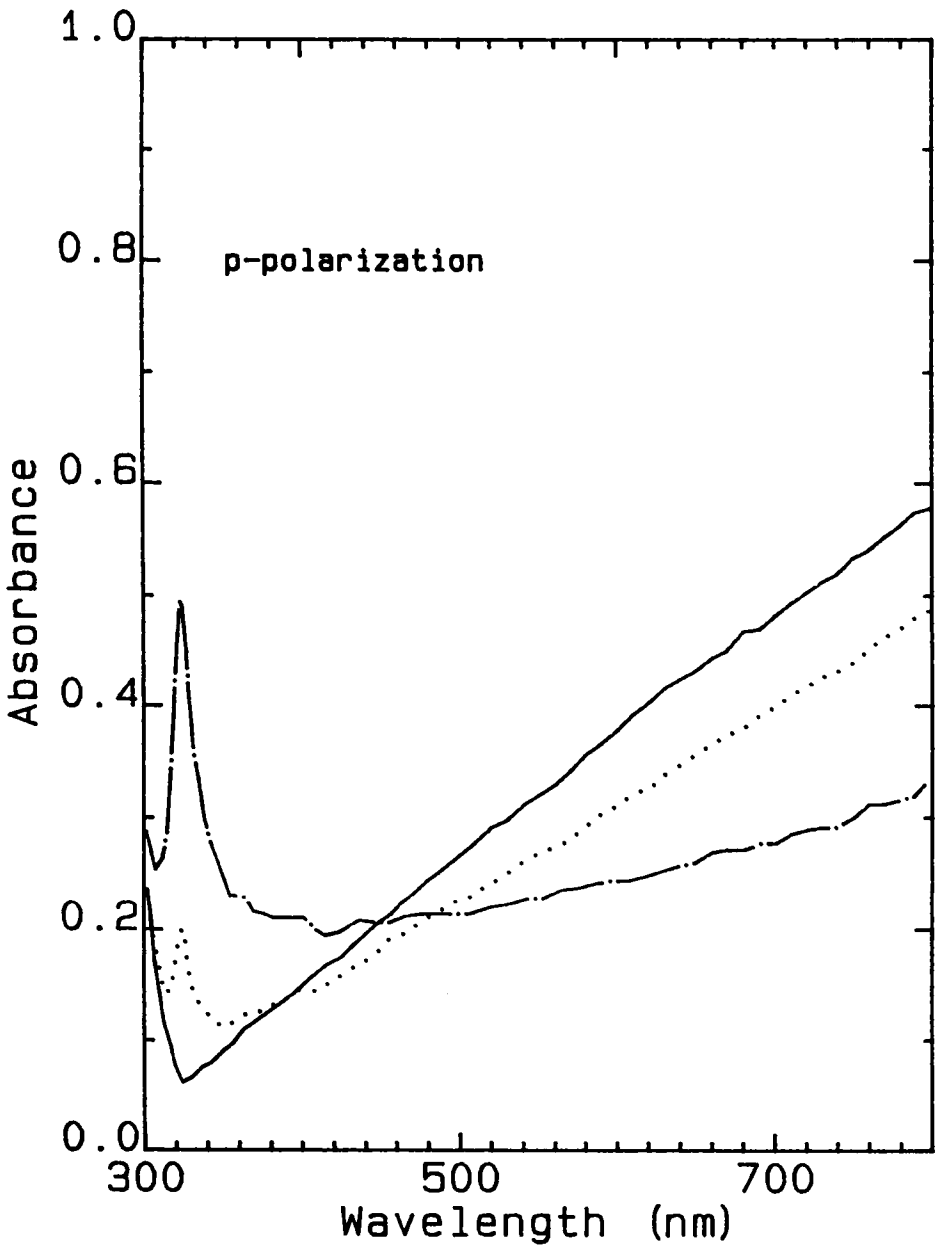



Figure 4-14. The absorbance of a thin silver film for p-polarized light. The absorbance is due to the bulk absorption of silver. The thickness is 12 nm. The solid line is for light at normal incidence, the dotted line is for light at 40° from the normal and the dash-dotted line is for light at 70° from the normal.

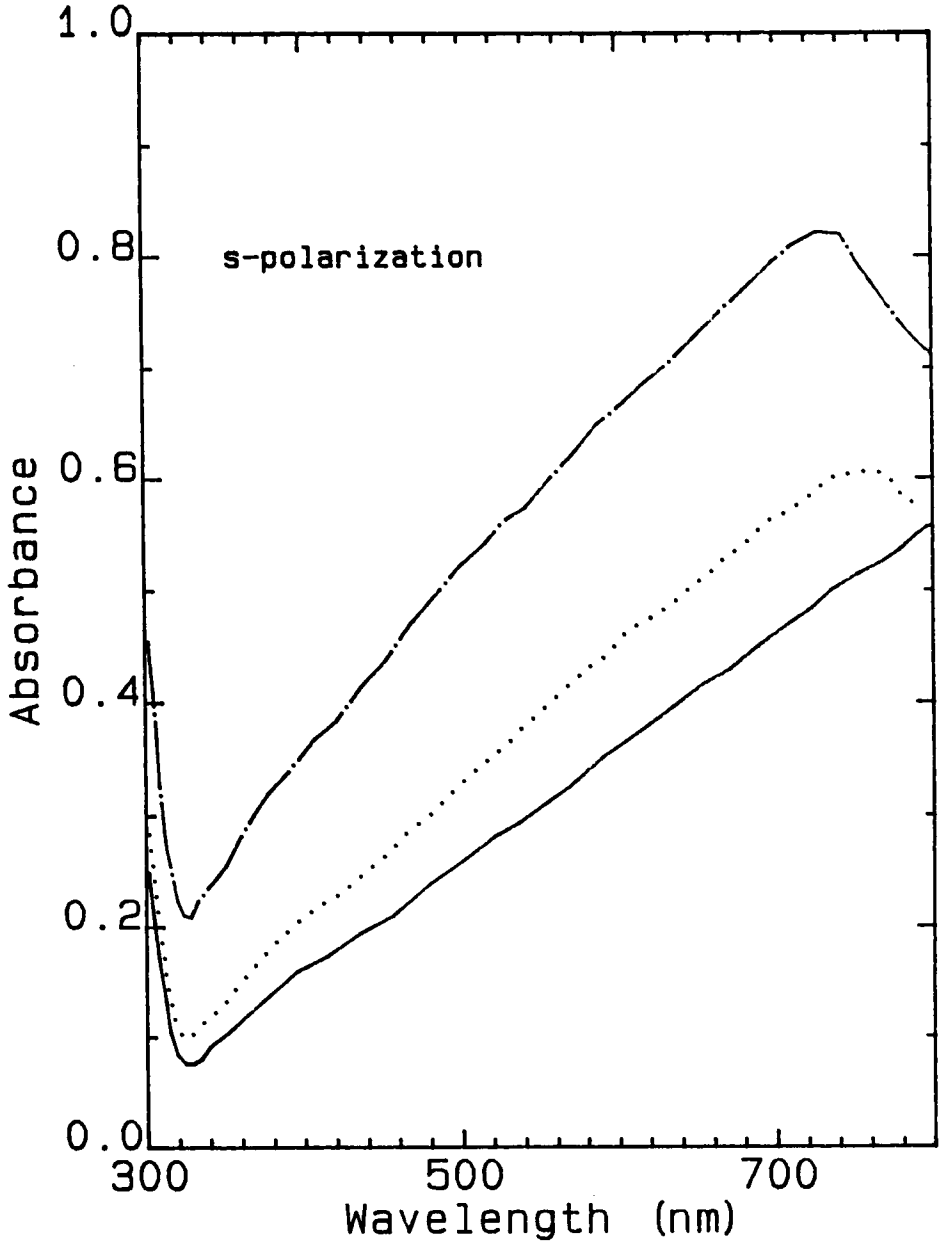



Figure 4-15. The absorbance of a thin silver film for s-polarized light. The absorbance is due to the bulk absorption of silver. The thickness is 12 nm. The solid line is for light at normal incidence, the dotted line is for light at 40° from the normal and the dash-dotted line is for light at 70° from the normal.

thicknesses ranging from 25 to 40 nm we find a substantial rise in the absorbance peak heights attributed to the type 2 particle relative to the other peaks for increasing silver depth. We also find a corresponding rise in the number of bridged posts that appear in scanning electron micrographs of these samples. Also we have heated our samples to temperatures ranging from 100 to 200 °C for 1 min and measured the optical absorbance after annealing. We find a blue shift in the a- and b-axis resonance positions when compared with the measurements of the same sample before heating. There is also a slight increase in the peak height for the absorbance peaks attributed to the type 2 ellipsoids. The blue shift indicates that the ellipsoids are less elongated, tending toward a more spherical shape and that the a- and b-axes are shorter than those of the unheated sample. This change occurs because the surface tension of the silver forms a more spherically shaped ellipsoid (a lower self-energy configuration) when the mobility of the silver is increased by the elevated temperature. The small increase in peak height appears to be due to a superposition of the absorbance as the resonance positions move closer together plus an increase in the number of bridged particles.

In the second study the evaporation depth was maintained at 20 nm and the angle of evaporation was changed. We made evaporations at 25°, 35°, 45°, and 55° with respect to the sample normal. Each time the absorbance was measured for both polarizations and measurements were made after heating to 100 °C, 150 °C, and 200 °C for 1 min. Each time

scanning electron micrographs were made to get a measure of the size and shape of the ellipsoids. For silver deposited at 25°, a significant number of nearly oblate ellipsoids were formed on the flat parts of the substrate. The formation of these ellipsoids decreased to a negligible number for the 45° and 55° depositions. At all angles the number of resonance peaks was consistent. There is some structure in the 25° and 35° absorbance data that does not appear in the other two measurements. This is due to the decrease of silver on the flat parts of the substrate at larger angles of deposition. The shoulder appearing in the s-polarized data at around 400 nm appears to be due to this silver. With increasing temperature the a- and b-axis resonances blue shift from the unheated positions. In heating from 150° to 200° we found that the a-axis resonance of the type 2 particle would red shift slightly for all angles except the 45° data. For this deposition angle the peak position continued to blue shift about 5 nm when heated from 150° to 200° . The red shift can be attributed to additional bridging of nearby ellipsoids to form a single one. The relative peak heights for the resonances are about the same for all angles.

For the measurements at thicker depths only the c-axis depth is altered and is at most 40 nm which is well below the 55 nm limit of reference [2.4]. Therefore we expect to observe no relative increase in the additional absorbance peaks if they are due to increased size effects. In the measurements of the heated samples the a- and b-axis lengths were shortened by the elevated temperature. In these

measurements, if the additional absorbance structure is due primarily to size then we would expect to see a decrease in the relative peak heights of this additional structure. In both cases we saw a rise in the heights of the peaks associated with the type 2 ellipsoids. The purpose in depositing silver at larger angles and heating the sample was to produce ellipsoids with dimensions smaller than the higher order mode limit. The micrographs show that the dimensions at 55 were less than the spherical limit of reference [2.4]. Again we would expect to see a change in the absorbance spectra if some of the structure is due to size effects. The 55° data is consistent with the other measurements. From this we conclude that while there may be effects of particle size and retardation in our measurements, the additional absorbance structure is indeed due a second type of ellipsoid as we have described.

In a related study, the posts were produced by a field assisted form of microlithography [4.1]. Silver posts were formed by using a roughened substrate as one half of a simple capacitor. A high field was applied and silver evaporated between the capacitor electrodes perpendicular to the field lines. Concentrated field strength at roughness points caused silver to be deposited on those points forming posts. These posts have aspect ratios approaching 7:1. The posts have parallel major axes and are formed on a low absorbance substrate. Absorbance measurements were made and compared to the calculations presented here. Good agreement was obtained in this comparison by

modeling the posts as ellipsoids that are nearly prolate spheroids. Only a single type of particle was assumed in this comparison. Figures 4-16 and 4-17 show p- and s-polarization comparisons respectively.

The posts formed by this technique are approximately 200 nm in the largest dimension. This dimension is well beyond the spherical size limit mentioned earlier; therefore, if the absorbance structure that we attribute to type 2 particles is due to particle size we should see some of that structure in the absorbance of these samples. None of the type 2 particle absorbance structure appears in the measurements for s-polarized light on these posts. The p-polarized measurements shows the shoulder at about 500 nm that appears in the measurements of the present study although it does not appear as strongly in the field-assisted samples. The data of this study tends to reinforce the previous conclusions about a second type of particle but raises a question about the origin of the extra structure in the p-polarized data. This shoulder also appears in absorbance data of particles formed on a post substrate produced by a silver-island etch mask technique [4.2]. The particles formed this way are somewhat smaller than those of the present study and significantly smaller than those formed by the field-assisted method. It is reasonable to expect the absorbance of the smaller particles to have little or none of this structure if it is due to retardation. The structure is, however, about the same strength in all of the data. It is apparent that more work needs to be done to understand the origin of this absorbance structure.

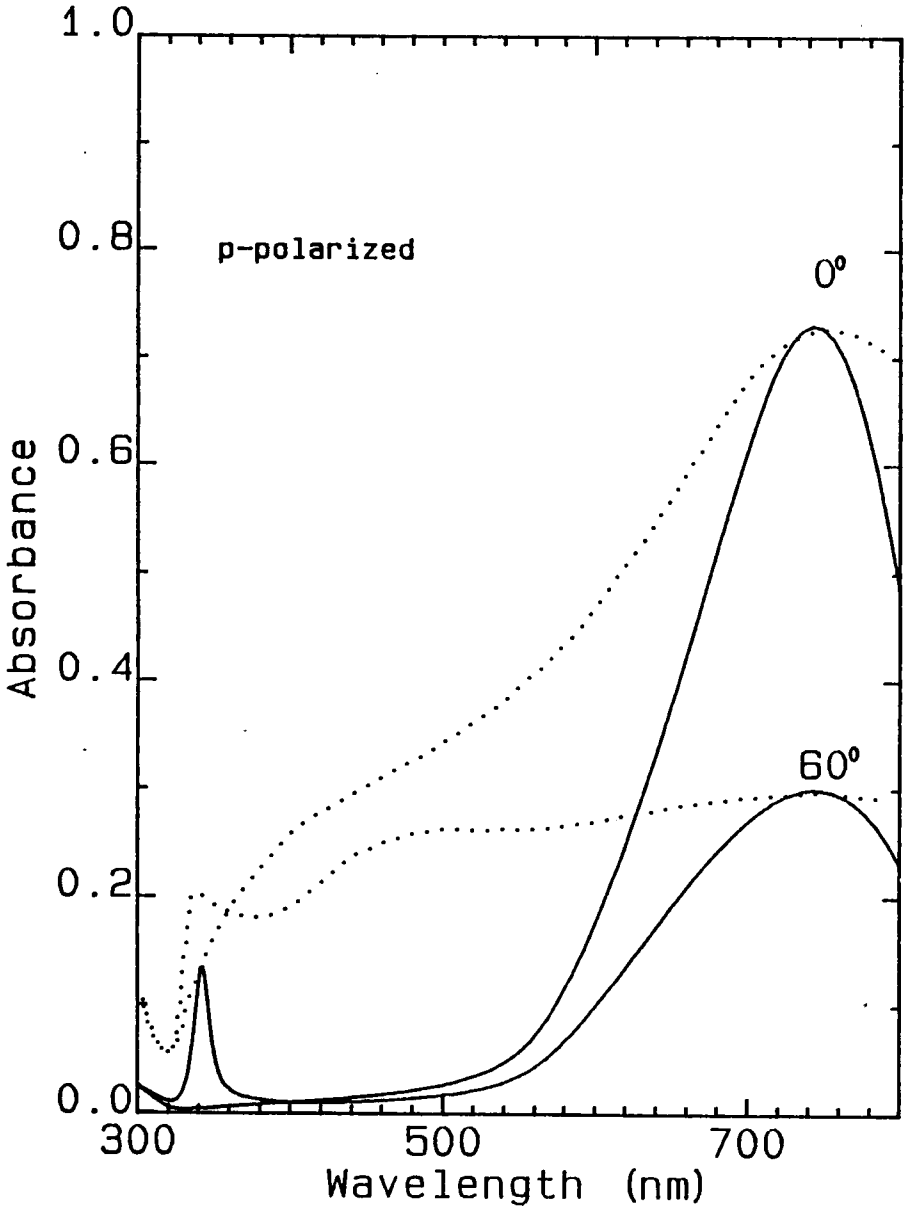



Figure 4-16. Measured and calculated absorbance for silver posts produced by a field-assisted evaporation technique. The incident light is p-polarized. A single particle is used in the calculation. A Gaussian distribution is included. The dotted lines are measured absorbance and the solid lines are calculated absorbance. The angle of the incident light is measured from the sample normal.

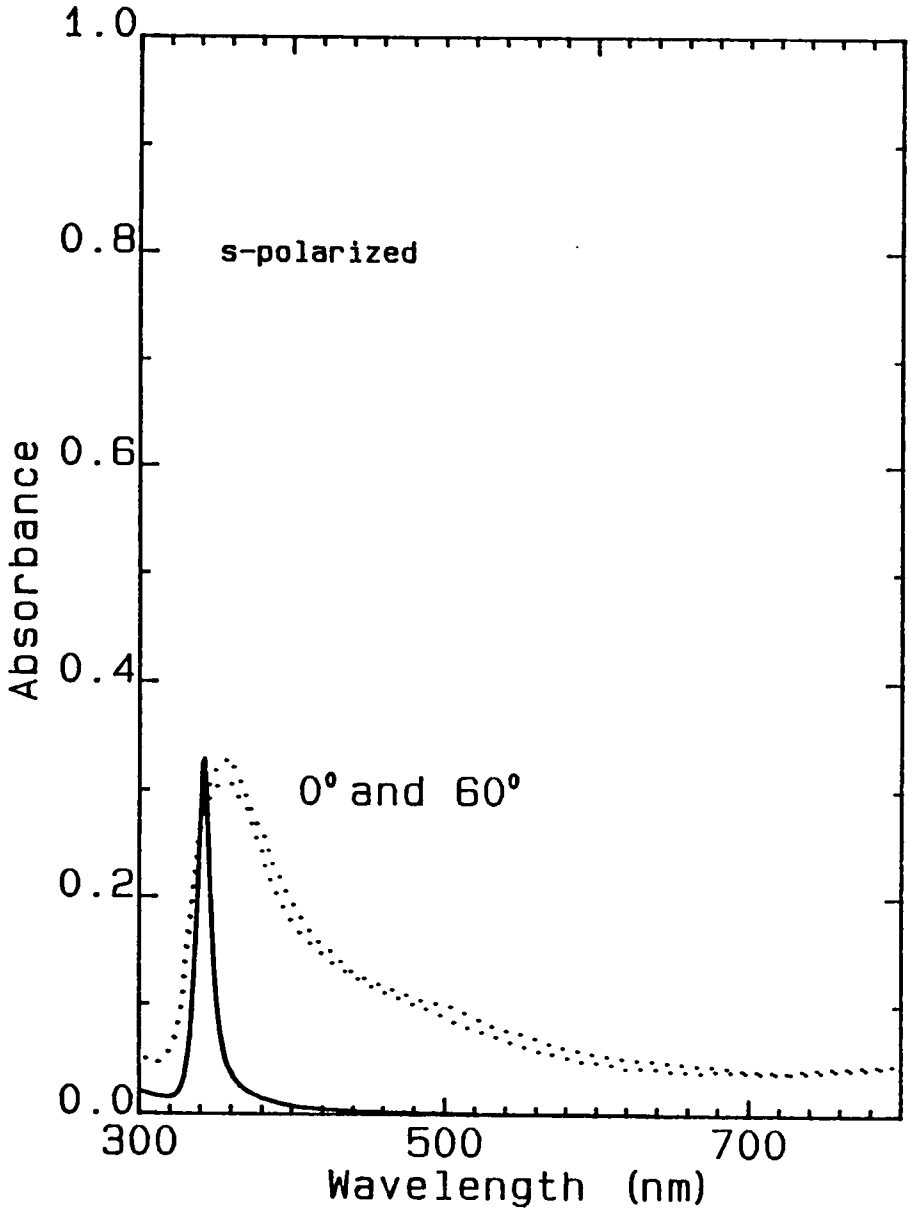



Figure 4-17. Measured and calculated absorbance for silver posts produced by a field-assisted evaporation technique. The incident light is s-polarized. A single particle is used in the calculation. A Gaussian distribution is included. The dotted lines are measured absorbance and the solid lines are calculated absorbance. The angle of the incident light is measured from the sample normal.

## C. SUBSTRATE EFFECTS

In all of the comparisons given here the effects of the underlying substrate have been ignored. The calculations were made for ellipsoids in vacuum. If they were totally immersed in a dielectric medium, the resonance is shifted by multiplying the resonance expressions obtained from the boundary conditions by the dielectric function of the surrounding medium. The substrate can interact with the charge-density oscillations shifting the resonances by depolarizing the particle. The substrates used in this experiment consist of both quartz posts and an underlying slab of quartz. This interaction cannot be calculated exactly. However, because the induced fields are due to dipole oscillations they are inversely proportional to the cube of the distance from the center of the ellipsoid. Thus, any dielectric that is more than a few nanometers from the particle surface will not interact with the induced fields. Therefore we may neglect the substrate except for the area of the posts that is in direct contact with the silver particles.

It is possible to obtain an estimate of the effect of the posts on the resonances by using a modified thin film approximation [4.3]. The resonance expression for the dielectric function for each mode of oscillation is modified in the same manner as for a continuous thin film on a substrate; a problem that can be solved exactly. This approximation gives a new resonance position for each mode.

Calculations using this approximation are compared with absorbance spectra for silver island films modeled as oblate spheroids in reference [4.3] and demonstrate good agreement. It is most accurate for very flat, close lying particles on a flat substrate. While the ellipsoids produced on the posts are very flat they are not close enough for any interparticle interaction. Averaging over an array of particles, the interaction is altered from a reciprocal distance cubed to a reciprocal distance. However this is still a small effect for the samples prepared in this work. For other samples the effect of this interaction is to shift the energy of the resonances. They reside on posts with a large radius of curvature compared to the particle thickness and so could only be considered approximately flat. This approximation, then, probably overestimates coupling of the silver with the substrate.

The effect of the substrate is to red shift the resonance position of the charge-density oscillations along the a- and b-axis of each type of ellipsoid but the resonance position of the c-axes is almost unaffected. Using the approximation to adjust the value of the dielectric function, the calculations predict a shape that is in better agreement with the measured shape of the silver ellipsoids. The fitting parameters used with the substrate effect included are a=60 nm with axis ratios b/a=0.215 and c/a=0.145 for particle type 1 and a=35 nm with axis ratios b/a=0.8 and c/a=0.18 for particle type 2. Table 4-1 is a summary of the fitting parameters used and those measured from the micrographs.

Table 4-1. Fitting parameters and SEM measurements for silver ellipsoid-like particles.

| Fitting parameters for calculations | | | | |
|---|---|---|---|---|
| | substrate interaction particle | | no substrate interaction particle | |
| | type 1 | type 2 | type 1 | type 2 |
| b/a | .215 | .80 | .165 | .84 |
| c/a | .145 | .18 | .145 | .14 |
| a-axis length (nm) | 60 | 35 | 60 | 35 |
| total particle density | 53.6 $(nm)^2$ | | 66.8 $(nm)^2$ | |

| SEM measurements | | |
|---|---|---|
| | particle type 1 | particle type 2 |
| b/a | .67 | 1.0 |
| c/a | .101 | .107 |
| a-axis length (nm) | 74 | 70 |
| total particle density | 49 $(nm)^2$ | |

By studying the parameters here it is obvious that there is a difference in the axis lengths used to calculate absorbance and those observed in the micrographs. The largest difference is in the b-axis length for the type 1 particle and the a-axis length for the type 2 particle. Both lengths measured in the micrographs appear to be about twice as long as those used to calculate the absorbance. We feel that this is due to the circular cross section of the posts. This curvature affects the particle formation in two ways. First, as the post surface curves away from the direction of evaporation the deposited silver is thinner. Secondly, the post curvature causes the formation of a particle shape that is not characteristic of an ideal ellipsoid. Apparently the resulting particle has an effective optical length along this direction for both particle types that is roughly half of the length observed in the micrographs.

## D. CONCLUSIONS

We have shown that the optical absorbance of ellipsoid like silver particles can be described as the stimulation of charge-density oscillations on the particle surfaces. Good agreement between the calculated absorbance and the measured results was obtained by using nonretarded electrodynamics and experimental optical constants for bulk silver. A two particle model was used and an estimated substrate effect on the resonances was included. Interparticle interactions were

neglected since they are necessary only to explain data from more closely spaced particles. Multiple scattering has been neglected.

Microlithographic techniques were used to produce arrays of silver particles approximately ellipsoidal in shape. The ellipsoids were produced in a well-defined orientation so that each sample contained ellipsoids with parallel principal axes. This allowed determination of the angular and polarization dependence of the optical absorbance. This dependence could not have been measured for ellipsoids with random orientations.

Calculation of correction terms for retardation effects appears to be possible only by the use of spheroidal wave functions. These functions must be evaluated by numerical techniques and utilize at least nine different normalizations. This makes correlation with other calculations in the literature very difficult. The solution of this problem alone is worthy of a thesis project and is beyond the scope of this experimental work.

While optical absorbance methods are beneficial for determining shapes much smaller than the wavelength of light, [4.4] our analysis demonstrates that care must be taken in modeling geometries of similarly produced particles even for fairly regular substrates. Thus, for example, while our samples give extremely large enhancements in surface-enhanced Raman scattering, [4.2] it is difficult to draw unequivocal relations between the surface plasmon and the Raman enhancement.

There are some unresolved problems with the calculations and the measured absorbance. The experimental absorbance throughout the visible region is in general higher than the theory can predict. Part of this may be resolved by including the bulk absorbance of silver. If the shape distribution is broadened the peak absorbance will be lowered. Renormalization to the measured value results in particle densities that are much too high. This is presently unresolved. There is also an angular dependence in the data that is yet to be resolved.

The essential result of this work is that a simple model using a single-particle theory does predict the resonant frequencies and the polarization dependence. This should give valuable information for surface-enhanced Raman applications.

By using this sample production technique it may be possible to reduce the post size and obtain longer range order for the post arrays. Smaller posts would produce silver ellipsoids with dimensions closer to or less than the retardation limit and reduction of the shape distribution from longer range order would result in more narrow peaks in the absorbance spectrum.

Characterization of particles produced in a well-defined orientation should prove useful in surface plasmon related phenomena such as surface-enhanced Raman scattering [4.2], [4.5] metal-insulator-metal tunnel junctions [4.6], and photoemission.

# REFERENCES

# REFERENCES


[1.1] J.P. Goudonnet, G.M. Begun, and E.T. Arakawa, Chem. Phys. Lett. 92, p. 197 (1982).

[1.2] D.A. Weitz, S. Garoff, C.D. Hanson, T.J. Gramila, and J.I.Gersten, Opt. Lett. 7, p. 89 (1982).

[1.3] J. R. Goudonnet, T. Inagaki, T. L. Ferrell, R. J. Warmack, M. C. Buncick, and E. T. Arakawa, Chem. Phys. 106, pp. 225-232 (1986).

[1.4] Craig F. Bohren and Donald R. Huffman, *Absorbtion and Scattering of Light by Small Particles*, (Wiley-Interscience, New York 1983), pp. 3-4.

[1.5] D. Bohm and D. Pines Phys. Rev. 82, p. 625 (1951); Phys. Rev. 85, p. 338 (1952); Phys. Rev. 92, p. 609 (1953); D. Pines, Phys. Rev. 92, P. 626 (1953).

[1.6] R. H. Ritchie, Phys. Rev. 106, p. 874 (1957).

[1.7] R. H. Ritchie, Surface Science 34, p. 1 (1973).

[1.8] W. Steinmann, Phys. Stat. Sol. 23, p. 437 (1968).

[1.9] H. Raether, *Springer Tracts in Modern Physics* (Springer-Verlay, Berlin and New York, 1980), 88.

[1.10] T. L. Ferrell, T. A. Callcott, and R. J. Warmack, American Scientist 73, pp. 334-353, (1985).

[1.11] P. O'Neill and A. Ignatiev, Phys. Rev. B, 18, p. 6540 (1978).

[1.12] P. C. Hammel and R. C. Richardson, Physics 107 B, p. 611 (1981).

[1.13] S. W. Kennerly, J. W. Little, R. J. Warmack, and T. L. Ferrell, Phys. Rev. B. 29, p. 2926 (11984).

[1.14] R. J. Warmack and S. L. Humphrey, Phys. Rev. B 34, p. 2246 (1986).

[1.15] M. C. Buncick, R. J. Warmack, and T. L. Ferrell, Bull. Am. Phys. Soc. 29, p. 1501 (1984).

[1.16] H. W. Lehmann, R. Widmer, M. Ebnoether, A. Wokaun, M. Meier, and S. K. Miller, J. Vac. Sci. Technol. B 1, p. 1088 (1983).

[1.17] M. C. Buncick, R. J. Warmack, and T. L. Ferrell, Bull. Am. Phys. Soc. 30, p. 1783 (1985).

[1.18] M. C. Buncick, R. J. Warmack, J. W. Little, and T. L. Ferrell, Bull. Am. Phys. Soc. 28, p. 10 (1983).

[1.19] P. F. Liao, in *Surface Enhanced Raman Scattering*, R. K. Chang and T. E. Furtak, eds. (Plenum, New York, 1982).

[1.20] J. C. Oro and J. C. Wolfe, J. Vac. Sci. Technol. B 1, p. 1088 (1983).

[1.21] C. A. Spindt, C. E. Holland, and R. D. Stowell, Journal De Physique, Colloque C9, supplement au n 12, Tome 45, p. C9-269 (1984).

[1.22] G. A. Kitzmann, Journal De Physique, Colloque C2, supplement au n 3, Tome 47, p. C2-79 (1986).

[1.23] H. W. Deckman and J. H. Dunsmuir, Appl. Phys. Lett. 41, p. 377 (1982).

[1.24] B. K. Russell, J. G. Mantovani, V. E. Anderson, R. J. Warmack, and T. L. Ferrell, Phys. Rev. B, 35, p. 2151 (1987).

[1.25] R. H. Ritchie, J. C. Ashley, and T. L. Ferrell in *Electromagnetic Surface Modes*, A. D. Boardman, ed. (Wiley, New York, 1982).

[2.1] J.D. Jackson, *Classical Electrodynamics*, (Wiley and Sons, New York, 1975), p. 218.

[2.2] J.A. Stratton, *Electromagnetic Theory*, (McGraw Hill, New York, 1941), p. 24.

[2.3] Jackson, Op. cit., p. 292.

[2.4] Jackson, Op. cit., p. 623.

[2.5] B.K. Russell, T.L. Ferrell, V.E. Anderson, R.J. Warmack, and J.C. Montovani, Phys. Rev. B 35, 2151 (1987).

[2.6] G.Mie, Ann. Phys. 25, 377 (1908).

[2.7] R.H. Ritchie, Phys. Rev. 106 p. 874 (1957).

[2.8] William R. Smythe, *Static and Dynamic Electricity*, 3rd. ed. (McGraw Hill, New York, 1968), p. 168.

[2.9] Parry Moon and Domina Spencer, *Field Theory for Engineers*, (D. Van Nostrand Co. Inc., New York, 1961) p. 267.

[2.10] Smythe, Op. cit., p. 177.

[2.11] Moon and Spencer, Op. cit., p. 237.

[2.12] Stratton, Op. cit., p. 58.

[2.13] Parry Moon and Domina Spencer, *Field Theory Handbook*, (Springer-Verlag, Berlin, 1961), p. 41.

[2.14] Smythe, Op. cit., pp. 158-159.

[2.15] George Arfken, *Mathematical Methods for Physicists*, 3rd. ed. (Academic Press, Orlando 1985), p. 685.

[2.16] Smythe, Op. cit., p. 158.

[2.17] R.H. Ritchie, J.C. Ashley, and T.L. Ferrell, *Electromagnetic Surface Modes*, A.D. Boardman ed., (Wiley, New York, 1982), Chap. 3.

[2.18] Smythe, Op. cit., p. 161.

[2.19] Jackson, Op. cit., p. 137.

[2.20] Stratton, Op. cit., p. 211.

[2.21] Arfken, Op. cit., p. 471.

[2.22] Murray R. Spiegel, *Mathematical Handbook of Formulas and Tables*, Schaum's Outline Series, (McGraw Hill, New York, 1968), p. 63

[2.23] S.W. Kennerly, M.S. Thesis, The University of Tennessee, December, 1983.

[2.24] Jackson, Op. cit., p. 412.

[2.25] Jackson, Op. cit., p. 453-454.

[2.26] Kennerly, Op. cit., p. 23.

[2.27] Max Born and Emil Wolf, *Principles of Optics*, 5th. ed., (Pergamon, Elmsford, New York, 1975), p. 659.

[2.28] Kennerly, Op.cit. p. 24.

[2.29] Deutsches Elektronen-Syncrotron, (Hamburg 1974) Report No. DESY-SR-74/7, (unpublished).

[3.1] Esco Products, Inc., 171 Oak Ridge Rd., Oak Ridge, NJ 04738.

[3.2] Micro Liquid Laboratory Cleaner, Cole-Parmer Instrument Co., 7425 North Oak Ridge Ave., Chicago, IL 60648.

[3.3] Air Products and Chemicals, Inc., Box 2802, Allentown, PA 18105.

[3.4] Duke Scientific Corp., 2415 Embarcadero Way, Palo Alto, CA 94303.

[3.5] H.W. Deckman and J.H. Bunsmuir, Appl. Phys. Lett. 41, 377 (1982).

[3.6] R.D. Mathis Co., 2840 Gundry Ave., Long Beach, CA 90806.

[3.7] Shimadzu Scientific Instruments, Inc., 7102 Riverwood Dr., Comumbia MD 21046.

[3.8] Newport Corp.,18235 Mt. Baldy Circle, P.O. Box 8020, Fountain Valley, CA 92728-8020.

[4.1] M.J. Bloemer, T.L.Ferrell, M.C. Buncick, and R.J. Warmack, (unpublished).

[4.2] J. R. Goudonnet, T. Inagaki, T. L. Ferrell, R. J. Warmack, M. C. Buncick, and E. T. Arakawa, Chem. Phys. **106**, pp. 225-232 (1986).

[4.3] P. Royer,J. P. goudonnet, R.J. Warmack, and T.L.Ferrell, Phys. Rev. B 35, p. 3753 (1987).

[4.4] S. W. Kennerly, J. W. Little, R. J. Warmack, and T. L. Ferrell, Phys. Rev. B. 29, p. 2926 (11984).

[4.5] J.P. Goudonnet, G.M. Begun, and E.T. Arakawa, Chem. Phys. Lett. 92, p. 197 (1982).

[4.6] M. J. Bloemer, J. G. Mantovani, J. P. Goudonnet, D. R. James, R. J. Warmack, and T. L. Ferrell, Phys. Rev. B 35, p. 5947 (1987).

[A.1] Murray R. Spiegel, *Mathematical Handbook of Formulas and Tables*, Schaum's Outline Series, (McGraw Hill, New York, 1968), p. 128.

[A.2] William R. Smythe, *Static and Dynamic Electricity*, 3rd. ed., (McGraw Hill, New York, 1968), p. 170.

[A.3] Spiegel, Op. cit., p. 149.

[A.4] Smythe, Op. cit., p. 155.

[A.5] Spiegel, Op. cit., p. 128.

[A.6] Smythe, Op. cit., p. 170.

[A.7] Spiegel, Op. cit., p. 149.

[A.8] Smythe, Op. cit., p. 142.

[B.1] J.D. Jackson, *Classical Electrodynamics*, (Wiley and Sons, New York, 1975), p. 764. The complex spherical harmonics have been replaced by the real spherical harmonics.

[B.2] Jackson, Op. cit., p. 741.

# APPENDICES

# APPENDIX A

## OBLATE AND PROLATE SPHEROIDAL COORDINATES

### Oblate Coordinates

Oblate spheroidal coordinates $(\eta,\theta,\phi)$ have three associated families of mutually orthogonal surfaces. They are confocal ellipses, single-sheeted hyperboloids and half planes. The scale factors for oblate spheroidal coordinates are

$$h_\eta = a\left[\frac{\eta^2+\cos^2\theta}{1+\eta^2}\right]^{1/2} \tag{A-1}$$

$$h_\theta = a(\eta^2+\cos^2\theta)^{1/2} \tag{A-2}$$

and

$$h_\phi = a\sin\theta(1+\eta^2)^{1/2} \tag{A-3}$$

where a is the focal length of the ellipses. The radius vector is

$$\vec{r} = a\sin\theta(1+\eta^2)^{1/2}(\cos\phi\hat{i}+\sin\phi\hat{j}) + a\eta\cos\theta\hat{k} \tag{A-4}$$

where $(\hat{i},\hat{j},\hat{k})$ are the Cartesian unit vectors. The unit vectors for the oblate spheroidal coordinates are

$$\hat{e}_\eta = \frac{\eta\sin\theta}{(\eta^2+\cos^2\theta)^{1/2}}(\cos\phi\hat{i}+\sin\phi\hat{j}) + \cos\theta\left[\frac{\eta^2+1}{\eta^2+\cos^2\theta}\right]^{1/2}\hat{k} \tag{A-5}$$

$$\hat{e}_\theta = \cos\theta\left[\frac{\eta^2 + 1}{\eta^2 + \cos^2\theta}\right]^{1/2} (\cos\phi\hat{i} + \sin\phi\hat{j}) - \frac{\eta \sin\theta}{(\eta^2 + \cos^2\theta)^{1/2}} \hat{k} \quad \text{(A-6)}$$

and

$$\hat{e}_\phi = -\sin\phi\hat{i} + \cos\phi\hat{j} \quad \text{(A-7)}$$

The element of volume is

$$dV = a^3(\eta^2 + \cos^2\theta)\, d\eta\, \sin\theta d\theta d\phi \quad \text{(A-8)}$$

The gradient of a scalar is

$$\nabla\Phi = \frac{1}{a}\left[\frac{1}{(\eta^2 + \cos^2\theta)^{1/2}}\left[\frac{\partial\Phi}{\partial\eta}\hat{e}_\eta + \frac{\partial\Phi}{\partial\theta}\hat{e}_\theta\right] + \frac{1}{(\eta^2 + 1)^{1/2}\sin\theta}\frac{\partial\Phi}{\partial\phi}\hat{e}_\phi\right] \quad \text{(A-9)}$$

The divergence of a vector is

$$\nabla\cdot\vec{E} = \frac{1}{a(\eta^2 + \cos^2\theta)}\left[\frac{\partial}{\partial\eta}[(\eta^2 + \cos^2\theta)^{1/2}(\eta^2 + 1)^{1/2}E_\eta]\right] +$$

$$\frac{1}{a\sin\theta(\eta^2 + \cos^2\theta)}\frac{\partial}{\partial\theta}(\sin\theta(\eta^2 + \cos^2\theta)^{1/2}E_\theta) \frac{1}{a(1 + \eta^2)^{1/2}\sin\theta}\frac{\partial E_\phi}{\partial\phi} \quad \text{(A-10)}$$

Laplace's equation in oblate spheroidal coordinates is given by [A.1]

$$\nabla^2\Phi = \frac{1}{a(\eta^2 + \cos^2\theta)}\left[\frac{\partial}{\partial\eta}\left[(\eta^2 + 1)\frac{\partial\Phi}{\partial\eta}\right] + \frac{\partial}{\partial\theta}\left[\sin^2\theta\frac{\partial\Phi}{\partial\theta}\right] + \frac{\eta^2 + \cos^2\theta}{(1+\eta^2)\sin^2\theta}\frac{\partial^2\Phi}{\partial\phi^2}\right] \quad \text{(A-11)}$$

Using the standard separation of variables technique the potential is written as

$$\Phi = G(\eta)\, F(\theta)\, H(\phi) \quad \text{(A-12)}$$

Dividing by the potential, Eq. (A-11) becomes

$$\frac{(\eta^2+1)\sin^2\theta}{\eta^2+\cos^2\theta}\left[\frac{1}{G}\frac{\partial}{\partial\eta}\left[(\eta^2+1)\frac{\partial G}{\partial\eta}\right] + \frac{1}{F}\frac{\partial}{\partial\theta}\left[\sin^2\theta\frac{\partial F}{\partial\theta}\right]\right] + \frac{1}{H}\frac{\partial^2 H}{\partial\phi^2} = 0. \tag{A-13}$$

The last term is a function only of $\phi$ and, therefore, must separately be equal to a constant. If the constant us $-m^2$ then

$$\frac{\partial^2 H}{\partial\phi^2} = -m^2 H(\phi) \tag{A-14}$$

The solutions to Eq. (A-14) are [A.2]

$$H(\phi) = \begin{cases} K_{mp}\cos(m\phi) \\ L_{mp}\sin(m\phi) \end{cases} \tag{A-15}$$

Eq. (A-13) is now

$$\left[\frac{1}{G}\frac{\partial}{\partial\eta}\left[(\eta^2+1)\frac{\partial G}{\partial\eta}\right] + \frac{m^2}{1+\eta^2}\right] + \left[\frac{1}{F}\frac{\partial}{\partial\theta}\left[\sin^2\theta\frac{\partial F}{\partial\theta}\right] - \frac{m^2}{1-\cos\theta^2}\right] = 0. \tag{A-16}$$

Each of the terms in the square brackets is dependent only on a single variable, $\eta$ or $\theta$. Each term must then separately be equal to a constant, and because the sum is zero, one constant must be the negative of the other. If the constant is $\ell(\ell+1)$, then Eq. (A-16) may be separated into two differential equations

$$\frac{1}{F}\frac{\partial}{\partial\theta}\left[(1-\cos^2\theta)\frac{\partial F}{\partial\theta}\right] - \frac{m^2}{1-\cos\theta^2} = -\ell(\ell+1) \qquad \text{(A-17)}$$

and

$$\frac{1}{G}\frac{\partial}{\partial\eta}\left[(\eta^2+1)\frac{\partial G}{\partial\eta}\right] + \frac{m^2}{1+\eta^2} = \ell(\ell+1) \qquad \text{(A-18)}$$

The solutions to Eq. (A-17) are the Legendre polynomials [A.3]

$$F(\cos\theta) = A_{\ell m}\, P_{\ell m}(\cos\theta) + B_{\ell m}\, Q_{\ell m}(\cos\theta) \qquad \text{(A-19)}$$

$Q_{\ell m}(\cos\theta)$ may be disregarded because it is infinite at $\cos\theta=\pm1$. The solutions to Eq. (A-18) are the Legendre functions of imaginary argument [A.4]. Here both functions are included because each function will be restricted to a region where it remains finite as discussed below.

The complete solution to Laplace's equation is

$$\Phi = \sum_{\ell=0}^{\infty}\sum_{m=0}^{\ell}\sum_{p=\pm1}\left[C_{\ell m}\, P_{\ell m}(i\eta) + D_{\ell m}\, Q_{\ell m}(i\eta)\right]\left[A_{\ell m}\, P_{\ell m}(\cos\theta)\right]$$

$$\cdot \begin{cases} K_{mp}\cos(m\phi) \\ L_{mp}\sin(m\phi) \end{cases} \qquad \text{(A-20)}$$

The terms containing $\theta$ and $\phi$ can be combined into the real spherical harmonics. They are defined by

$$Y^{p}_{\ell m}(\theta,\phi) = \left[\frac{(2+\delta_o^m)(2\ell+1)(\ell-m)!}{4\pi(\ell+m)!}\right]^{1/2} P_{\ell m}(\cos\theta)(\delta_p^{+1}\cos(m\phi) + \delta_p^{-1}\cos(m\phi)) \tag{A-21}$$

So we write the solution to Laplace's equation inside and outside the spheroid as

$$\Phi_{in} = \sum_{\ell=0}^{\infty} \sum_{m=0}^{\ell} \sum_{p=\pm 1} \left[C_{\ell m} P_{\ell m}(i\eta) + D_{\ell m} Q_{\ell m}(i\eta)\right] Y^{p}_{\ell m}(\theta,\phi) \tag{A-22}$$

and

$$\Phi_{in} = \sum_{\ell=0}^{\infty} \sum_{m=0}^{\ell} \sum_{p=\pm 1} \left[C'_{\ell m} P_{\ell m}(i\eta) + D'_{\ell m} Q_{\ell m}(i\eta)\right] Y^{p}_{\ell m}(\theta,\phi) \tag{A-23}$$

Now we note that as $\eta$ approaches zero, $Q_{\ell m}(i\eta)$ becomes infinite and as $\eta$ approaches infinity, $P_{\ell m}(i\eta)$ becomes infinite. The potential must be finite everywhere, requiring that the coefficients $D_{\ell m}$ and $C'_{\ell m}$ be set equal to zero. The potential also must be continuous at the spheroidal boundary. To satisfy this condition the potentials must be written as

$$\Phi_{in} = \sum_{\ell=0}^{\infty} \sum_{m=0}^{\ell} \sum_{p=\pm 1} A_{\ell mp} P_{\ell m}(i\eta) Q_{\ell m}(i\eta_o) Y^{p}_{\ell m}(\theta,\phi) \tag{A-24}$$

$$\Phi_{out} = \sum_{\ell=0}^{\infty} \sum_{m=0}^{\ell} \sum_{p=\pm 1} A_{\ell mp} P_{\ell m}(i\eta_o) Q_{\ell m}(i\eta) Y^{p}_{\ell m}(\theta,\phi) \tag{A-25}$$

These equations are the general form given for the potential in Chapter II.

Prolate Coordinates

Prolate spheroidal coordinates $(\eta', \theta, \phi)$ have three associated families of mutually orthogonal surfaces. They are confocal ellipses, double-sheeted hyperboloids and half planes. The scale factors for prolate spheroidal coordinates are

$$h_{\eta'} = a \left[\frac{\eta'^2 - \cos^2\theta}{1 + \eta'^2}\right]^{1/2} \tag{A-26}$$

$$h_{\theta} = a(\eta'^2 + \cos^2\theta)^{1/2} \tag{A-27}$$

and

$$h_{\phi} = a \sin\theta(\eta'^2 - 1)^{1/2} \tag{A-28}$$

where a is the focal length of the ellipses. The radius vector is

$$\vec{r} = a \sin\theta(\eta'^2 - 1)^{1/2}(\cos\phi\hat{i} + \sin\phi\hat{j}) + a\eta' \cos\theta\hat{k} \tag{A-29}$$

where $(\hat{i}, \hat{j}, \hat{k})$ are the Cartesian unit vectors. The unit vectors for the prolate spheroidal coordinates are

$$\hat{e}_{\eta'} = \frac{\eta' \sin\theta}{(\eta'^2 - \cos^2\theta)^{1/2}} (\cos\phi\hat{i} + \sin\phi\hat{j}) + \cos\theta\left[\frac{\eta'^2 - 1}{\eta'^2 - \cos^2\theta}\right]^{1/2}\hat{k} \tag{A-30}$$

$$\hat{e}_{\theta} = \cos\theta\left[\frac{\eta'^2 - 1}{\eta'^2 - \cos^2\theta}\right]^{1/2} (\cos\phi\hat{i} + \sin\phi\hat{j}) - \frac{\eta' \sin\theta}{(\eta'^2 - \cos^2\theta)^{1/2}}\hat{k} \tag{A-31}$$

and

$$\hat{e}_{\phi} = -\sin\phi\hat{i} + \cos\phi\hat{j} \tag{A-32}$$

The element of volume is

$$dV = a^3(\eta'^2 - \cos^2\theta)\, d\eta\, \sin\theta d\theta d\phi \qquad \text{(A-33)}$$

The gradient of a scalar is

$$\nabla\Phi = \frac{1}{a}\left[ \frac{(\eta'^2 - 1)^{1/2}}{(\eta'^2 - \cos^2\theta)^{1/2}} \frac{\partial\Phi}{\partial\eta} \hat{e}_\eta + \frac{1}{(\eta'^2 - \cos^2\theta)^{1/2}} \frac{\partial\Phi}{\partial\theta} \hat{e}_\theta + \right.$$

$$\left. \frac{1}{(\eta' - 1)^{1/2}\sin\theta} \frac{\partial\Phi}{\partial\phi} \hat{e}_\phi \right] + \qquad \text{(A-34)}$$

The divergence of a vector is

$$\nabla\cdot\vec{E} = \frac{1}{a(\eta'^2 - \cos^2\theta)} \left[ \frac{\partial}{\partial\eta'} [(\eta'^2 - \cos^2\theta)^{1/2}(\eta'^2 - 1)^{1/2} E_{\eta'}] \right] +$$

$$\frac{1}{a\,\sin\theta(\eta'^2 + \cos^2\theta)} \frac{\partial}{\partial\theta} (\sin\theta(\eta'^2 - \cos^2\theta)^{1/2} E_\theta) \frac{1}{a(1 - \eta'^2)^{1/2}\sin\theta} \frac{\partial E_\phi}{\partial\phi}$$

(A-35)

Laplace's equation in prolate spheroidal coordinates is given by [A.5]

$$\nabla^2\Phi = \frac{1}{a(\eta'^2 - \cos^2\theta)} \left[ \frac{\partial}{\partial\eta'} \left[ (\eta'^2 - 1)\frac{\partial\Phi}{\partial\eta'} \right] + \frac{\partial}{\partial\theta}\left[ \sin^2\theta \frac{\partial\Phi}{\partial\theta} \right] + \right.$$

$$\left. \frac{\eta'^2 - \cos^2\theta}{(1-\eta'^2)\sin^2\theta} \frac{\partial^2\Phi}{\partial\,\phi^2} \right]. \qquad \text{(A-36)}$$

Using the standard separation of variables technique as before, the potential is written as

$$\Phi = G(\eta')\, F(\theta)\, H(\phi) \qquad \text{(A-37)}$$

Dividing by the potential, Eq. (A-33) becomes

$$\frac{(\eta'^2-1)\sin^2\theta}{\eta'^2+\cos^2\theta}\left[\frac{1}{G}\frac{\partial}{\partial\eta}\left[(\eta'^2-1)\frac{\partial G}{\partial\eta}\right]+\frac{1}{F}\frac{\partial}{\partial\theta}\left[\sin^2\theta\frac{\partial F}{\partial\theta}\right]\right]+\frac{1}{H}\frac{\partial^2 H}{\partial\phi^2}=0. \tag{A-38}$$

The last term is a function only of $\phi$ and, therefore, must separately be equal to a constant. If the constant is $-m^2$ then

$$\frac{\partial^2 H}{\partial\phi^2}=-m^2H(\phi) \tag{A-39}$$

The solutions to Eq. (A-36) are [A.6]

$$H(\phi)=\begin{cases}K_{mp}\cos(m\phi)\\ L_{mp}\sin(m\phi)\end{cases} \tag{A-40}$$

Eq. (A-35) is now

$$\left[\frac{1}{G}\frac{\partial}{\partial\eta'}\left[(\eta'^2-1)\frac{\partial G}{\partial\eta'}\right]-\frac{m^2}{1-\eta'^2}\right]-\left[\frac{1}{F}\frac{\partial}{\partial\theta}\left[\sin^2\theta\frac{\partial F}{\partial\theta}\right]-\frac{m^2}{1-\cos\theta^2}\right]=0. \tag{A-41}$$

Each of the terms in the square brackets is dependent only on a single variable, $\theta$ or $\phi$. Each term must then separately be equal to a constant, and because the sum is zero the constants must be equal to each other. If the constant is $\ell(\ell+1)$, then Eq. (A-35) may be separated into two differential equations

$$\frac{1}{F}\frac{\partial}{\partial\theta}\left[(1-\cos^2\theta)\frac{\partial F}{\partial\theta}\right]-\frac{m^2}{1-\cos\theta^2}=-\ell(\ell+1) \tag{A-42}$$

and

$$\frac{1}{G}\frac{\partial}{\partial \eta'}\left[(\eta'^2-1)\frac{\partial G}{\partial \eta'}\right] - \frac{m^2}{1-\eta'^2} = -\ell(\ell+1) \qquad \text{(A-43)}$$

The solutions to Eq. (A-36) are the Legendre polynomials [A.7]

$$F(\cos\theta) = A_{\ell m}\, P_{\ell m}(\cos\theta) + B_{\ell m}\, Q_{\ell m}(\cos\theta) \qquad \text{(A-44)}$$

$Q_{\ell m}(\cos\theta)$ may be disregarded because it is infinite at $\cos\theta=\pm 1$. The solutions to Eq. (A-37) are the Legendre functions of real argument [A.8]. Here both functions are again included because each function will be restricted to a region where it remains finite.

The complete solution to Laplace's equation is

$$\Phi = \sum_{\ell=0}^{\infty} \sum_{m=0}^{\ell} \sum_{p=\pm 1} \left[C_{\ell m}\, P_{\ell m}(\eta') + D_{\ell m}\, Q_{\ell m}(\eta')\right]\left[A_{\ell m}\, P_{\ell m}(\cos\theta)\right]$$

$$\cdot \begin{bmatrix} K_{mp}\cos(m\phi) \\ L_{mp}\sin(m\phi) \end{bmatrix}. \qquad \text{(A-45)}$$

The terms containing $\theta$ and $\phi$ can be combined into the real spherical harmonics. They are defined in Eq. (A-20). So we write the solution to Laplace's equation inside and outside the spheroid as

$$\Phi_{in} = \sum_{\ell=0}^{\infty} \sum_{m=0}^{\ell} \sum_{p=\pm 1} \left[C_{\ell m}\, P_{\ell m}(\eta') + D_{\ell m}\, Q_{\ell m}(\eta')\right] Y^{p}_{\ell m}(\theta,\phi) \qquad \text{(A-46)}$$

and

$$\Phi_{in} = \sum_{\ell=0}^{\infty} \sum_{m=0}^{\ell} \sum_{p=\pm 1} \left[ C'_{\ell m} P_{\ell m}(\eta') + D'_{\ell m} Q_{\ell m}(\eta') \right] Y^{p}_{\ell m}(\theta,\phi) \qquad \text{(A-47)}$$

Now we note that as $\eta'$ approaches zero, $Q_{\ell m}(\eta')$ becomes infinite and as $\eta'$ approaches infinity, $P_{\ell m}(\eta')$ becomes infinite. The potential must be finite everywhere, requiring that the coefficients $D_{\ell m}$ and $C'_{\ell m}$ be set equal to zero. The potential also must be continuous at the spheroidal boundary. To satisfy this condition the potentials must be written as

$$\Phi_{in} = \sum_{\ell=0}^{\infty} \sum_{m=0}^{\ell} \sum_{p=\pm 1} A_{\ell mp} P_{\ell m}(\eta') Q_{\ell m}(\eta'_o) Y^{p}_{\ell m}(\theta,\phi) \qquad \text{(A-48)}$$

$$\Phi_{out} = \sum_{\ell=0}^{\infty} \sum_{m=0}^{\ell} \sum_{p=\pm 1} A_{\ell mp} P_{\ell m}(\eta'_o) Q_{\ell m}(\eta') Y^{p}_{\ell m}(\theta,\phi) \qquad \text{(A-49)}$$

These equations are the general form given for the potential in Chapter II.

# APPENDIX B

## THE TOTAL CROSS SECTION

This appendix carries through the major steps between Eq. (2-160) and the two Eqs. (2-171) and (2-173). Only the important steps are shown; the algebraic manipulations are omitted.

The numerator of Eq. (2-160) will simplify to

$$\mathrm{Re}[(\vec{E}_i \cdot \vec{E}_s^*) + \hat{n} \cdot \hat{n}(\vec{E}_s \cdot \vec{E}_i^*) - (\hat{n} \cdot \vec{E}_i)(\hat{n}_i \cdot \vec{E}_s)] \qquad \text{(B-1)}$$

The scattered electric field is given by Eq. (2-150). The unit vectors $\hat{n}$ and $\hat{n}_i$ are given by Eqs. (2-161) and (2-162). The form of the incident field depends on the polarization of the incident light.

To evaluate the cross section for s-polarized light we use Eq. (2-163) for the incident electric field and Eq. (2-170) for the dipole moment. If we use a vector identity then

$$(\hat{n} \times \vec{p}) \times \hat{n} = \vec{p} - \hat{n}(\vec{p} \cdot \hat{n}) \qquad \text{(B-2)}$$

Making the substitutions for $\vec{E}_s$, $\vec{E}_i$, $\hat{n}$ and $\hat{n}_i$ the total cross section for s-polarized light becomes

$$\sigma_{\substack{tot \\ s\text{-}pol}} \Big| = -\int \mathrm{Re}\left[\frac{k^2 e^{-ikr} e^{i\vec{k}\cdot\vec{r}}}{r}\left[\alpha_x^* \sin^2\Phi(1-\sin^2\theta\cos^2\phi) + \right.\right.$$

$$\alpha_y^* \cos^2\Phi(1-\sin^2\theta\sin^2\phi) + (\alpha_x^*+\alpha_y^*)\sin\Phi\cos\Phi\sin^2\theta\sin\phi\cos\phi\Big] +$$

$$\frac{k^2 e^{ikr} e^{-ik\cdot r}}{r}\left[\alpha_x \sin\Phi\sin\theta\sin\theta\sin\phi + \alpha_x \sin^2\Phi\cos\theta\cos\phi + \right.$$

$$\left.\left.\alpha_y \sin\theta\cos\Phi\sin\theta\cos\phi + \alpha_y \cos^2\Phi\cos\theta\cos\theta\right]\right] \qquad \text{(B-3)}$$

Now we use the plane wave expansion for $e^{\pm ik\cdot r}$ in terms of real spherical harmonics and the spherical Bessel functions. It is [B.1]

$$e^{\pm ik\cdot r} = 4\pi \sum_{\ell=0}^{\infty} (\pm 1)^{\ell} j_{\ell}(kr) \sum_{m=0}^{\ell} \sum_{p=\pm 1} Y^p_{\ell m}(\theta,\phi)\, Y^p_{\ell m}(\Theta,\Phi) \qquad \text{(B-4)}$$

The coordinates r, $\theta$, and $\phi$ are the spherical coordinates of the point of observation and the angles $\theta$ and $\Phi$ are the polar and azimuthal angles of incidence of the wave vector k. In addition if we rewrite the terms of the cross section containing $\theta$ and $\phi$ in terms of real spherical harmonics, we can do the integration easily by virtue of the orthogonality of the spherical harmonics.

If we evaluate each term in the cross section individually, The first term is

$$\alpha_x^* \sin^2\Phi(1-\sin^2\theta\cos^2\phi) \qquad \text{(B-5)}$$

In terms of spherical harmonics this becomes

$$\alpha_x^* \sin^2\Phi \left[\frac{2\sqrt{4\pi}}{3} Y_{00}^2(\theta,\phi) + \frac{1}{3}\sqrt{\frac{4\pi}{5}} Y_{20}^1(\theta,\phi) - \frac{1}{3}\sqrt{\frac{12\pi}{5}} Y_{22}^1(\theta,\phi)\right] \quad \text{(B-6)}$$

And using the plane wave expansion in Eq. (B-4) the first term is

$$\sigma_1 = -\frac{4\pi\omega r}{c^2} \mathrm{Re}\Big[ e^{-ikr} \alpha_x^* \sin^2\Phi \Big[ j_0(kr) \frac{2\sqrt{4\pi}}{3} Y_{00}^1(\theta,\Phi) -$$

$$j_2(kr) \frac{1}{3}\sqrt{\frac{4\pi}{5}} Y_{20}^1(\theta,\Phi) + j_2(kr) \frac{1}{3}\sqrt{\frac{12\pi}{5}} Y_{22}^1(\theta,\Phi)\Big] \Big] \quad \text{(B-7)}$$

Now the point of observation is a large distance away from the source when compared to the magnitude of the wave vector so for large values of r the spherical Bessel functions for $\ell=0$ and $\ell=2$ are [B.2]

$$j_0 \approx \frac{\sin(kr)}{kr} \quad , \quad j_2 \approx \frac{-\sin(kr)}{kr} \quad \text{(B-8)}$$

so

$$\sigma_1 = \frac{-4\pi\omega}{c} \mathrm{Re}[\sin(kr)\alpha_x^* \sin^2\Phi(1-\sin^2\theta \cos^2\Phi) e^{-ikr}] \quad \text{(B-9)}$$

Similarly we find for the second and third terms

$$\sigma_2 = \frac{-4\pi\omega}{c} \mathrm{Re}[\sin(kr)\alpha_y^* \cos^2\Phi(1-\sin^2\theta \sin^2\Phi) e^{-ikr}] \quad \text{(B-10)}$$

and

$$\sigma_3 = \frac{-4\pi\omega}{c} \mathrm{Re}[\sin(kr)(\alpha_y^*+\alpha_y^*) \cos^2\Phi \sin^2\theta \sin^2\Phi e^{-ikr}] \quad \text{(B-11)}$$

For the remaining four terms we use the spherical Bessel function for $\ell=1$ and large r;

$$j_1 \approx \frac{-\cos(kr)}{kr} \tag{B-12}$$

Combining all seven terms we find

$$\sigma_{\substack{tot \\ s\text{-}pol}} \Big| = \frac{-4\pi\omega}{c} \mathrm{Re}[e^{-ikr}\sin(kr)(\alpha_x^*\sin^2\Phi + \alpha_y^*\cos^2\Phi) + e^{ikr}i\cos(kr)(\alpha_x\sin^2\Phi + \alpha_y\cos^2\Phi)] \tag{B-13}$$

If we use Euler's equation for $e^{\pm ikr}$ [B.3] and use $\alpha_x$=Re $\alpha_x$+iIm $\alpha_x$, and $\alpha_x^*$=Re $\alpha_x$-iIm $\alpha_x$ with similar expressions for $\alpha_y$,

$$\sigma_{\substack{tot \\ s\text{-}pol}} \Big| = \frac{4\pi\omega}{c}(\mathrm{Im}\ \alpha_x\sin^2\Phi + \mathrm{Im}\ \alpha_y\cos^2\Phi) \tag{2-171}$$

For p-polarization we follow the same procedure using Eq. (2-164) for the incident electric field and Eq. (2-172) for dipole moment. The total cross section is then

$$\sigma_{\substack{tot \\ p\text{-}pol}} = -\int \mathrm{Re}\left[\frac{k^2 e^{-ikr} e^{i\vec{k}\cdot\vec{r}}}{r}\left[\alpha_x^* \cos^2\theta \cos^2\Phi(1-\sin^2\theta\cos^2\phi) + \right.\right.$$

$$\alpha_y^* \cos^2\theta \sin^2\Phi(1-\sin^2\theta\sin^2\phi) + \alpha_z^* \sin^2\theta \sin^2\theta -$$

$$(\alpha_x^*+\alpha_y^*)\cos^2\theta \sin\Phi \cos\Phi \sin^2\theta \sin\phi \cos\phi +$$

$$(\alpha_x^*+\alpha_z^*)\cos\theta \sin\theta \cos\Phi \sin\theta \cos\theta \cos\phi +$$

$$\left.(\alpha_y^*+\alpha_z^*)\cos\theta \sin\theta \sin\Phi \sin\theta \cos\theta \sin\phi \right] +$$

$$\frac{k^2 e^{ikr} e^{-i\vec{k}\cdot\vec{r}}}{r}\left[\alpha_x \cos^2\Phi \cos\theta \cos\theta + \alpha_y \sin^2\Phi \cos\theta \cos\theta + \right.$$

$$\left.\alpha_z \sin\theta \cos\Phi \sin\theta \cos\phi + \alpha_z \sin\theta \sin\Phi \sin\theta \sin\phi\right] \qquad \text{(B-14)}$$

Using Eq. (B-4) and writing the angular functions in terms of the real spherical harmonics we evaluate term by term again. We also use the expressions for the spherical Bessel functions in Eq. (B-8). Evaluating and combining the ten terms of the cross section

$$\sigma_{\substack{tot \\ p\text{-}pol}} = \frac{-4\pi\omega}{c} \mathrm{Re}[e^{-ikr}\sin(kr)(\alpha_x^* \cos^2\theta \cos^2\Phi + \alpha_y^* \cos^2\theta \sin^2\Phi + \alpha_z^* \sin^2\theta)$$

$$+ e^{ikr} i\cos(kr)(\alpha_x \cos^2\theta \cos^2\Phi + \alpha_y \cos^2\theta \sin^2\Phi + \alpha_z \sin^2\theta)] \qquad \text{(B-15)}$$

Using Euler's equation again and the expressions for the real and imaginary parts of the polarizability as before

$$\sigma_{tot}\Big|_{p\text{-}pol} = \frac{-4\pi\omega}{c}\left[\cos^2\theta(\mathrm{Im}\,\alpha_x\cos^2\Phi + \mathrm{Im}\,\alpha_y\sin^2\Phi) + \mathrm{Im}\,\alpha_z\sin^2\theta\right] \quad \text{(B-16)}$$

# VITA

Milan C. Buncick was born in Lenoir, North Carolina, on September 20, 1956. He is the son of Mr. and Mrs. Michael Buncick. He attended Hibriten High School and graduated in June, 1974. The following Setember he entered Appalachian State University in Boone, North Carolina. In December 1979, he received a Bachelor of Science degree in Physics. In January 1980 he entered the Graduate School of The University of Tennessee, Knoxville, and received the Doctor of Philosophy with a major in Physics in June 1987.